UNIVERSIDADE ESTADUAL DE CAMPINAS
Instituto de Física Gleb Wataghin

ALLAN MACHADO PAYERAS

USE OF A SMALL PHOTOMULTIPLIER TUBE TO EXTEND THE DYNAMIC RANGE OF THE SURFACE DETECTOR OF THE PIERRE AUGER OBSERVATORY

USO DE FOTOMULTIPLICADORA PEQUENA PARA ESTENDER O ALCANCE DINÂMICO DO DETECTOR DE SUPERFÍCIE DO OBSERVATÓRIO PIERRE AUGER

CAMPINAS
2018

ALLAN MACHADO PAYERAS

USE OF A SMALL PHOTOMULTIPLIER TUBE TO EXTEND THE DYNAMIC RANGE OF THE SURFACE DETECTOR OF THE PIERRE AUGER OBSERVATORY

USO DE FOTOMULTIPLICADORA PEQUENA PARA ESTENDER O ALCANCE DINÂMICO DO DETECTOR DE SUPERFÍCIE DO OBSERVATÓRIO PIERRE AUGER

Dissertation presented to the Institute of Physics "Gleb Wataghin" of the University of Campinas in partial fulfilment of the requirements for the degree of Master, in the area of Physics.

Dissertação apresentada ao Instituto de Física "Gleb Wataghin" da Universidade Estadual de Campinas como parte dos requisitos exigidos para a obtenção do título de Mestre em Física, na área de Física.

Supervisor/Orientador: Prof. Dr. Anderson Campos Fauth

Este trabalho corresponde à versão final da dissertação defendida pelo aluno Allan Machado Payeras, e orientado pelo Prof. Dr. Anderson Campos Fauth.

CAMPINAS

2018

Agência(s) de fomento e nº(s) de processo(s): CNPq, 131956/2016-7

Ficha catalográfica
Universidade Estadual de Campinas
Biblioteca do Instituto de Física Gleb Wataghin
Lucimeire de Oliveira Silva da Rocha - CRB 8/9174

M18u

Machado Payeras, Allan, 1992-
Use of a small photomultiplier tube to extend the dynamic range of the surface detector of the Pierre Auger Observatory / Allan Machado Payeras. – Campinas, SP : [s.n.], 2018.

Orientador: Anderson Campos Fauth.
Dissertação (mestrado) – Universidade Estadual de Campinas, Instituto de Física Gleb Wataghin.

1. Detectores Cherenkov. 2. Detectores de partículas. 3. Raios cósmicos. I. Fauth, Anderson Campos, 1957-. II. Universidade Estadual de Campinas. Instituto de Física Gleb Wataghin. III. Título.

Informações para Biblioteca Digital

Título em outro idioma: Uso de fotomultiplicadora pequena para estender o alcance dinâmico do detector de superfície do Observatório Pierre Auger
Palavras-chave em inglês:
Cherenkov counters
Particle detectors
Cosmic rays
Área de concentração: Física
Titulação: Mestre em Física
Banca examinadora:
Anderson Campos Fauth [Orientador]
André Massafferri Rodrigues
Carola Dobrigkeit Chinellato
Data de defesa: 19-10-2018
Programa de Pós-Graduação: Física

MEMBROS DA COMISSÃO JULGADORA DA DISSERTAÇÃO DE MESTRADO DE **ALLAN MACHADO PAYERAS – RA 164178** APRESENTADA E APROVADA AO INSTITUTO DE FÍSICA "GLEB WATAGHIN", DA UNIVERSIDADE ESTADUAL DE CAMPINAS, EM 19 / 10 / 2018.

COMISSÃO JULGADORA:

- Prof. Dr. Anderson Campos Fauth – Orientador – IFGW/UNICAMP
- Prof. Dr. André Massafferri Rodrigues – CBPF
- Profa. Dra. Carola Dobrigkeit Chinellato – IFGW/UNICAMP

OBS.: Informo que as assinaturas dos respectivos professores membros da banca constam na ata de defesa já juntada no processo vida acadêmica do aluno.

CAMPINAS
2018

Dedico essa dissertação, com muito amor, à minha família, o pilar sólido da minha vida que me ensinou as lições mais valiosas, me apoiou e acreditou em mim desde o ínicio.

AGRADECIMENTOS

Agradeço aos meus pais, irmão e avó por terem me dado muito amor e me incentivado da forma mais carinhosa a alcançar meu sonhos.

À minha namorada, Paula Kempe, que tive a alegria de conhecer durante meus estudos de mestrado. Você traz muita luz a minha vida e aquece meu coração.

Ao Prof. Dr. Anderson Campos Fauth por me orientar neste trabalho, enriquecer muito meu conhecimento, me apoiar e incentivar minha carreira científica.

Aos meus amigos.

A Dra. Antonella Castellina e ao Dr. Marco Aglietta pelas valiosas discussões para a realização desse trabalho. Também ao apoio da Prof. Dra. Carola Dobrigkeit.

A Universidade Estadual de Campinas e ao Instituto de Física "Gleb Wataghin" pela fantástica estrutura e qualidade de ensino.

Ao auxílio financeiro do Conselho Nacional de Desenvolvimento Científico e Tecnológico.

O presente trabalho também foi realizado com apoio da Coordenação de Aperfeiçoamento de Pessoal de Nível Superior - Brasil (CAPES) - Código de Financiamento 001.

RESUMO

Raios cósmicos são partículas que permeiam o universo e estão constantemente atingindo a Terra. Os raios cósmicos de mais altas energias, ao penetrarem a atmosfera terrestre, interagem principalmente com moléculas de nitrogênio e oxigênio produzindo cascatas de partículas. Esse fenômeno é conhecido como chuveiro atmosférico extenso.

Dado o baixo fluxo de raios cósmicos com energias maiores que 100 PeV, a detecção direta dessas partículas não é uma abordagem prática. Ao invés, são detectados os chuveiros atmosféricos que estas produzem. Para isso são utilizados detectores espalhados por uma grande área que assim possibilitam o acúmulo de dados suficientes para estudos.

O Observatório Pierre Auger, localizado na Argentina, é o maior observatório de raios cósmicos do mundo. Ele emprega duas técnicas independentes e complementares na detecção de chuveiros atmosféricos extensos. O detector de superfície é composto por uma rede de 1660 tanques de água Cherenkov espalhados por uma área de 3000 quilômetros quadrados. A atmosfera acima do detector de superfície é observada por 27 telescópios de fluorescência distribuídos em quatro sítios de observação.

Cada tanque Cherenkov contém 12000 litros de água. No topo deste volume estão instaladas três fotomultiplicadoras. Quando partículas carregadas, provenientes de chuveiros atmosféricos, atravessam o volume de água com velocidade maior que a da luz nesse meio, é emitida radiação Cherenkov. Os fótons são refletidos no interior do tanque de forma difusa e geram um sinal nas fotomultiplicadoras. Quanto maior o número de partículas atravessando o tanque, maior o sinal.

Quando um grande número de partículas passa por um detector Cherenkov, as fotomultiplicadoras deste podem vir a saturar. Isso tem um impacto nos procedimentos de reconstrução de chuveiros utilizados para a obtenção de informações como a energia e composição dos raios cósmicos primários.

Para resolver o problema de saturação foi proposta a implementação de uma fotomultiplicadora adicional com fotocátodo de pequena área, como parte do plano de atualização do observatório. Com a implementação de tal fotomultiplicadora nos detectores, menos fótons serão coletados em relação as fotomultiplicadoras convencionais, portanto diminuindo drasticamente a probabilidade de saturação.

Para testar a proposta, dez detectores experimentais receberam fotomultiplicadoras pequenas. Utilizando dados desses detectores, realizamos um estudo da performance das fotomultiplicadoras no campo, constatando que estas são robustas ao ambiente. Utilizando as fotomultiplicadoras convencionais, fizemos a calibração das fotomultiplicadoras pequenas, para que estas expressem os sinais em termos da carga produzida por um múon vertical cruzando o centro do detector. Descobrimos uma dependência da calibração com variações a longo prazo da temperatura. Por fim, constatamos que, com a implementação das fotomultiplicadoras pequenas, o alcance dinâmico dos detectores é aumentado por um fator de aproximadamente 25 vezes, o qual reduz a ocorrência de saturação para menos de 0,1% dos eventos.

ABSTRACT

Cosmic rays are particles that permeate the universe and constantly bombard the Earth. High-energy cosmic rays, when penetrating Earth's atmosphere, interact mainly with nitrogen and oxygen molecules producing cascades of particles. This phenomenon is called extensive air shower.

Given the low flux of cosmic rays with energies greater than 100 PeV, the direct detection of these particles is not a practical approach. Instead, detectors spread over a large area are used to detect extensive air showers produced by energetic cosmic rays, allowing enough data to be collected for further studies.

The Pierre Auger Observatory in Argentina is the largest cosmic-ray observatory in the world. It employs two independent and complementary techniques for detecting extensive air showers. The surface detector is composed of 1660 water-Cherenkov detectors spread over an area of 3000 squared kilometres. The atmosphere above the surface detector is observed by 27 fluorescence telescopes at four observation sites.

The water-Cherenkov detectors consist of a tank containing 12000 liters of water. On top of this volume, three photomultiplier tubes are present. When charged particles from extensive air showers cross the water with speed higher than that of light in that medium, Cherenkov radiation is emitted. The photons are diffusely reflected on the tank interior and produce a signal in the photomultiplier tubes. The larger the number of particles crossing the detector, the larger the signals.

When a large number of particles pass through a water-Cherenkov detector, its photomultiplier tubes may saturate. This impacts on the procedures to reconstruct showers, which are used for obtaining information like energy and composition of the primary cosmic ray.

As part of the upgrade plan for the Observatory, the implementation of an additional photomultiplier tube with small photocathode area was proposed to solve the saturation problem. For an event, less photons will be collected by the small photomultiplier compared to the standard ones. Therefore, the probability of saturation will be drastically reduced.

Ten water-Cherenkov detectors were equipped with small photomultiplier tubes to test the proposal. We used their data to study the performance of the small photomultiplier tubes in the field. We found that they are robust in the environment. Using the

standard photomultiplier tubes, we calibrated the small ones so that their signals are given in terms of the charge produced by a vertical muon crossing the centre of a detector. We found a dependency of the calibration on long-term variations of temperature. At last, we verified that the implementation of the small photomultiplier extended the dynamic range of the water-Cherenkov detectors by a factor of approximately 25 times. It reduced the occurrence of saturation to less than 0.1% of the events.

List of Figures

List of Tables

Contents

Chapter 1

Introduction

The Earth is constantly bombarded by particles coming from outer space, the so-called cosmic rays. Cosmic rays that are energetic enough penetrate the atmosphere and collide with atmospheric molecules, mainly nitrogen and oxygen. Such collisions produce secondary particles, the great majority being charged and neutral pions.

Almost immediately after their production, neutral pions decay into a pair of photons, which produce electron-positron pairs. These will interact with air molecules and produce new photons by the bremsstrahlung process. The photons will again give origin to electron-positron pairs and the whole process repeats forming what is called an electromagnetic cascade.

Charged pions will interact again with atmospheric molecules producing hadronic particles, mostly new charged and neutral pions. The latter will decay into photons contributing further to the electromagnetic cascade. Charged pions, in turn, interact again with air molecules giving birth to a hadronic cascade. Once the energy of pions is small enough so that the probability of they decaying is larger than interacting further with air molecules, muons are produced as their decay product. This gives birth to what is called the muonic component. The collection of particles produced in the interaction of cosmic rays with the atmosphere are called extensive air showers (EAS).

The energy of cosmic rays ranges from below 1 GeV up to 10^{20} eV. They are the most energetic particles observed in Nature. For more than one century, humans are trying to understand the origin and nature of such cosmic particles. With that goal in mind the Pierre Auger Observatory was constructed in Argentina.

The Pierre Auger Observatory studies the highest-energy cosmic rays. Unfortunately, these have a very low flux, for instance, for the energy of approximately 10^{19} eV one particle is observed per squared kilometer per year, therefore direct detection is unpractical. To obtain information about such energetic particles, the Pierre Auger Observatory deployed detectors over a large area of approximately 3000 km^2. They detect the EAS particles produced by primary cosmic rays.

Two independent and complementary techniques of detection are employed by the observatory. An array of 1600 water-Cherenkov detectors (WCD) and four sites with six fluorescence telescopes each are used to detect extensive air showers.

As charged EAS particles propagate through the atmosphere they excite nitrogen molecules which emit fluorescence light isotropically in the ultraviolet frequency range. During dark moonless nights, such light is detected by the fluorescence telescopes which observe the longitudinal development of the EAS. As the amount of fluorescence light emitted is proportional to the energy of the shower particles, the fluorescence technique provides an almost-calorimetric measurement of the energy of the primary cosmic rays.

The water-Cherenkov detectors consist of a cylindrical tank of water with three photomultiplier tubes (PMTs) symmetrically placed on the surface of the water volume facing down into it. The WCDs are disposed 1500 m from the nearest neighbors forming a triangular-grid array. When charged particles pass through the water volume with speed higher than that of light in that medium, they emit Cherenkov radiation. The photons are diffusely reflected in the tank liner and produce a signal in the PMTs. The amount of Cherenkov light produced, and thus the PMTs signals, is proportional to the number of particles crossing the tank, therefore the WCDs measure particle density.

Several WCDs are triggered in an EAS event. Their signals are fit to a function which describes the particle density as a function of the distance to the shower core, i.e., a lateral distribution function (LDF). This procedure allows the determination of the position which the shower axis hits the ground. Combining this information with the trigger time of each detector, the arrival direction of the primary particle can be obtained.

From the LDF fit, the signal at 1000 m from the shower core ($S(1000)$) is also determined. It is the observable chosen to represent the size of the EAS. The choice of using the distance of 1000 m is because it minimises the dependency on the LDF chosen to describe the lateral profile of the shower. Using events observed by both the

WCDs and the fluorescence telescopes, the so-called hybrid events, one can find a relation between $S(1000)$ and the almost-calorimetric energy measured with the telescopes. This relation allows the determination of energy with the ground array with no need to rely on simulations, hence demonstrating the power of the hybrid design of the observatory.

The number of particles close to the shower core is very high. When these particles pass through a WCD, copious amounts of photons are produced which, in turn, might saturate the PMTs. In fact, more than 40% of the events with energy higher than 3×10^{19} eV have at least one saturated station, usually the one closest to the shower core [1]. This turns out to be a problem because the saturated signals are also included in the LDF fit, affecting the determination of $S(1000)$ and hence the event reconstruction, i.e., the determination of energy, shower geometry and even the composition of the primaries.

The observatory is currently being upgraded to enhance its scientific capabilities. Within the upgrade proposal, a solution to the saturation problem has been put forward. The installation of an additional photomultiplier tube with a small photocathode area in all WCDs was proposed. Due to its small area, it will collect less photons compared to the standard PMTs, therefore the saturation probability in the WCDs is expected to greatly reduce.

As a test of the small PMT proposal (sPMT), ten experimental WCDs, the engineering array (EA), were equipped with sPMTs. In this work, we analysed data from the EA to assess the performance of the sPMTs in the field as well as study their calibration and validate the proposal by showing that their implementation extend the dynamic range of the WCDs, reducing the occurrence of saturated events.

This dissertation has six chapters. In Chapter 2, an overview of cosmic rays is presented with emphasis on extensive air showers. Chapter 3 describes the Pierre Auger Observatory including details of event reconstruction and the upgrade project. In Chapter 4, detailed information on the sPMT proposal is provided. The expected performance of the upgraded observatory and the experimental setup for the test in the EA are discussed. Our analysis of the data collected in the EA is then presented in Chapter 5. Finally, the main results and conclusions of our analysis are summarised in Chapter 6. The Appendix A was included to provide a basic background on photomultiplier tubes.

Chapter 2

Cosmic rays

In this chapter, some topics regarding cosmic rays are going to be discussed to provide a basic background relevant especially for detection of ultra-high energy cosmic rays. After a brief historical introduction, the physics of extensive air showers will be discussed using simple models to understand some of their basic features. Different detection techniques will be presented. In the end, a section is dedicated to the energy spectrum of cosmic rays and their composition.

2.1 The discovery of cosmic rays

The history of cosmic rays [2] can be traced back to 1900 when physicists discovered that the air presented some electrical conductivity, meaning that something should be ionising the air molecules. The source of such ionising agent was thought to be contamination of the environment by radioactive elements.

To investigate the phenomenon further, Victor Hess performed balloon flights to measure the ion density in the air for different heights. He found that the ionisation amount increased with altitude. In 1912, Hess concluded that the ionisation of air molecules should be due to ionising particles coming from outer space, marking what is considered to be the discovery of cosmic rays.

The discovery made by Hess was confirmed by Werner Kolhörster, who constructed a better measuring equipment and took balloon flights to higher altitudes in 1913 and 1914. In 1936, Hess was awarded the Nobel Prize for the discovery of cosmic rays, prize which he shared with Anderson for the discovery of the positron.

Since then, a lot of effort has been put into understanding the nature and origin of these particles. Several models have been developed to explain their astrophysical sources, acceleration mechanisms and propagation through interstellar and intergalactic media. Also on the experimental front, several detectors with increasing precision and sizes have been constructed to test cosmic-ray models.

2.2 Extensive air showers

As mentioned previously, cosmic rays produce cascades of particles, called extensive air showers, when they interact with atmospheric molecules. Although different primary cosmic rays, like proton or heavier atomic nuclei, produce showers with different characteristics, they all present electromagnetic, hadronic and muonic components. In the following, extensive air showers will be explained by describing these components using simple models.

2.2.1 Electromagnetic showers

When a photon (γ) with high energy penetrates the atmosphere, it will interact with air molecules and produce an electron-positron pair (e^-e^+). Energy loss due to Compton scattering is negligible at this stage. The electrons and positrons produce new photons by bremsstrahlung. These, in turn, will generate new e^-e^+ pairs and the whole process repeats to give origin to an electromagnetic cascade, which is illustrated in Fig. 2.1a.

This process does not happen endlessly. Every time the e^- and e^+ produce bremsstrahlung photons, their energy decreases. The electromagnetic cascade will cease when losses of energy by ionisation and excitation become more important than radiative losses. This happens for a critical energy of $\xi_c^e = 85$ MeV, assuming electrons propagating in the air.

Although an accurate picture of electromagnetic cascades is obtained by computer simulations, a simple model can be used to have a grasp of their main features. This model was presented by Heitler [3] and is illustrated in Fig. 2.1b. There, a photon with energy E_0 propagates in the atmosphere, upon the first interaction it produces a positron and an electron, each with half the initial energy of the photon. Each of these particles, after traversing a fixed distance $d = \lambda_r \ln 2$, where λ_r is the radiation length in

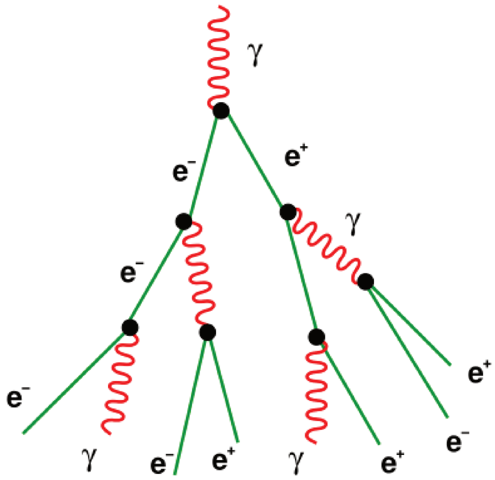

(a)

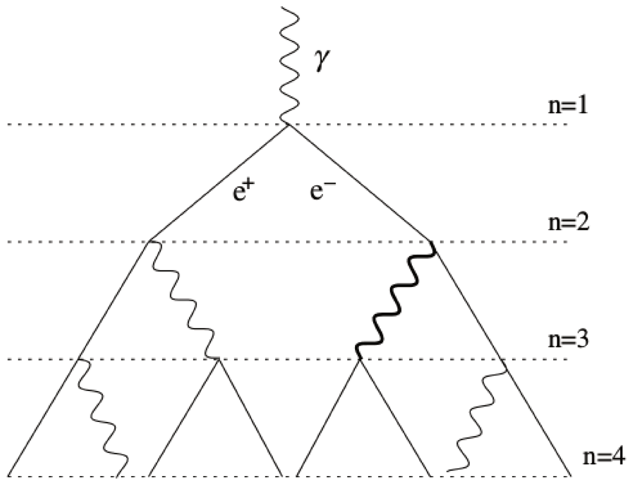

(b)

Figure 2.1: (a) Electromagnetic cascade. Photons produce e^-e^+ pairs when interacting with air molecules. Electron and positrons, in turn, produce photons by the bremsstrahlung process [4]. (b) Heitler model to describe electromagnetic cascades. Each particle interacts after traversing a fixed length giving origin to two particles sharing equally the energy of the parent particle [5].

the medium, gives origin to two particles with half the energy of the parent particle. In Heitler's model, each particle interacts after traversing a fixed distance d producing two outgoing particles, which share equally the energy of the parent particle.

After n interactions, at a distance $x = nd = n\lambda_r \ln 2$, the number of particles in the shower is $N = 2^n = e^{x/\lambda_r}$ and their energy is $E = E_0/2^n = E_0/e^{x/\lambda_r}$. The number of particles in the cascade will increase until the energy of the electrons (and positrons) becomes ξ_c^e. At that point, the number of particle reaches its maximum

$$N_{max} = \frac{E_0}{\xi_c^e} \ . \tag{2.1}$$

It follows that the number of interactions to achieve $N = N_{max}$ is $n_c = \ln(E_0/\xi_c^e)/\ln 2$. Therefore, the corresponding depth of maximum X_{max} is

$$X_{max} = x(n_c) = \lambda_r \ln\left(\frac{E_0}{\xi_c^e}\right) \ , \tag{2.2}$$

which is in good agreement with detailed simulations.

The number of particles at maximum shower development given by Eq. 2.1 is not compatible with what is found in simulations. The difference can be understood as due to the fact that the model does not account for electrons and positrons that range out and that multiple photons may be created by bremsstrahlung. The ratio between the number of particles predicted by Heitler's model and what is obtained from simulation is quite constant for different energies and propagation media. Therefore, an estimation for the order of magnitude of the number of electrons (and positrons) can be obtained by scaling N with a constant correction factor $g = 10$, so that

$$N_e = \frac{N}{g} \ . \tag{2.3}$$

Nevertheless, Heitler's model correctly describes two important features of electromagnetic cascades. The number of maximum particles is proportional to the primary energy (Eq. 2.1), and the depth of maximum shower development (X_{max}) grows logarithmically with energy (Eq. 2.2).

2.2.2 Hadronic showers

Hadronic showers are produced when protons or heavier nuclei from outer space interact with air molecules. After the primary interaction with the atmosphere, hadronic particles such as pions, kaons, η, ρ and heavier baryonic resonances are generated, although most part are neutral and charged pions (π^0 and $\pi^{\pm}$) produced in similar amounts each.

The charged hadrons interact further with air molecules to produce even more hadronic particles, like in the first interaction. This process goes on giving birth to a hadronic cascade. On the other hand, the produced neutral pions will almost immediately decay into two photons ($\pi^0 \rightarrow \gamma + \gamma$), which in turn generate electromagnetic cascades such as described in the previous section. Therefore, upon each interaction, part of the energy of the hadronic component of the shower is converted into an electromagnetic cascade.

The hadronic cascade will end when the characteristic interaction length of charged pions becomes larger than their decay length into muons and neutrinos ($\pi^{\pm} \rightarrow \mu^{\pm} + \nu_\mu/\bar{\nu}_\mu$). The critical energy ξ_c^π for which pion decay is more likely than it interacting with atmospheric molecules decreases slowly with primary energy. A fixed value of $\xi_c^\pi \approx$ 20 GeV is a good approximation. A pictorial description of the development of hadronic showers is shown in Fig 2.2a.

A simple model, inspired by that of Heitler, was developed by Matthews to

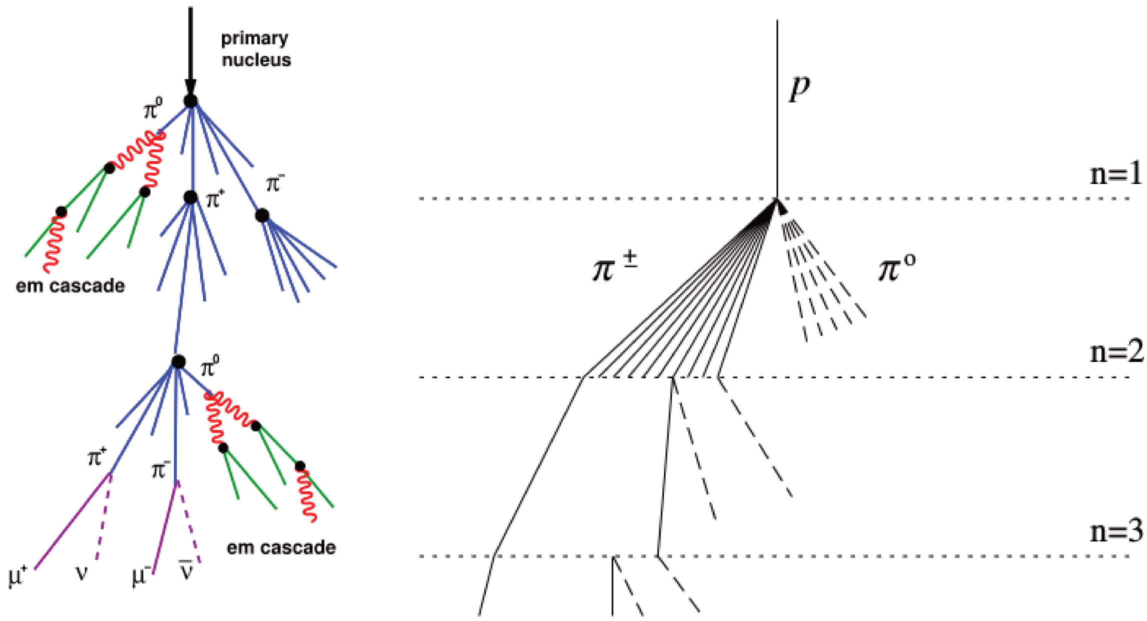

(a) (b)

Figure 2.2: (a) Development of a hadronic shower. Hadrons interact with atmospheric molecules producing new hadrons. Neutral pions decay into two photons which produce electromagnetic cascades. When the energy of charged pions falls bellow a critical value they decay into muons and neutrinos [4]. (b) Matthews' model of a hadronic shower. Upon each interaction, N_{ch} charged pions and $N_{ch}/2$ neutral pions are produced, dividing equally the energy of the parent particle [5].

describe hadronic showers [5]. In this model, a proton is assumed to enter Earth's atmosphere, and after an atmospheric length X_0, it interacts with air molecules producing N_{ch} charged pions and $N_{ch}/2$ neutral pions. The energy of the proton is equally distributed among the daughter particles. The neutral pions immediately decay into two photons which start electromagnetic cascades. Each of the charged pions traverses an atmospheric layer of length $\lambda_I \ln 2$, where λ_I is the interaction length, then interacts with air molecules to produce further N_{ch} charged pions and $N_{ch}/2$ neutral pions. The whole process repeats, such as shown in Fig. 2.2b, until the energy of the particles reaches ξ_c^π, when the charged pions are assumed to decay into muons and neutrinos.

After n interactions, the number of charged pions is $N_\pi = (N_{ch})^n$. The energy they carry, which will be referred to as the energy of the hadronic component, is

$$E_{had} = \left(\frac{2}{3}\right)^n E_0 \ . \tag{2.4}$$

On the other hand, the energy carried away by the electromagnetic cascades produced by π^0 decays, which will be called the energy of the electromagnetic component, is

$$E_{EM} = \left[1 - \left(\frac{2}{3}\right)^n\right] E_0 \ . \tag{2.5}$$

Equation 2.5 implies that after only six interactions about 90% of the primary energy is in the electromagnetic component.

Dividing Eq. 2.4 by the number of charged pions after n interactions yields their individual energy as a function of n:

$$E_\pi(n) = \frac{E_{had}}{N_\pi} = \frac{E_0}{\left(\frac{3}{2}N_{ch}\right)^n} \ . \tag{2.6}$$

This expression can be used to find the number of interactions after which the energy of the pions becomes ξ_c^π:

$$n_c = \frac{\ln\left(E_0/\xi_c^\pi\right)}{\ln\left(\frac{3}{2}N_{ch}\right)} \ . \tag{2.7}$$

The number of interactions n_c does not depend strongly on variations of N_{ch}. The multiplicity of particles produced, in turn, also varies very slowly with primary energy (it grows as $E^{1/5}$ for pp and $p\bar{p}$ collisions). Therefore, a constant value of $N_{ch} = 10$ can be used as a good approximation.

Concerning detection of particles produced in extensive air showers, an estimation of the energy of the primary proton can be achieved by measuring the number of electrons and muons. After maximum development of the shower, the particles reach the critical energy, ξ_c^π and ξ_c^e for the hadronic and electromagnetic components respectively. At this stage, charged pions decay into muons, thus $N_\pi = N_\mu$. The number of electromagnetic particles after shower maximum can be related to the number of electrons using Eq. 2.3, i.e., $N_{max}^{em.\ cascade} = gN_e$. Therefore, the energy of the primary is given by

$$\begin{aligned} E_0 &= \xi_c^e g N_e + \xi_c^\pi N_\mu \ , \\ &= g\xi_c^e \left(N_e + \frac{\xi_c^\pi}{g\xi_c^e} N_\mu\right) \ . \end{aligned} \tag{2.8}$$

Substituting $\xi_c^\pi = 20$ GeV, $\xi_c^e = 85$ MeV and $g = 10$ in Eq. 2.8 yields $E_0 = 0.85(N_e + 24N_\mu)$ GeV.

Equation 2.8 is, of course, an approximation, since during shower development the energy of a parent particle usually is not equally divided among its products. Still, it agrees incredibly well with the energy reconstruction performed by the CASA-MIA experiment [5, 6]. The important feature taken from expression 2.8 is that the primary energy grows linearly with the number of particles in the shower.

Deriving a good estimation for the depth of shower maximum X_{max} from Matthews' model is quite complicated. As mentioned, after a few interactions the shower initiated by a proton is mainly dominated by the electromagnetic component due to π^0 decay into photons. A more precise treatment should account for each electromagnetic cascade. However, following Matthews' approach, one can have an idea taking into account only the first electromagnetic cascade produced [5]. The primary proton is assumed to interact at atmospheric depth X_0. Since one third of its products are neutral pions, their individual energy is $E_{\pi^0} = 2E_0/3N_{ch}$. As neutral pions decay into two photons, assuming they equally share the energy of the π^0, each one will have energy $E_\gamma = E_0/3N_{ch}$. From Eq. 2.2, the photons will produce electromagnetic cascades with maximum development at depth

$$X_{max} = X_0 + \lambda_r \ln\left(\frac{E_0}{3N_{ch}\xi_c^e}\right) . \tag{2.9}$$

As regarded, Eq. 2.9 is not supposed to be taken as an accurate prediction, instead it can be seen as a lower limit to the actual X_{max}. Compared to simulations, it gives a result about 100 gcm^{-2} lower, due to neglecting further particle generations and also not accounting for the non-uniform distribution of energy of the daughter particles. Equation 2.9 shows that X_{max} depends on primary energy as well as interaction multiplicity.

The muons from a hadronic shower are due to the decay of charged pions, mainly when they reach the critical energy ξ_c^π. This is the *muonic component* of the shower. Assuming in Matthews' model that the number of muons is exclusively due to decay of charged pions after they reach the critical energy, then it is given by $N_\mu = (N_{ch})^{n_c}$, with n_c the number of interactions needed for the energy of the charged pions to be ξ_c^π. Substituting Eq. 2.7 in

$$\ln N_\mu = n_c \ln N_{ch}$$

leads to

$$N_\mu = \left(\frac{E_0}{\xi_c^\pi}\right)^\beta , \tag{2.10}$$

with

$$\beta = \frac{\ln N_{ch}}{\ln(3N_{ch}/2)} .$$

Using $N_{ch} = 10$, one finds $\beta = 0.85$. Therefore, the number of muons increases with a dependency on the primary energy which is less than linear. Simulation results yield β ranging from 0.85 to 0.92.

Heavier nuclear primaries

Approximations of features of extensive air showers produced by nuclei primaries can be obtained if one assumes that nuclei with atomic number A and energy E_0 are composed of A independent nucleons of energy E_0/A, each starting a hadronic shower as described by Matthews' model. Such approach is called the *superposition model*.

Using this idea one can easily find expressions for the energy, the depth of shower maximum and the number of muons, analogous to Eqs. 2.8, 2.9 and 2.10 respectively. For example, the number of muons produced by a nucleus of atomic number A and energy E_0 is

$$N_\mu^{(A)}[E_0] = AN_\mu^{(p)}[E_0/A] = A\left(\frac{E_0}{A\xi_c^\pi}\right)^\beta = A^{1-\beta}N_\mu^{(p)}[E_0] \ , \tag{2.11}$$

where the superscripts (A) and (p) refer to a nucleus and a proton respectively. Proceeding in a similar manner, expressions for $X_{max}^{(A)}$ and $E_0^{(A)}$ are found

$$X_{max}^{(A)} = X_{max}^{(p)} - \lambda_r \ln A \ , \tag{2.12}$$

$$E_0^{(A)} = g\xi_c^e\left(N_e + \frac{\xi_c^\pi}{g\xi_c^e}N_\mu\right) \ . \tag{2.13}$$

In the case of Eq. 2.12, $X_{max}^{(p)}$ is the depth of shower maximum for a proton (p) with same energy as the nuclear primary (A). This is done for comparison reasons.

Using $\beta = 0.85$, as previously, in Eq. 2.11 one finds $N_\mu^{(A)}[E_0] = A^{0.15}N_\mu^{(p)}[E_0]$. Therefore, a shower generated by a nucleus produces more muons than an equivalent shower initiated by a proton with the same energy. For example, an iron nucleus will produce $(56)^{0.15} = 1.8$ times more muons than a proton with same energy. This happens because the energy dependence of N_μ is not linear (see Eqs. 2.10 and 2.11).

Although expression 2.12 for $X_{max}^{(A)}$ derives from Eq. 2.9, which does not give an accurate description of $X_{max}^{(p)}$ for the reasons already discussed, Eq. 2.12 predicts that heavier nuclei will have a shallower X_{max} than an equally energetic proton. For instance, iron nuclei will have shower maximum $\lambda_r \ln(56) = 150$ gcm^{-2} higher than protons with the same energy. This result agrees with what is obtained from simulation.

The expression for energy estimation from the number of muons and electrons (Eq. 2.13) remains unchanged for nuclei compared to proton primaries, because in both

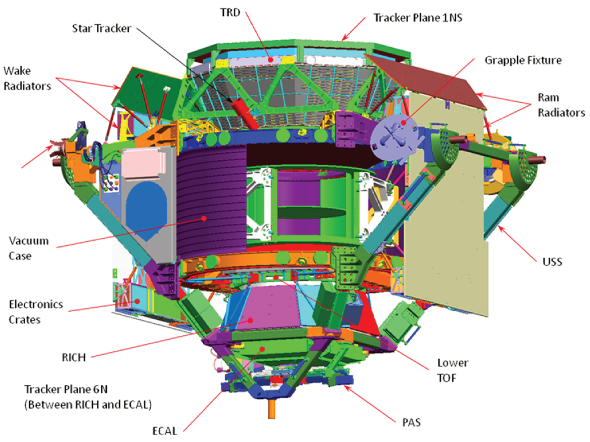

(a)

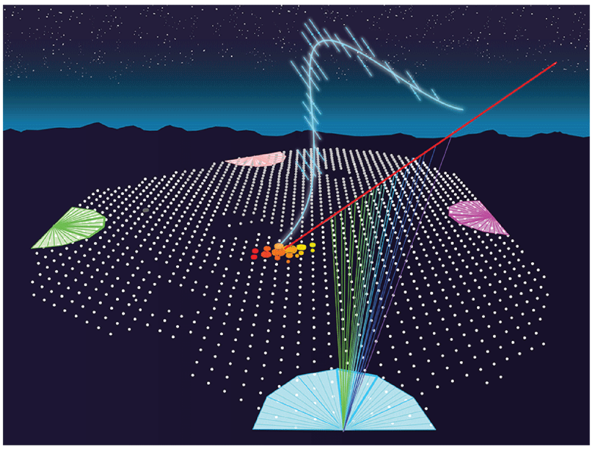

(b)

Figure 2.3: Cosmic rays can be detected directly or indirectly, depending on their flux. (a) The AMS detector, which is in the International Space Station, detects cosmic-ray particles directly [7]. (b) The Pierre Auger Observatory detects extensive air showers using a hybrid detection technique [8].

cases the total energy of the electromagnetic and hadronic components are accounted for by counting the total number of particles.

2.3 Detecting cosmic rays

The detection of cosmic rays can be divided into two clear categories: direct and indirect. The difference is due to the flux of cosmic rays, i.e., the number of particles reaching Earth per unit area per unit time, for different energy ranges.

For cosmic rays of energy below about 10^{14} eV, the flux is high enough to allow direct detection. The detectors can be calorimeters, emulsion stacks or transition radiation detectors, similar to the technology used in experiments of high-energy physics with particle accelerators. Such detectors are placed in the International Space Station, such as AMS (see Fig. 2.3a) or ISS-CREAM, in satellites, such as PAMELA, or even in balloons as in the case of ATIC and TRACER. The direct detection provides very accurate measurements of energy and composition of the cosmic-ray particles.

For energies above 10^{15} eV, the flux of cosmic rays is very low, therefore direct detection is simply not feasible. For instance, at energies above 5×10^{15} eV, one particle is detected per squared meter per year. In this case, information about the primary cosmic ray is obtained indirectly by detecting the numerous particles produced in the extensive air showers they induce, as described in the last section.

Ground arrays of detectors covering a large area are used to detect the particles produced in the air showers. The detectors can be scintillators, such as AGASA in Japan and KASCADE in Germany, or water-Cherenkov tanks, as pioneered by the Haverah-Park experiment in the United Kingdom. Another important technique is that of atmospheric light emission. When the relativistic shower particles propagate through the atmosphere with speed higher than that of light in the air, they produce Cherenkov radiation, which is highly collimated. They also excite atmospheric nitrogen molecules which emit fluorescence light in the ultraviolet part of the spectrum. The detection of these kinds of light is exploited by some experiments, such as done by the Fly's Eye and Hi-Res experiments in the United States.

Nowadays, observatories such as the Pierre Auger in Argentina (see Fig. 2.3b) and the Telescope Array in the United States apply a hybrid technique by combining both ground-array and fluorescence-light detectors. This approach greatly improves the data quality. However, the uncertainty in the measurements of quantities such as energy and composition is still larger than in direct detection.

2.4 Energy spectrum and composition of cosmic rays

Since the discovery of cosmic rays, many experiments were designed to understand their nature. The main questions to be answered concern the source of such particles, the mechanisms which accelerate them to high energies and how they propagate in the interstellar and intergalactic media. Studying the energy spectrum of cosmic rays and their composition, among other approaches such as anisotropy studies, provides a means to shed light on the questions of interest.

In Fig. 2.4, the differential flux of cosmic rays is presented as a function of their energy. The flux was multiplied by $E^{2.6}$ (E being the cosmic-ray energy) so that the features of the spectrum can be observed in a more pronounced manner. For energies below 10^{10} eV, the flux is suppressed by solar winds which sweep cosmic-ray particles away from the solar system. At these energies, the flux is modulated by the solar activity.

The cosmic-ray spectrum has three main distinctive regions. Each can be

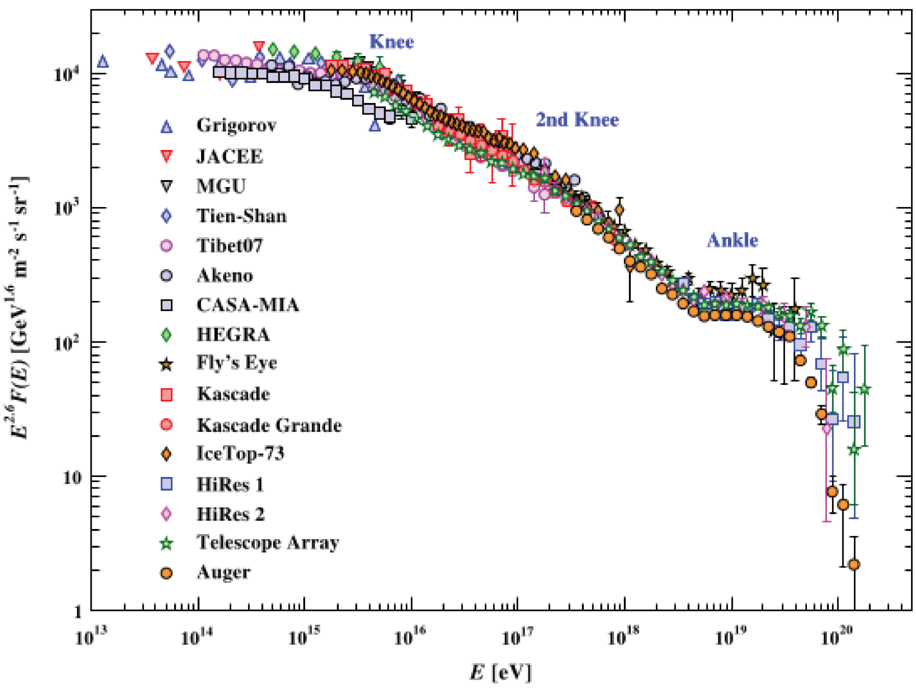

Figure 2.4: Differential flux of cosmic rays as a function of their energy [9]. The flux was multiplied by $E^{2.6}$ to make the features of the spectrum more prominent. The shape of the spectrum, following power-law functions for each distinctive regions, is closely related to acceleration mechanisms. A strong suppression is observed for energies above 4×10^{19} eV.

described by a power-law function of the form

$$\frac{d\phi}{dE} \propto E^{-\gamma} \ , \tag{2.14}$$

where ϕ is the flux and E is the energy of the cosmic rays. In the first region, up to the so called "knee" at approximately 4×10^{15} eV, $\gamma \approx 2.7$. Above that, the differential flux decreases more rapidly with $\gamma \approx 3.1$ until the energy of 5×10^{18} eV, known as the "ankle". The flux then becomes harder again with $\gamma \approx 2.6$. Between the knee and the ankle, a "second knee" is observed at 10^{17} eV, γ is approximately 3.0 on its left and 3.3 on the right where a further steepening happens.

The shape of the cosmic-ray spectrum suggests that they are accelerated by non-thermal processes. Enrico Fermi showed that cosmic rays going through moving magnetised regions of the space could lead to a spectrum with the power-law shape. An improved picture is obtained taking into account shock waves through magnetised regions. Such situation could be produced by supernova explosions. Other possible sources of cosmic rays include the neighbourhood of black holes and neutron stars.

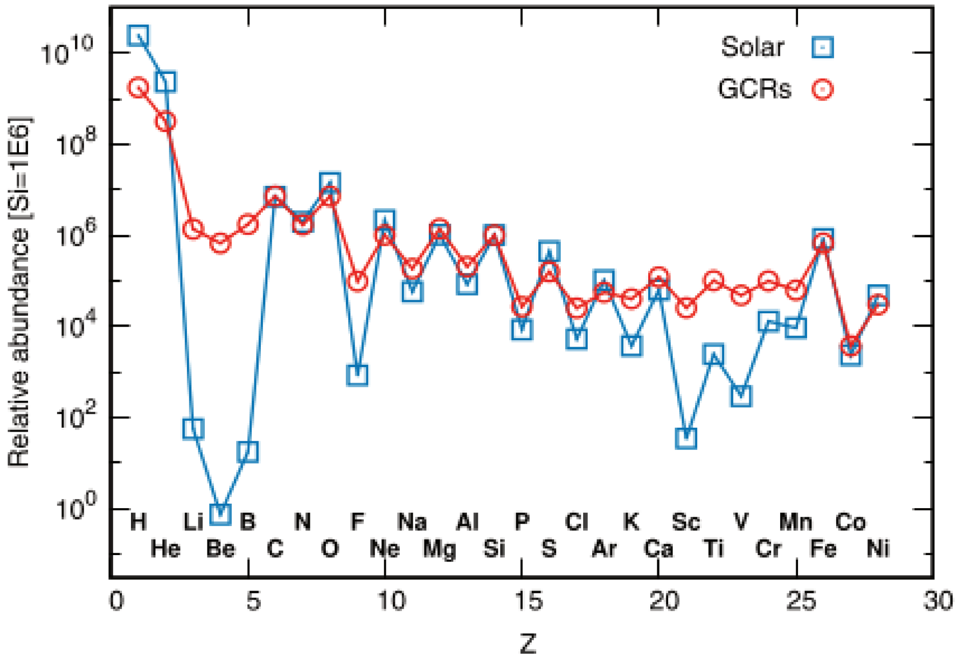

Figure 2.5: Relative abundances of elements in low-energy cosmic rays and in the solar system. The abundances were normalised so that they are 10^6 for Si [4]. The overall abundances are similar for cosmic rays and the solar system. The differences are mainly due to spallation of heavier nuclei producing lighter ones.

The hardening of the spectrum at the ankle region could be due to a transition from galactic to extragalactic cosmic rays. On the other hand, there are interpretations of the data that suggest that such transition could also happen somewhere between the second knee and the ankle [4].

A suppression of the cosmic-ray flux is observed for energies above 4×10^{19} eV. Different hypothesis try to explain this effect. For instance, high-energy protons may interact with photons of the cosmic background radiation to produce pions. This process, known as the GZK effect, predicts a cutoff in the cosmic-ray spectrum. The observed suppression could also be the result of an energetic limit of the astrophysical sources. To settle this question, more accurate data on the composition of ultra-high energy cosmic rays is needed.

In Fig. 2.5, the relative composition of low-energy cosmic rays is presented along with that of the solar system. The abundances were normalised so that they are 10^6 for Si. Overall, the compositions are very similar which suggests that the elements that compose the low-energy cosmic rays are produced by a similar process to the elements

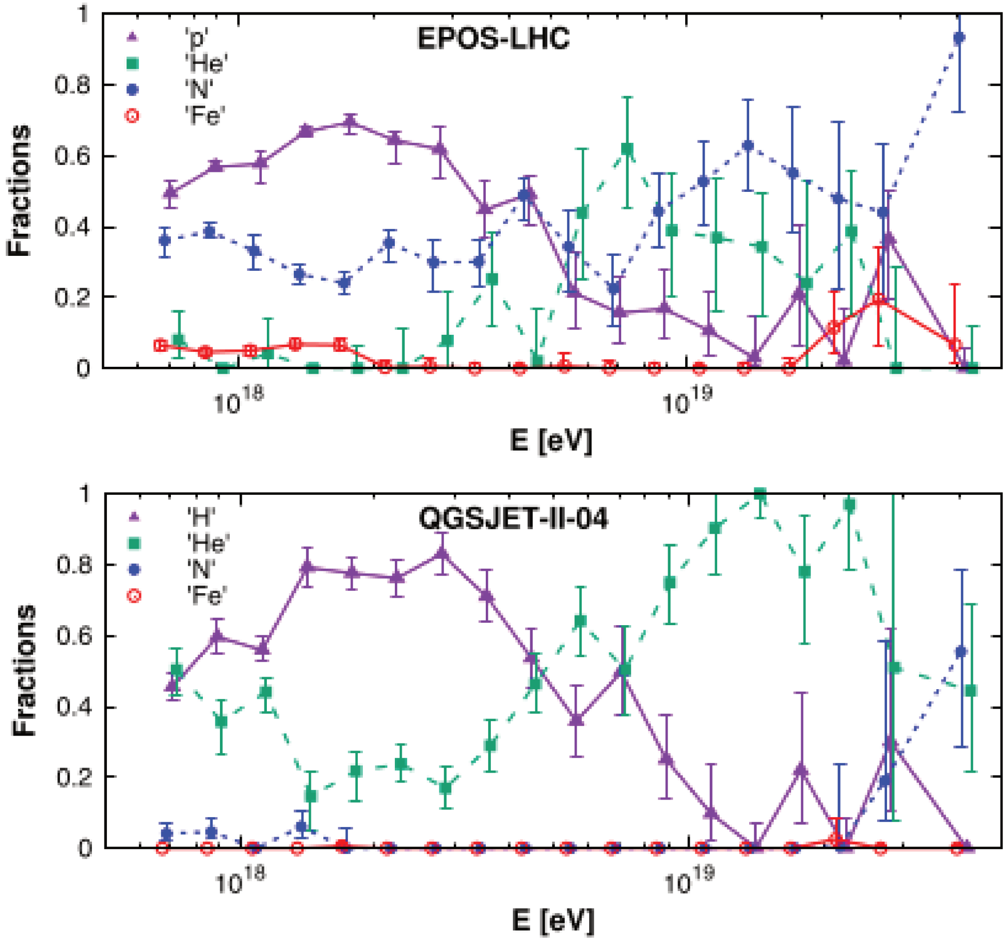

Figure 2.6: Composition of high-energy cosmic rays as a function of their energy [4]. The hadronic-interaction models EPOS-LHC and QGSJET-II-04 were used to interpret the data. Although the results present a dependency on the model used, both indicate a heavier composition for energies above 10^{19} eV.

that form planetary systems, i.e, by stellar nucleosynthesis. Despite the similarities, there are some noticeable differences. The abundances of H and He are larger in the solar system than in cosmic rays. This probably reflects the high ionisation potential of these elements which makes harder for them to be accelerated away from their sources. Another clear difference is that the abundances of Li, Be and B are much larger in cosmic rays. These elements are produced when heavier ones such as C, N and O interact with matter of the interstellar medium, causing them to break up into lighter elements. This process is called spallation and also occurs for Ne producing F, and for Fe and Ni which produce elements from Sc to Mn.

In the case of high-energy cosmic rays, studying their composition is more challenging since only data on extensive air showers produced by the primaries is available. Therefore, one must rely on simulations and extrapolations of the data on hadronic interactions for ultra-high energies to reconstruct the showers and obtain an estimation of the primary composition.

The composition for high-energy cosmic rays is presented in Fig. 2.6. Two models of hadronic interactions, EPOS-LHC and QGSJET-II-04, were used to interpret the data. The elements H, He, N and Fe should be regarded as groups of elements close to these atomic masses, since such an accuracy to separate elements is still not possible with the present data. The dependency of the results on the hadronic interaction model used is very clear if one compares the two plots. Nevertheless, both models suggest a heavier composition for energies above 10^{19} eV. Efforts are currently being made to improve the accuracy of data on high-energy cosmic rays, noticeably by the Pierre Auger Collaboration.

Chapter 3

The Pierre Auger Observatory

In this chapter a description of the Pierre Auger Observatory will be given. A general overview of the Observatory will be presented, describing its goals, structure and operation principles to perform key measurements to study ultra-high energy cosmic rays. A detailed description of the surface detector array, relevant to the work produced in this project, will be given. An exposure of how extensive air showers are reconstructed from the data collected by the Observatory will be presented. In conclusion, the proposed upgrade of the Observatory will be discussed.

3.1 Overview of the Observatory

The Pierre Auger Observatory was envisioned in 1991 by Jim Cronin and Alan Watson, with the aim of studying cosmic-ray particles with energy higher than 10^{17} eV, the most energetic particles observed in Nature. Accurate data is needed to test hypothesis of cosmic-ray sources, models of their acceleration and propagation in interstellar space as well as their nature.

The flux of cosmic rays with such high energies is very low. For energies above 4×10^{18} eV, the ankle region, less than one particle is observed per squared kilometer per year. Therefore, to study these particles the detectors of the Pierre Auger Observatory are spread over an area of ~ 3000 km^2, in the province of Mendoza, Argentina (see Fig. 3.1).

The Observatory obtains information about high-energy cosmic rays indirectly, by detecting extensive air showers produced by primary particles when they interact

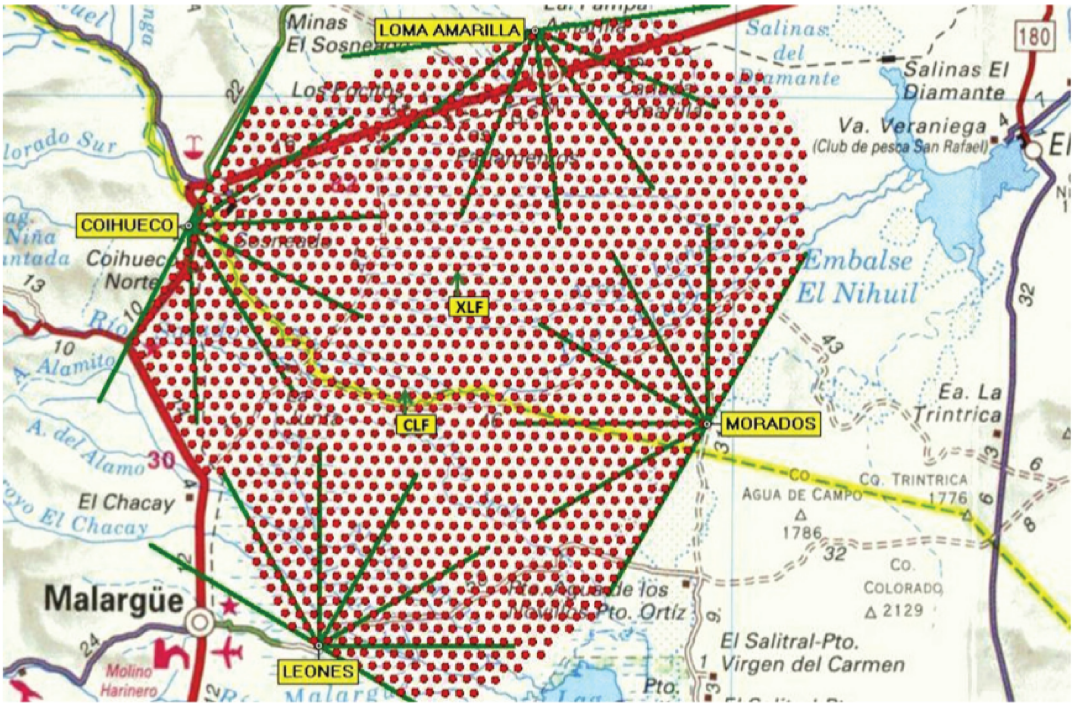

Figure 3.1: Overview of the Pierre Auger Observatory in the province of Mendoza, Argentina. Each red dot corresponds to a water-Cherenkov detector forming the surface detector array. The four fluorescence detector sites are also shown [10].

with the atmosphere. Such approach also allows fundamental particle interactions to be studied with the observatory data, especially because the energy of cosmic-ray particles are far beyond what is achieved with human-made accelerators. For instance, a cosmic-ray particle with energy 10^{19} eV has an equivalent center of mass energy of 100 TeV.

The Observatory employs two independent and complementary detection techniques to measure air shower properties [10]. An array of 1660 water-Cherenkov detectors, the so-called surface detector array (SD), is overlooked by 24 fluorescence telescopes distributed at four observation sites, each with six telescopes. In Fig. 3.1 an overview of the Observatory is presented, each dot representing a water-Cherenkov detector. The four fluorescence observation sites are also shown with the lines delimiting the field of view of each telescope. Pictures of a surface detector station and a fluorescence detector site are shown in Fig 3.2.

The water-Cherenkov detectors are placed forming a triangular grid, so that 1600 detectors have a separation of 1500 m from nearest neighbours and 60 have a 750 m spacing. The detectors are basically a tank filled with water and the associated electronics. When charged particles from extensive air showers pass through the water volume of a

(a) (b)

Figure 3.2: (a) A water-Cherenkov detector of the surface detector array. (b) A fluorescence detector site with six telescopes, each spanning a field of view of 30° in azimuth and elevation [10].

detector with speed larger than that of light propagating in water, Cherenkov radiation is emitted producing a signal proportional to the number of particles crossing the station. Thus the water-Cherenkov detectors measure particle density at ground level. A more detailed description will be given in Sec. 3.2.

Each fluorescence telescope spans a 30° field of view in azimuth as well as elevation (see Fig. 3.1). They operate in dark moonless nights, yielding a duty cycle of roughly 15% in contrast with the nearly 100% on the surface detector array. A schematic drawing of a telescope house is shown in Fig. 3.3, together with a corresponding picture.

The telescope mirror is made of smaller hexagonal or rectangular mirrors, which reflect light towards the camera, consisting of 440 photomultiplier tubes, model XP3062 by Photonis, arranged in 22 rows and 20 columns, each photomultiplier constituting a pixel. An ultraviolet filter is placed just behind the telescope aperture system allowing light transmission greater than 80% for the band between 330 and 380 nm. The electronics digitise the signals produced in the camera. A full description of the fluorescence detector can be found in reference [11].

When an extensive air shower develops, interactions of the shower particles, mainly the electromagnetic component, with nitrogen molecules of the atmosphere make them emit fluorescence light isotropically in the ultraviolet part of the spectrum. The fluorescence telescopes register such emissions as the shower develops in the atmosphere,

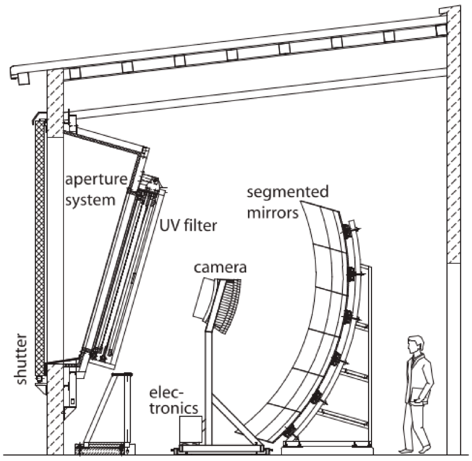

(a)

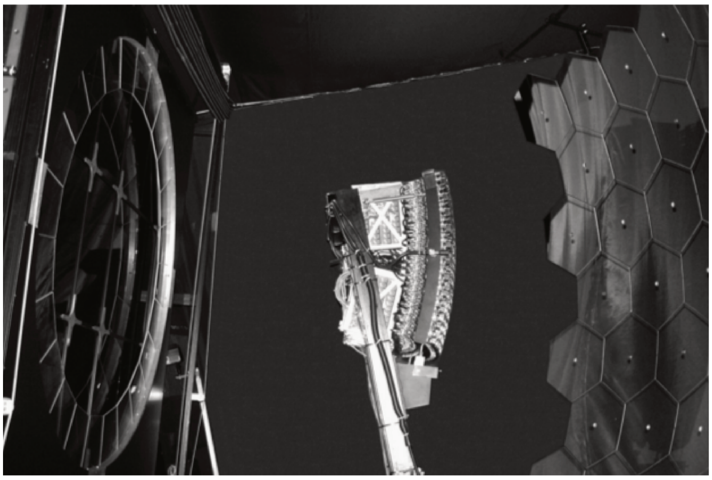

(b)

Figure 3.3: (a) Schematic view of the telescope setup and (b) corresponding picture [10, 11].

allowing the longitudinal shower profile to be observed. As the intensity of the fluorescence light is proportional to the energy deposited by the shower particles, integrating the energy deposit along the shower axis yields a nearly calorimetric determination of the primary energy.

The hybrid design of the observatory consists in combining the two different techniques, surface and fluorescence detectors, to obtain data of higher quality than would be possible with each technique alone. This approach also allows cross-checks of measurements such as energy, mass composition and arrival direction.

An example of the power of this hybrid design is illustrated in the energy determination of events. As mentioned, the fluorescence detector provides an almost-calorimetric measurement of energy, but it operates roughly 15% of the time. On the other hand, the surface detector array works 24 hours a day. Because the SD measures particle density at ground level, an energy estimation with the surface detector alone would have to make use of simulation, which is unreliable as the current understanding of hadronic interactions at such high energies is very limited. However, the hybrid design offers a workaround: using events observed by both detectors, i.e, hybrid events, it is possible to calibrate the surface detector array so that, when the fluorescence detector is not operational, reliable energy measurements can be done using only the SD. More details of this procedure will be described in Sec. 3.3.

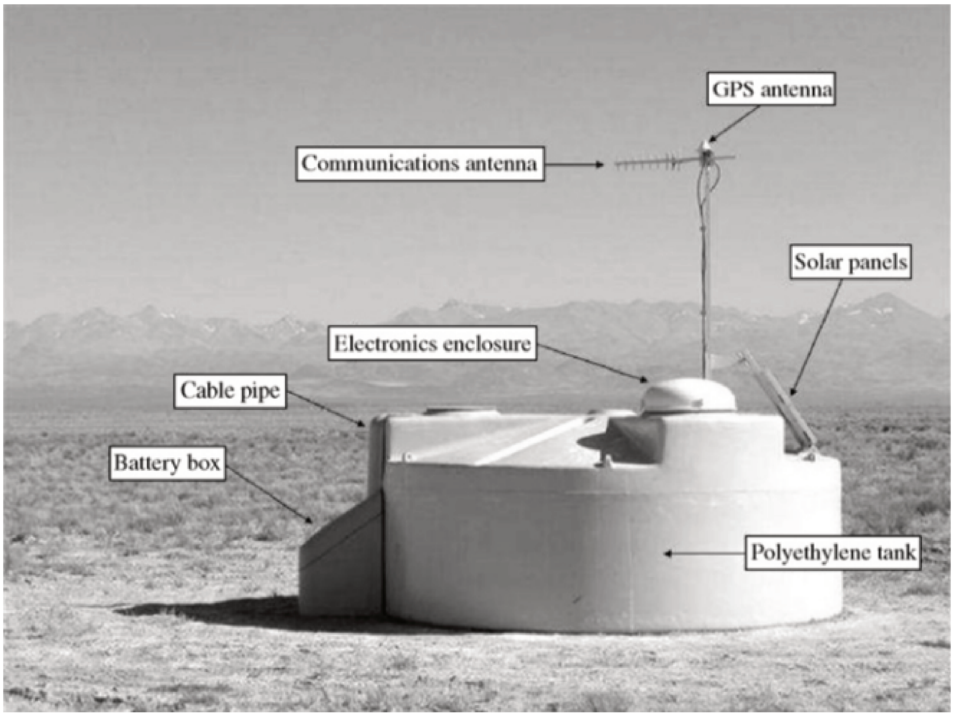

Figure 3.4: Picture of a water-Cherenkov detector. Its components are indicated [12].

3.2 The surface detector array

As mentioned previously, the surface detector is formed by two arrays of water-Cherenkov detectors, also called stations, disposed in a triangular grid. One array is composed of 1600 stations separated by 1500 m from their closest neighbors. There is also a smaller infilled array where the distance between stations is 750 m. Each station has a cylindrical-shaped tank with 12000 litres of ultra-pure water contained in a liner. On top, three symmetrically-placed photomultiplier tubes look into the water volume. They collect Cherenkov light produced when charged particles cross the water volume with a speed greater than that of light in water. The station is self-powered by two solar panels combined with two auxiliary batteries which allow it to operate almost 100% of the time. The components of a surface-detector station can be seen in Fig. 3.4.

3.2.1 The water-Cherenkov detectors

The water-Cherenkov detectors have 3.6 m of diameter and a height that does not exceed 1.6 m so that they can be transported within regulations. They are coloured beige to blend with the local landscape.

The structure of the stations is made of high-density polyethylene using the process of rotational molding, or "rotomolding" [10, 12]. This process consists in depositing a certain amount of polyethylene powder inside a mold placed in an oven. As the powder melts the mold is rotated. In the end, a robust and low-cost structure is obtained. The station wall, with thickness 13 ± 3 mm, is composed of two layers, the outer one is beige and the inner, spanning two thirds of the total thickness, is black thus providing a dark interior.

On top of the station, three hatches, one large with 560 mm of diameter and two smaller ones with 450 mm diameter, give access to the interior. In order to prevent rain water from accumulating, the hatches are elevated, as can be seen in Fig. 3.4. Hatchcovers are fixed with screws. On top of the large one there is a dome forming an enclosure to the station electronics (see Fig. 3.4).

The battery box is also made from polyethylene using the rotomolding process. It is placed in the tank facing South so that it is protected from direct sunlight. It is thermally isolated by 50-mm sheets of polystyrene foam.

The station is powered by two 55-Wp (Watt-peak) solar panels that charge two 12-V batteries connected in series. The panels face North forming an angle of 55° with the upward direction to maximize sunlight collection. This setup provides the 10 W required by the station electronics, and should make the station operational more than 97% of the time.

Power cables run from the solar panels to the electronics enclosure and then, through the station interior, to the battery box. Sensors are installed to monitor the voltages, electric currents and temperatures of the batteries and photomultiplier tubes every six minutes. The station control board allows to remotely shutdown the station. It is also possible to shutdown the entire array.

The water volume is contained inside a liner made of a low-density polyethylene film. Its interior is covered by a Tyvek layer to diffusely reflect UV Cherenkov light produced in the water. The liner also has the function of preventing any external light of reaching the interior of the water volume. Three dome windows are present to give optical access for the photomultiplier tubes, besides five smaller ports allow water to be filled inside the liner as well as provide windows for LED flashers which are used to test the photomultiplier tubes. A picture of an inflated liner during a test to assure that no holes are present is shown in Fig. 3.5.

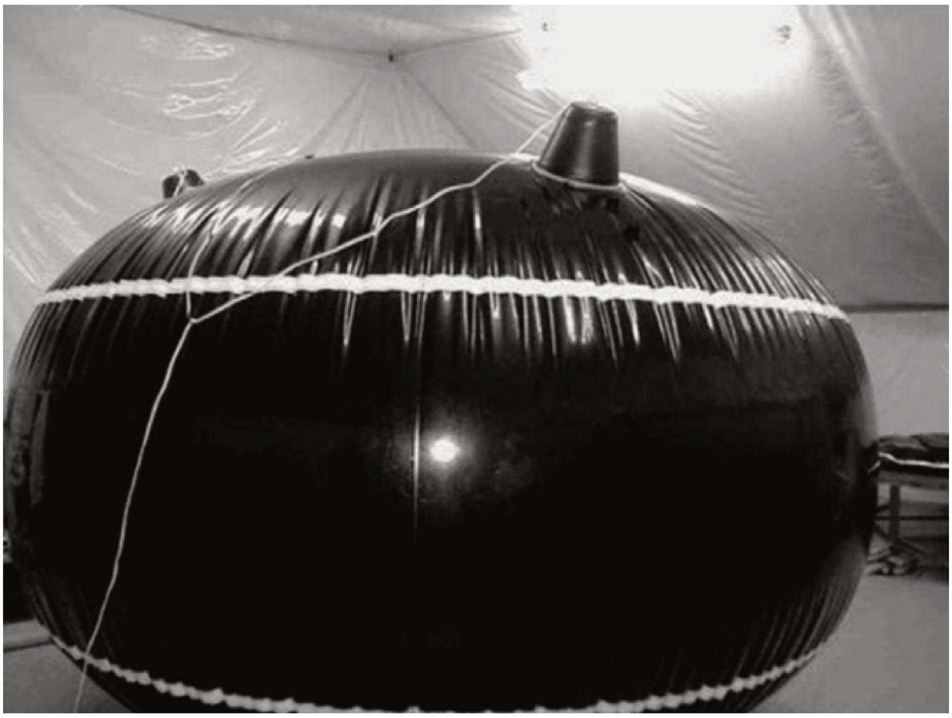

Figure 3.5: An inflated liner during test to assure no holes are present. The PMTs enclosures can also be seen on top of the liner [12].

The ultra-pure water which is filled into the liner is free of nutrients and microorganisms, thus preventing attenuation of Cherenkov light propagating inside the water volume, and guaranteeing stability during the Observatory operation. The filled liner has a water height of 1.2 m. The water is produced in a plant at the Observatory campus which is owned and maintained by the Collaboration.

An antenna allows the station to communicate with the central data acquisition system (CDAS). Close to it, a GPS receiver is installed for event timing and communication synchronization. Both antennas can be seen in Fig. 3.4.

The three photomultiplier tubes (PMTs) used in the detector are Photonis XP1805/D1 with eight dynodes and a diameter of nine inches [13]. They are symmetrically placed at 1.20 m from the station's central axis. The PMTs are contained inside an enclosure to prevent outside light from reaching them as well as keeping them protected from the external environment. Figure 3.6 shows a picture of the PMT model used and a schematic drawing of the enclosure which can also be seen in Fig. 3.5.

High voltage is provided to the PMTs by a module in their base. It is proportional to a DC control voltage supplied locally by the slow control system. Each PMT outputs two signals, one from the anode and another obtained from the last dynode which

(a) (b)

Figure 3.6: (a) Photomultiplier tube model XP1805/D1 with 9-in diameter [13]. (b) Schematic drawing of the PMT enclosure [10].

is inverted and amplified by 32 times the anode charge gain.

The signals are filtered by a 5-pole Bessel filter, then they are digitised by a semi-flash analog-to-digital converter (ADC) with 10 bits at a frequency of 40 MHz. Combining the use of 10-bits ADCs with dynode signals amplified 32 times yields a 15-bits dynamic range for the system [10].

The outputs of the ADCs are analyzed and stored in a buffer memory by a programmable logic device, which informs the station microcontroller when a trigger occurs. The microcontroller communicates the local triggers to CDAS, which in the case of time coincidence with nearby stations, requests local data to build an event. More information on triggers with the surface detector will be presented later. A unified board implements the station controller, event timing, slow control functions and communications system, thus providing a front-end interface.

3.2.2 Calibration of the photomultiplier tubes

The photomultiplier tubes of the stations are calibrated to convert the charge of the signals read by the ADCs, in hardware unit (integrated ADC channels), to a physical unit which reflects the amount of particles that crossed the detector. The chosen unit is the *vertical equivalent muon*, or VEM, defined as the average charge produced in the PMTs by a vertical muon crossing the centre of a station. Besides providing a common reference for all stations of the surface detector array, the calibration also allows an easier comparison to simulations.

The calibration also determines, in ADC channels, the peak of the pulse-height distribution produced by atmospheric muons. This value is used to set the station local triggers, therefore providing uniform conditions of trigger for the entire surface detector array.

By itself, a station is not able to select only vertical muons to perform the calibration, therefore an indirect reliable method must be applied. Using a reference station, the charge spectrum of background charged particles, shown in Fig. 3.7a, was obtained [14–16]. A 3-fold coincidence between the three PMTs was used as trigger and the charge values are the sum registered by the three PMTs. It is possible to see two peaks in this plot. The first one is due to particles such as electrons and high-energy gammas, which produce electron-positron pairs in the water volume. The second peak is due to atmospheric muons. Using plastic scintillators placed above and under the reference station, the charge distribution of vertical central-going muons was also obtained, represented by the dashed red line in Fig. 3.7.

It was found that the peak in the distribution of atmospheric muons has charge of approximately 1.09 VEM for the sum of the three PMTs and 1.03 ± 0.02 VEM for each PMT [14, 16]. This difference occurs because the sum of the three PMTs represents the total signal whereas each PMT registers only part of it. The shift in the peak produced by background atmospheric muons, in relation to the vertical ones only, is understood as caused by different track lengths traversed by background muons arriving with different angles at the station, as opposed to the fixed length vertical muons cross [15].

Given the relation between the peak in the charge distribution of atmospheric muons (Q_{μ}^{peak}) and the average charge of a vertical centre-going muon (VEM or Q_{VEM}), the calibration of the PMTs is achieved performing the following few steps.

First, the end-to-end gains of the PMTs are adjusted so that the singles rate at 150 ADC channels above baseline be 100 Hz. This causes the peak of the pulse-height distribution produced by atmospheric muons (I_{μ}^{peak}) to be at approximately 50 ADC channels. As a consequence of this procedure, the stations will not necessarily have the same gains, if the water quality in a tank yields better propagation of photons than in another, the first will have a lower gain. Even in the same station the gain of the PMTs

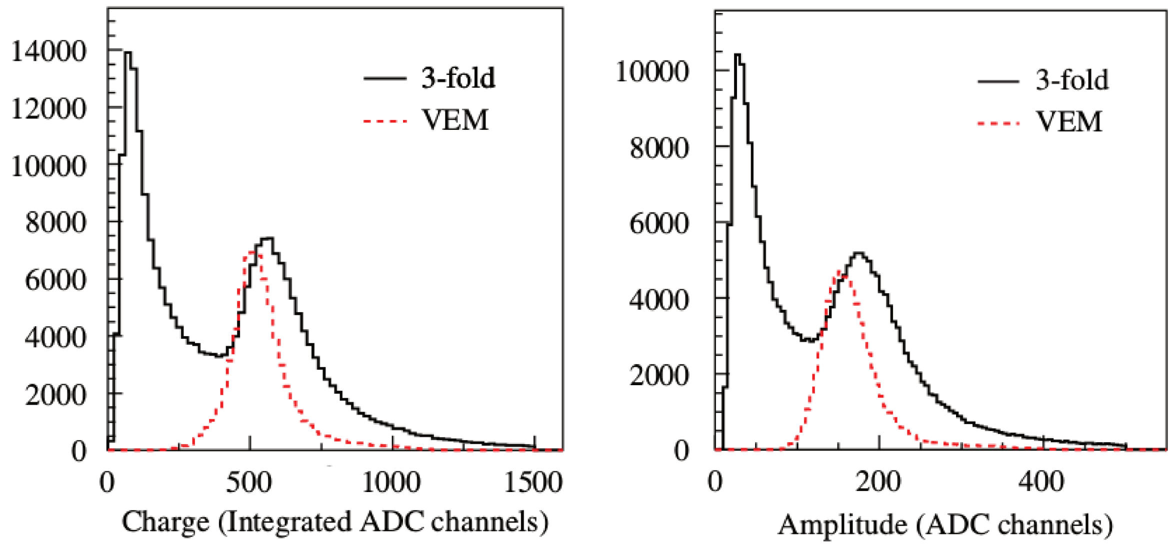

(a) (b)

Figure 3.7: (a) Charge histogram produced by atmospheric charged particles crossing a reference station (black). Using plastic scintillators placed above and under the station, the spectrum for vertical central-going muons was also obtained (red). (b) The corresponding histogram showing the signal pulse-height distribution for vertical muons and charged background particles. [16].

might differ, for instance, if a PMT has a worse optical coupling with the water volume it will operate in a higher gain.

After the gain adjustment, there are drifts of I_{μ}^{peak} from 50 ADC channels. To compensate for these drifts and determine I_{μ}^{peak}, an on-line continual procedure is applied. The most natural way to do it would be to produce a peak-height histogram, such as the one in Fig. 3.7b (black line), and directly obtain I_{μ}^{peak} in ADC channels. Unfortunately, this would make the dead time of the station too long. Instead an estimation of I_{μ}^{peak} ($I_{peak}^{est.}$) is obtained by requiring that the event rate satisfying a "calibration trigger" be 70 Hz. The calibration trigger is defined as a threshold trigger of $2.5I_{peak}^{est.}$ for the given PMT and $1.75I_{peak}^{est.}$ for all three. These values were obtained from the reference station. A convergence algorithm is applied to determine the value of $I_{peak}^{est.}$. The full algorithm is explained in Ref. [16]. The determination of $I_{peak}^{est.}$ is within 6% precision from I_{μ}^{peak}. As mentioned before, the local triggers are defined in terms of the estimation of I_{μ}^{peak} thus providing uniform triggers for the entire surface detector array.

Finally, the value of Q_{VEM} is determined in hardware units from charge histograms. A threshold trigger of $0.1 I_{peak}^{est.}$ is used to gather events for 60 s, yielding some 150,000 events. From these events, the following histograms are created:

- charge histogram for each PMT,
- charge histogram of the sum of the three PMTs,
- pulse-height histogram for each PMT,
- histogram containing the baseline of each PMT,

and also the average pulse shape of events with charge of $(1.0 \pm 0.1) Q_{\mathrm{VEM}}$. An example of these histograms is shown in Fig. 3.8.

Once an event is requested by CDAS, the corresponding calibration histograms, created in the last minute, are also sent attached. Then, during data analysis, the second peak of the charge histograms is fitted to a quadratic function and, using the known relation, the VEM charge is obtained in hardware unit.

3.2.3 Surface detector triggers

Several detectors of the surface array are hit by particles produced in highly energetic extensive air showers. Trigger conditions are set to identify such showers and select the ones of interest, i.e., ultra-high energy events. Here the surface detector triggers will be described as well as how they are used to select shower events.

Each water-Cherenkov detector has two levels of local triggers, T1 and T2. There are two types of T1 trigger. A simple threshold trigger (T1-TH) requires that all three PMTs of the station have signal amplitude larger than $1.75 I_\mu^{peak}$. This trigger is effective to detect very inclined showers, as their signals are not necessarily spread in time.

The other type of T1 is a time-over-threshold trigger (T1-ToT). It requires that the signal of at least 13 bins with size 3 μs be larger than $0.2 I_\mu^{peak}$ for two out of the three PMTs. This trigger tends to select vertical showers, more specifically low-energy showers close to its core or high-energy showers far from its core, since their signals are smaller and spread in time.

The second level of local trigger is T2. All T1-ToT triggers are automatically promoted to T2 (T2-ToT). In the other hand, for a T1-TH trigger to become a T2 (T2-TH) trigger the signal in all three PMTs must be larger than $3.2 I_\mu^{peak}$. Once a station

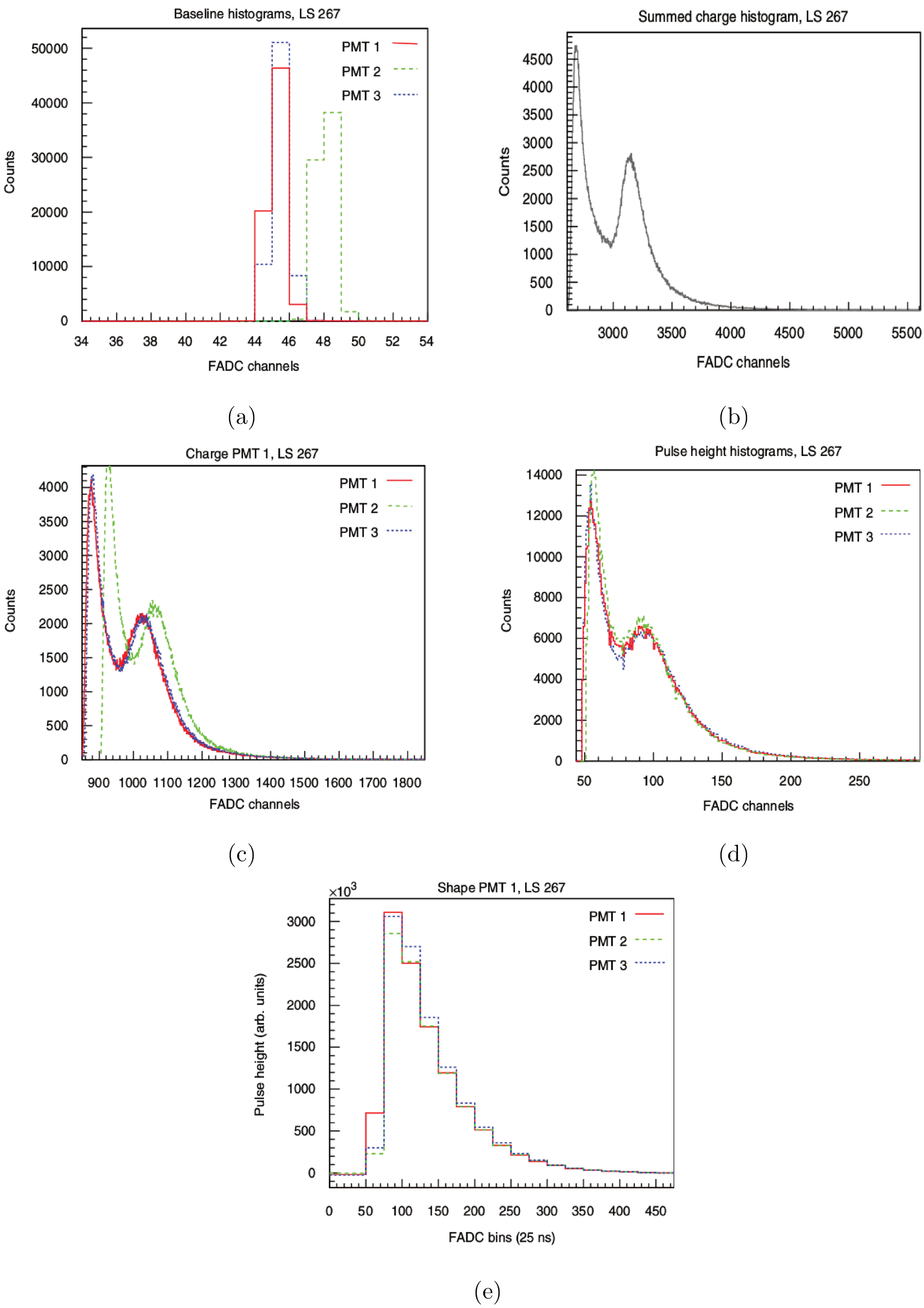

Figure 3.8: Calibration histograms. (a) Baseline. (b,c) Charge histograms. (d) Pulse-height histograms. (e) Average shape of $(1.0 \pm 0.1)Q_{\mathrm{VEM}}$ signals [16].

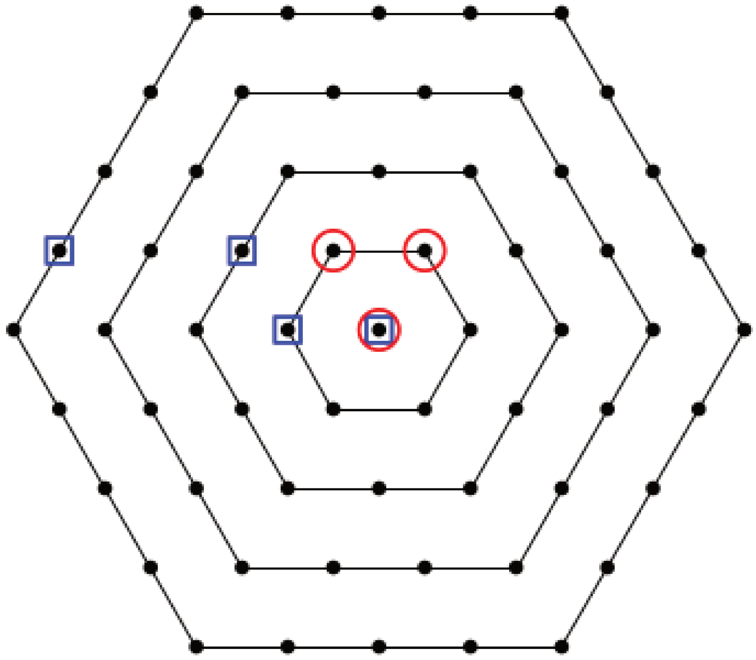

Figure 3.9: System of concentric hexagons centred on one of the surface stations. It is used in the analysis of spatial coincidence of T2-triggered stations. Two spatial conditions represented by the red circles and blue squares may be satisfied (see text for description of such conditions) [10].

has a T2 trigger occurrence its timestamp is sent to the central data acquisition system (CDAS).

An analysis of the received T2 triggers for spatial and time coincidence of the surface detectors is performed at CDAS to produce a level-3 trigger (T3) and identify a shower event. First, the received T2 triggers are clustered in time by setting a ± 25 μs interval centred on each T2. Groups with three or more stations with T2 triggers clustered together are selected for spatial analysis. A system of concentric hexagons centred on each station of the clustered group, such as shown in Fig. 3.9, is defined for the spatial analysis.

Two spatial conditions may be satisfied by a clustered group of stations to produce a T3 trigger:

1. at least three detectors triggered with a T2-ToT with one detector having one of the others in the first hexagon and the second no further than the second hexagon.

2. A coincidence of four stations with T2 of any type and the spatial requirement that one of the stations may be as far as the fourth hexagon, if another station is within

the first and another no further than the second hexagon.

An example of the first criterion is represented in Fig. 3.9 by the red circles. The blue squares illustrate an example of the second criterion.

After one of the spatial criteria is met, the T2 triggers must be within $(6 + 5n)$ μs of the central station, where n is the hexagon number, for a T3 trigger to be assigned. Once a T3 trigger is identified, CDAS requests all ADC traces within 30 μs of the central T2 trigger of the participating stations to build an event.

3.3 Event reconstruction with the surface detector

The Pierre Auger Observatory detects extensive air showers produced by high-energy cosmic rays. When the particle front of an EAS passes through the surface detector stations, they register a signal, proportional to the particle density, as well as the times such particles crossed them. Using these data one can reconstruct the shower and determine quantities such as its arrival direction and energy. Here the process to obtain these quantities from vertical showers (zenith angle smaller than 60°) detected by the 1500 m surface detector array will be described.

Figure 3.10a shows a particle front crossing some stations. The time of the signal registered by the stations is fit to a model which describes the propagation of the particle front. For events with few stations triggered, a plane front is used. However, with more stations participating in the event a model considering a speed-of-light inflating sphere is applied, so that

$$|\vec{x}_i - \vec{x}_{sh}| = c\,(t_i - t_0) \tag{3.1}$$

with $\vec{x}_{sh}$ the point where the shower started, on time t_0, and $\vec{x}_i$ is the position of the i^{th} station hit by the particle front at time t_i. An example of a fit to a plane front model is shown in Fig. 3.10b where time is plotted as a function of the perpendicular distance to the shower axis. This method allows one to determine $\vec{x}_{sh}$ which gives approximately the primary particle arrival direction.

The signal charge of the stations participating in the event are fit, using a maximum likelihood method, to a function which describes the particle density in an EAS as a function of the perpendicular distance to the shower core. Such a function is called the *lateral distribution function* (LDF). In Fig. 3.11, the signals registered for an

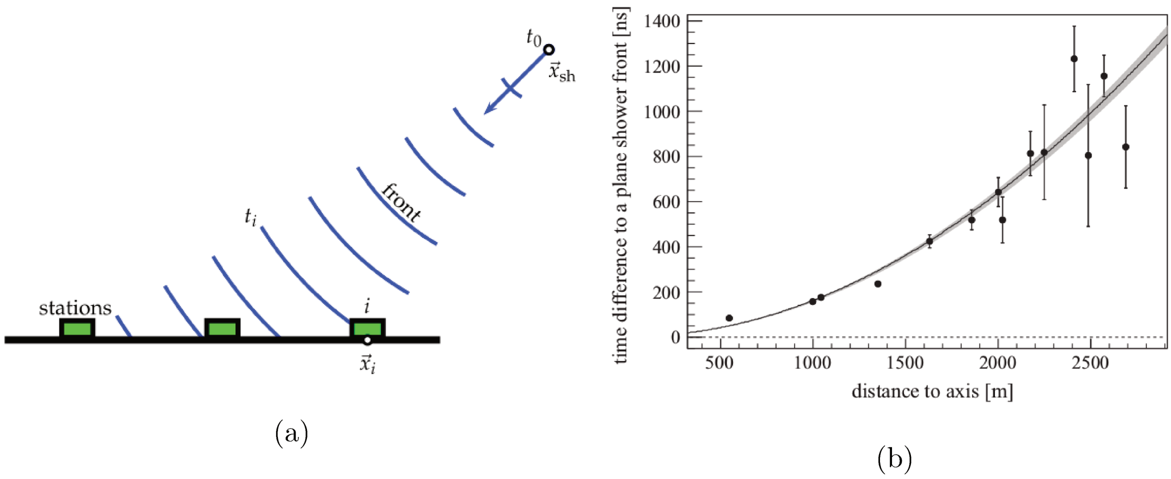

Figure 3.10: (a) Propagation of a shower particle front, the shower starts at $(\vec{x}_{sh}, t_0)$ and cross station i at $(\vec{x}_i, t_i)$. (b) Fit of time registered by stations to a front propagation model; the trigger times of the stations are plotted as a function of the perpendicular distance to the shower axis [10].

event are plotted as a function of their distances to the shower axis along with the LDF fit. Note that the signals are expressed in VEM unit.

For the LDF fit, a modified Nishimura-Kamata-Greisen function

$$S(r) = S(r_{opt}) \left(\frac{r}{r_{opt}}\right)^{\beta} \left(\frac{r + r_1}{r_{opt} + r_1}\right)^{\beta+\gamma} \tag{3.2}$$

is used, where $r_1 = 700$ m and r_{opt} is the optimum distance at which variations in the signal due to the choice of LDF used for the fit are minimized. It depends mainly on the geometry of the detector and for the 1500 m array $r_{opt} = 1000$ m [17]. $S(r_{opt})$ is the signal at the optimum distance, and is the observable chosen to mirror the shower size since it presents minimum dependence on the LDF used for the fit. As $r_{opt} = 1000$ m, $S(r_{opt})$ is $S(1000)$, the signal at 1000 m from the shower core which can be seen in Fig. 3.11. The parameter β depends on the zenith angle, since inclined events are detected at ground level at later shower age than vertical ones.

From the fit of the signals to an LDF one obtains the shower impact point on the ground (where the shower core hits the ground) $\vec{x}_{gr}$. Using the position where the shower originates, $\vec{x}_{sh}$ (see Fig. 3.10a), obtained from the time fit, the arrival direction of the primary cosmic ray can be determined from

$$\hat{a} = \frac{\vec{x}_{sh} - \vec{x}_{gr}}{|\vec{x}_{sh} - \vec{x}_{gr}|} \ . \tag{3.3}$$

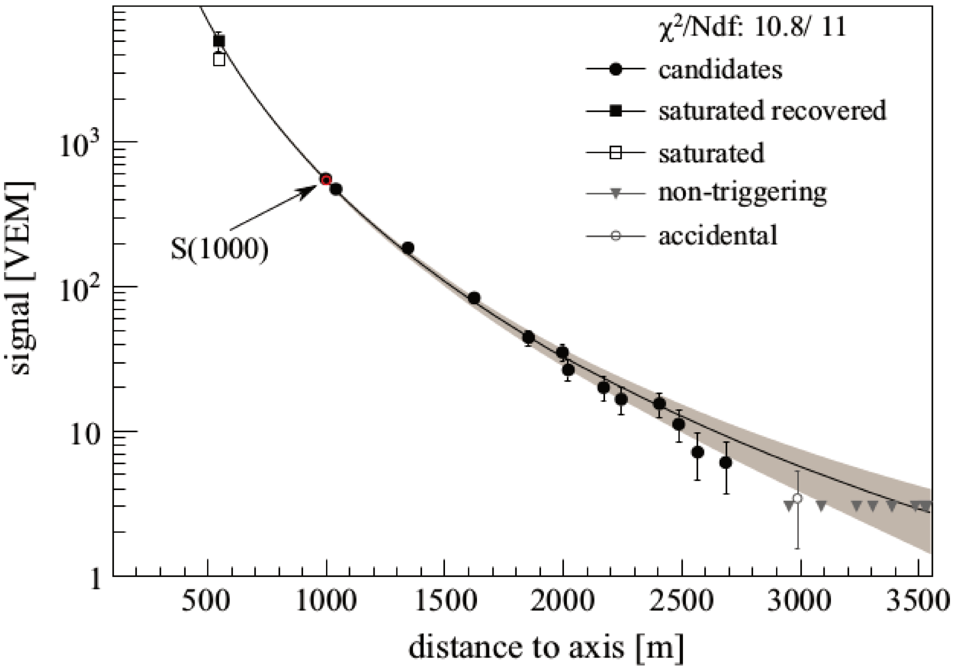

Figure 3.11: Fit of station signals to a modified Nishimura-Kamata-Greisen function which describes the lateral distribution of particles in an EAS. The signal at 1000 m from the shower core, $S(1000)$, is obtained from the fit [10].

The resolution on the arrival direction improves with increasing zenith angles and is constrained by the number of stations triggered in the event: the more stations the better the resolution. For events with three triggered stations, the resolution is better than 1.6°, with six or more it becomes better than 0.9° [10].

The energy determination of an event with the surface detector array relies on data from hybrid events. Therefore, energy determination with the fluorescence detector will be briefly explained.

When an extensive air shower develops in the atmosphere, the shower particles induce fluorescence light emissions from atmospheric molecules of nitrogen, at the same time as the shower particles produce Cherenkov radiation. This light is collected by the fluorescence telescopes, producing signals in different pixels of the telescope camera as the shower develops (each pixel covers a small part of the sky). The position of the shower axis is determined by performing a fit to the time of signals registered in the camera pixels. This determination is considerably improved by combining timing information from at least one surface detector station yielding a typical arrival direction resolution of 0.6° [11].

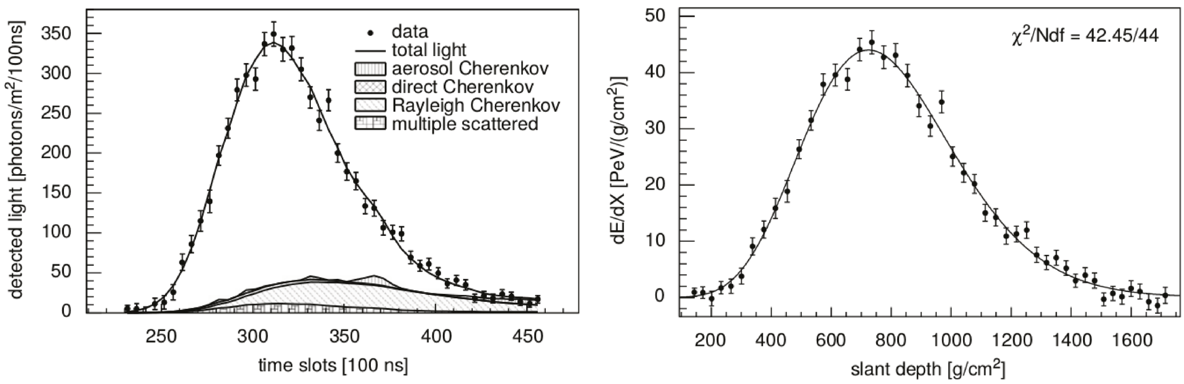

(a) (b)

Figure 3.12: (a) Light flux measured by the telescope as a function of time for an event. (b) Energy deposit profile obtained from converting the light flux and time to energy and slant depth respectively [11].

The amount of light collected by a telescope aperture as a function of time is shown in Fig. 3.12a, for an event. The shape of the shower longitudinal profile can already be seen. In order to convert light flux to energy deposit, the attenuation of light from the shower to the telescope is estimated as well as the different light components (fluorescence light, direct and indirect Cherenkov radiation and multiple-scattered light). These components are also observed in Fig. 3.12a. In this manner, Fig. 3.12b shows the energy deposit as a function of the slant depth. A Gaisser-Hillas function is fit to the energy deposit profile, then it is integrated to obtain the total energy. A correction obtained from Monte Carlo simulation is performed to account for the "invisible energy" of neutrinos and high-energy muons. The energy resolution, from statistical uncertainty, is 10% and the systematic uncertainties sum up to 22% [11].

As mentioned before, the shower size is represented by $S(1000)$, the signal at 1000 m from the shower core, obtained from the LDF fit. For a given energy, $S(1000)$ decreases with zenith angle, as inclined events reach the ground at later shower development compared to vertical ones. Assuming an isotropic cosmic-ray distribution, the attenuation of $S(1000)$ with zenith angle θ is obtained from the experimental data using the *constant intensity cut* (CIC) method [18]. The attenuation shape is fit with a third-degree polynomial in $x = \cos^2\theta - \cos^2\bar{\theta}$

$$f(\theta) = 1 + ax + bx^2 + cx^3 \;, \tag{3.4}$$

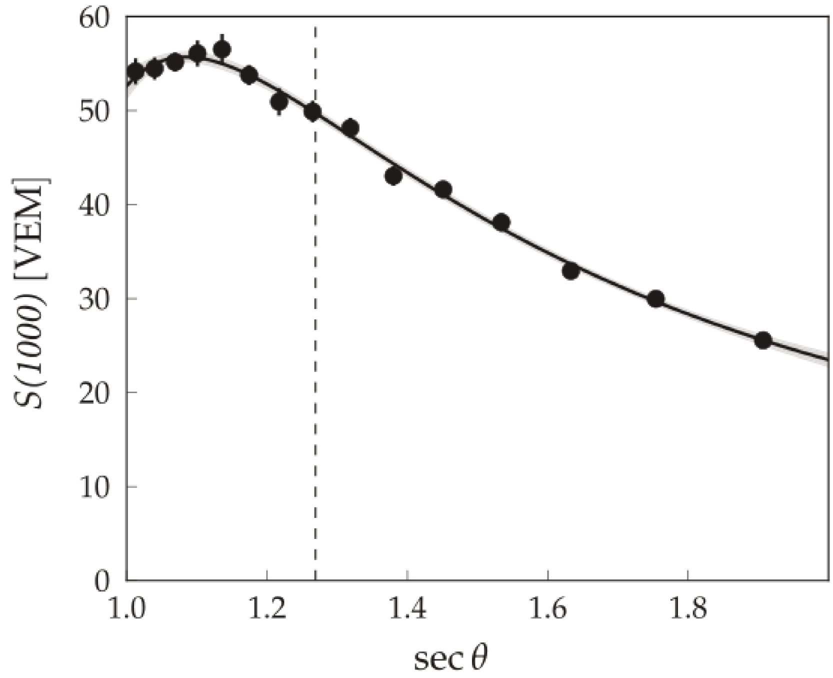

Figure 3.13: Attenuation of $S(1000)$ with zenith angle θ. A third degree polynomial in $x = \cos^2\theta - \cos^2\bar{\theta}$ is used to describe the attenuation. The angle $\bar{\theta} = 38°$ is the median of an isotropic distribution and is represented by the dashed line [10].

where $a = 0.980 \pm 0.004$, $b = -1.68 \pm 0.01$ and $c = -1.30 \pm 0.45$ [10]. In Fig. 3.13, $S(1000)$ is plotted as a function of $\sec\theta$, the fit curve can also be observed. The angle $\bar{\theta} = 38°$ is the median of an isotropic distribution. Expression 3.4 is used to convert $S(1000)$ to S_{38} defined as

$$S_{38} \equiv \frac{S(1000)}{f(\theta)} \; . \tag{3.5}$$

S_{38} can be interpreted as the $S(1000)$ value the shower would have if it arrived with zenith angle of 38°.

It is possible to correlate S_{38} with the shower energy. The advantage of the hybrid design of the Observatory now comes into the scene. Events detected simultaneously by the surface and fluorescence detectors offer a means to calibrate the surface detector array, and therefore it is not necessary to rely on Monte Carlo simulations to determine the energy of events detected only by the array of surface stations.

The hybrid events used in this calibration are required to have all the six closest neighbors to the station with the highest signal, a complete hexagon, working at the time of the event [19]. A plot of S_{38} as a function of the energy obtained from the fluorescence

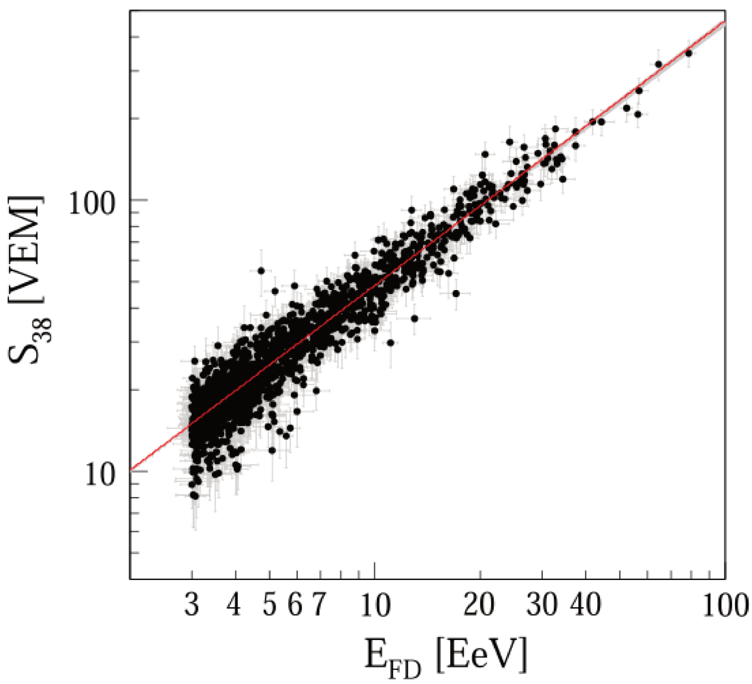

Figure 3.14: S_{38} as a function of the energy measured with the fluorescence detector. A single-power law fit is applied. This relation can be used to compute the energy of events detected only by the surface detectors [10].

detector, E_{FD}, is presented in Fig. 3.14. As expected, the shower size increases with the primary energy. A single-power law function

$$E_{FD} = A(S_{38}/VEM)^B \tag{3.6}$$

is used to describe the relation between S_{38} and E_{FD}. The coefficients A and B have values $(1.90 \pm 0.05) \times 10^{17}$ eV and 1.025 ± 0.007 respectively [20].

Combining Eqs. 3.4, 3.5 and 3.6 one obtains the energy estimation for an event detected by the surface detectors

$$E_{SD} = A \left(\frac{S(1000)}{1 + ax + bx^2 + cx^3} \right)^B \quad , \tag{3.7}$$

with $x = \cos^2\theta - \cos^2\bar{\theta}$ and $S(1000)$ in VEM unit. The energy resolution from the surface detector is 16% for low energies and 12% for high energies [10]. This effect is clear from the plot in Fig. 3.14 where the S_{38} distribution becomes narrower with increasing energy.

In summary, the surface detectors measure signals and their times as a shower particle front crosses the stations. By fitting the trigger time of the stations to a model describing the propagation of the shower particle front, and the signals to an LDF, it is possible to identify the position of the shower core and determine the arrival direction of the primary particle. For the energy estimation, the signal at 1000 m from the shower axis, $S(1000)$, obtained from the LDF fit, is converted to S_{38}, the $S(1000)$ signal the shower would have if it had arrived with a zenith angle of 38°. A relation between S_{38} and the energy measured by the fluorescence detector is obtained from hybrid events. Such relation is then used to estimate the energy of the primary particles detected only with the surface detectors. Using this approach, the use of Monte Carlo simulations is not necessary, thus a much more reliable result is obtained.

3.4 Observatory upgrade

The construction of the Pierre Auger Observatory was completed in 2008. Its copious amount of high-quality data has increased our understanding of cosmic rays at the highest energies. However these discoveries also brought more questions. The Observatory is currently being upgraded to shed some light into these questions.

In this section some of the notorious results obtained by the observatory will be presented. The need of more sensitive measurements will be explained as well as the means to achieve it. A description of the upgraded observatory will be given.

3.4.1 Observatory results

The data collected by the Pierre Auger Observatory allowed obtaining the differential flux of cosmic rays for the highest part of the energy spectrum with unprecedented precision. Figure 3.15 shows such cosmic-ray spectrum obtained from the surface detectors (1500 and 750 m arrays) as well as hybrid events [21]. It is possible to observe a clear suppression of the flux for energies above 3.9×10^{19} eV. The origin of the suppression is still not certain, since different models try to explain it. It could arise from the maximum energy output at the sources or from interactions of the cosmic-ray particles with the cosmic background radiation, as predicted by the GZK effect. Unfortunately, the current mass composition sensitivity of the Observatory is not enough to elucidate this question.

The observation of longitudinal profiles of showers with the fluorescence detector allows the determination of the depth of maximum shower development, X_{max}, offering a means to estimate the mass of the primary particle. The X_{max} mean and its

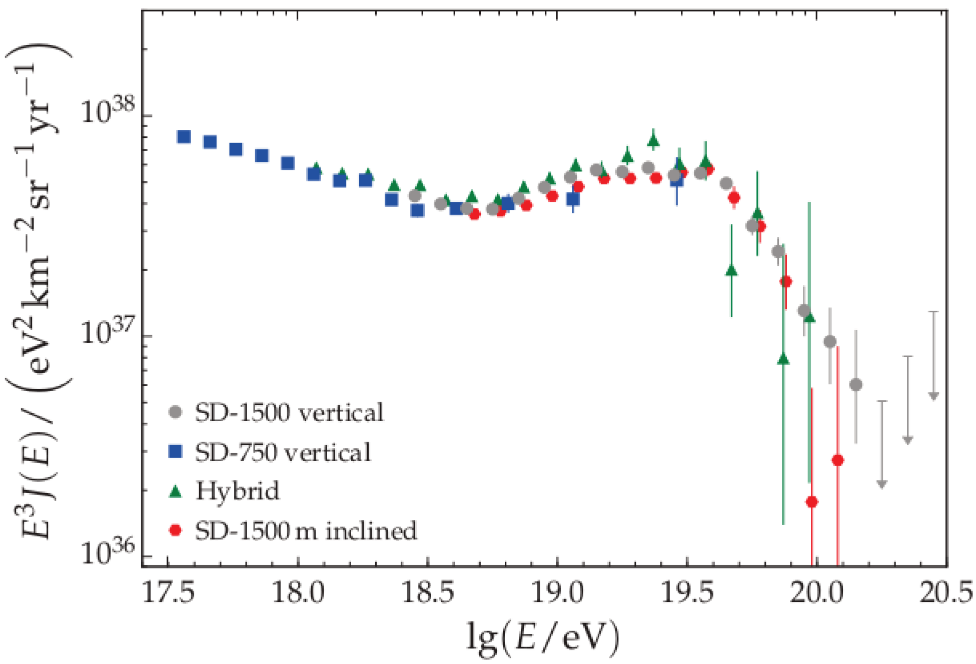

Figure 3.15: Energy spectrum of cosmic rays obtained from data of the 1500 and 750 m surface detector arrays as well as from hybrid events. The existence of a flux suppression above approximately 3.9×10^{19} eV is clear [21].

dispersion is given as a function of the shower energy in Fig. 3.16, where the predicted behavior from Monte Carlo simulations for proton and iron primaries is also shown [1]. The mean X_{max} favours a light composition up to energies of 3×10^{18} eV when, quite surprisingly, X_{max} starts to have a tendency towards heavier elements. Such behaviour is confirmed by the X_{max} dispersion. Due to the low duty cycle of the fluorescence detector (about 15%), the statistics of data for energies above 3×10^{19} eV, the suppression region, is still very sparse. In Fig. 3.16 the last data point represents all events with energy above 3×10^{19} eV. It is important to have in mind that the interpretation of X_{max} data using simulations relies on extrapolations of the current hadronic interaction knowledge to energy ranges way above the one covered by accelerator data.

The number of muons produced in a shower cascade is closely related to the hadronic interactions taking place during shower development. With the surface detector it is possible to indirectly measure the number of muons in inclined showers, for which the ground signal is dominated by the muonic component. Figure 3.17a shows the logarithm of the mean number of muons observed relative to that produced in showers induced by a proton with energy 10^{19} eV. Results of simulations using different hadronic interaction

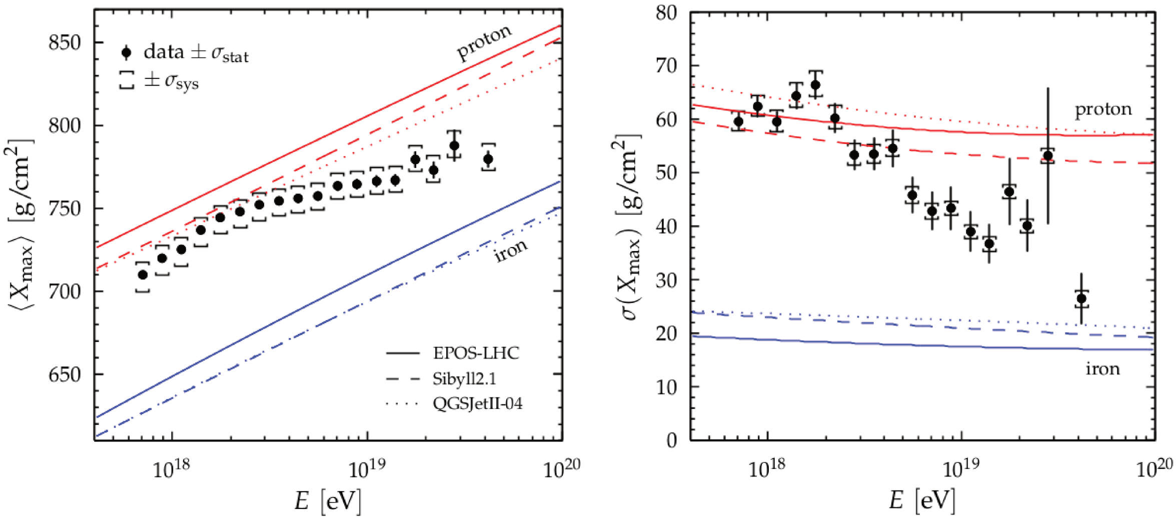

(a) (b)

Figure 3.16: X_{max} mean (a) and its dispersion (b) as a function of energy. The behavior for proton and iron-induced showers obtained from simulations is shown. For energies above 3×10^{18} eV, there is a tendency in X_{max} to favour a heavier composition for the primary particle [1].

models are also presented. It is clear that none of the simulation models can describe the data. Figure 3.17b shows the scaling factors R_μ and R_E necessary to correctly describe the number of muons and energy, respectively, measured by the Pierre Auger Observatory, when different hadronic interaction models are applied. Again the simulations fail to properly describe the data. These results strongly suggest that the current understanding of hadronic interactions is incomplete, especially for such high energies.

3.4.2 Upgrade proposal

In face of the results presented above, it is necessary to improve the Observatory sensitivity to the mass composition of the primary particles, so that an explanation for the suppression can be provided among the several existing models. Improved statistics on the composition data is also required, since at present the most precise method to obtain composition information is from $\langle X_{max} \rangle$ observed with the fluorescence detector, which has a low duty cycle.

In order to obtain the desired composition data, it is planned to measure separately the muonic and eletromagnetic components of extensive air showers with a

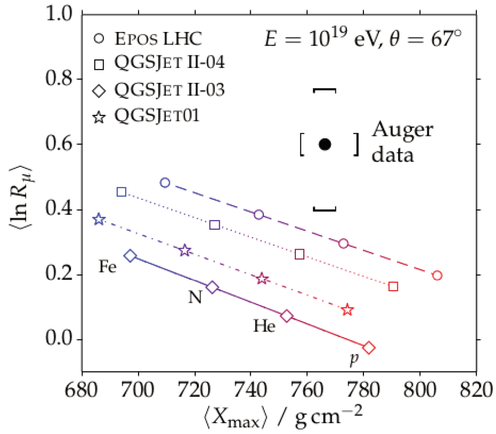

(a)

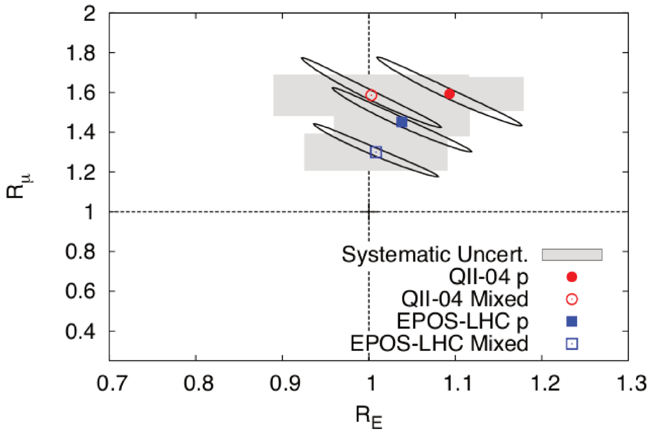

(b)

Figure 3.17: (a) The number of muons relative to that produced in a proton-induced shower with energy 10^{19} eV as a function of $\langle X_{max} \rangle$. Results for different hadronic interaction models are also shown. (b) Scaling factors R_μ and R_E necessary for simulations to describe the muon number and energy, respectively, observed by the Pierre Auger Observatory [1].

ground array. The number of muons produced in a shower is related to the mass of the primary cosmic-ray particle, as explained in Chapter 2. Such measurement may also provide valuable data to elucidate the mystery of muon excess observed at the Observatory as well as to study hadronic interactions in energy ranges far beyond those probed by human-made accelerators.

Figure 3.18 shows the number of muons at maximum shower development as a function of X_{max}, obtained from shower simulations for different primaries with energy 5×10^{19} eV and zenith angle 38°. The 1σ contour is shown. A clear separation between heavy and light composition is achievable. With enough statistics it is even possible to distinguish mid-range composition, such as nitrogen, from lighter and heavier elements.

The following enhancements to the Observatory are planned to achieve the science goals by measuring the muonic and electromagnetic components of extensive air showers [1, 22]:

- installation of a plastic scintillator detector with dimensions 3.8 m $\times$ 1.3 m on top of each surface detector. The complete array of scintillators will be called the *surface scintillation detector* (SSD).

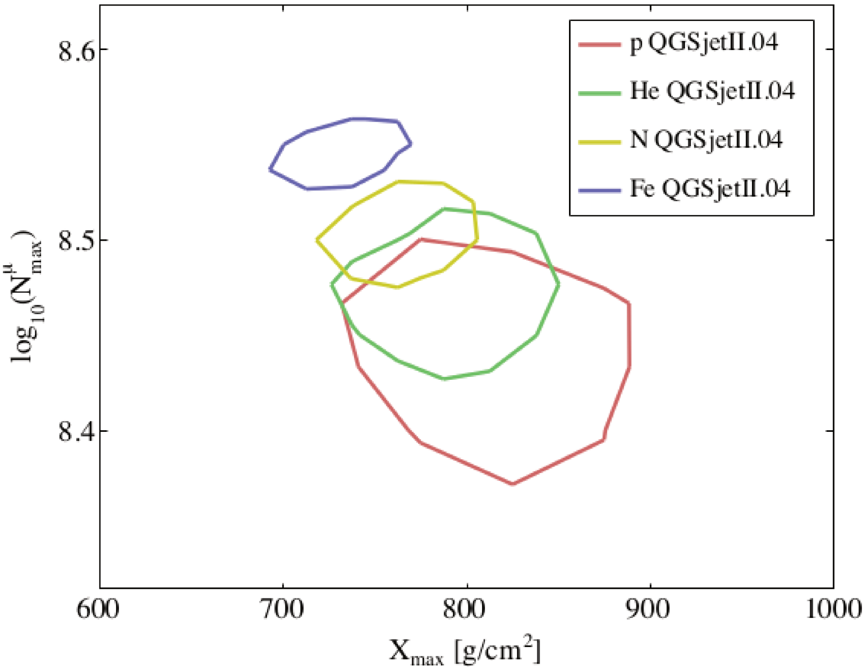

Figure 3.18: The 1σ contour of the number of muons as a function of X_{max} for different simulated primaries with energy 5×10^{19} eV and 38° zenith angle. The hadronic interaction model used in the simulations was QGSJetII.04 [1].

- New electronics will be provided to the SD stations with higher sampling rate of 120 MHz. Installation of an additional small area photomultiplier tube will extend the dynamic range of the SD stations by a factor of about 32. The new electronics will also be used to trigger the SSD by the SD.
- Underground muon detectors will be installed close to the 750 m array stations providing direct measurement of the muon content in air showers. It will be used as cross-check to the SSD and SD signals.
- The fluorescence detector will have its duty cycle increased by reducing the gain of the PMTs when moonlight is present in the sky.

Figure 3.19 shows a scintillator detector mounted on top of an SD station. The measurement of the muonic and eletromagnetic components of air showers will rely on the different responses produced by the scintillator and water-Cherenkov detector to each of these components. More details of how each component is extracted from the SSD and SD signals are presented in Refs. [1, 22].

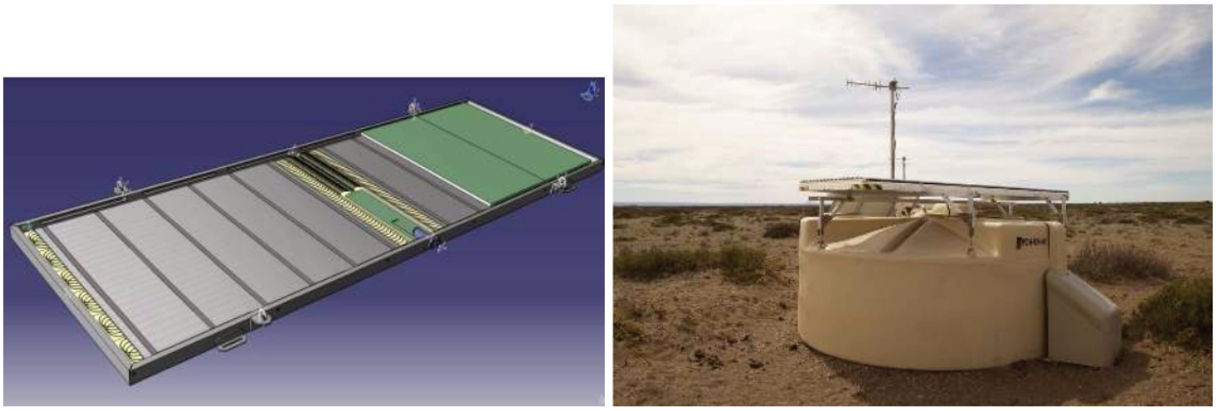

Figure 3.19: Scintillator detector layout (left), and mounted on top of a surface detector station (right) [22].

The work presented in this dissertation concerns the implementation of the additional small area photomultiplier to extend the dynamic range of the water-Cherenkov detectors. The next chapter is dedicated to its proposal and expected performance.

Chapter 4

Small photomultiplier tube proposal

In this chapter, the origin of saturation on the surface detectors of the Pierre Auger Observatory is discussed as well as its impact on event reconstruction. The proposition of using a photomultiplier tube of small area to overcome saturation will be presented along with the expected benefits it will bring to the performance of the water-Cherenkov detectors and event reconstruction. The plans for the implementation of this upgrade will be pointed out. A test with ten experimental stations was done to assess the performance of the small PMTs in the field, from which data for this project was obtained. This experimental setup will be described.

4.1 Saturation problem

Ultra-high energy cosmic rays produce extensive air showers in the Earth atmosphere. Such showers are composed of several particles with its number being larger the closer to the core. Surface-detector stations near a shower core will therefore have many charged particles crossing them. These particles, in turn, will produce copious amounts of Cherenkov photons when they cross the water volume of a station. With such high photon density in the water volume, the photomultiplier tubes might saturate.

The footprint of an extensive air shower on the ground can extend over a large area, for instance, a cosmic ray of 10 EeV can produce a shower spreading more than 20 km^2 on ground level. The footprint on the surface detector array of a real event is shown in Fig. 4.1a. Colours represent the times of the triggered stations from early (light yellow) to late (dark red). The radius of the markers is proportional to the logarithm of

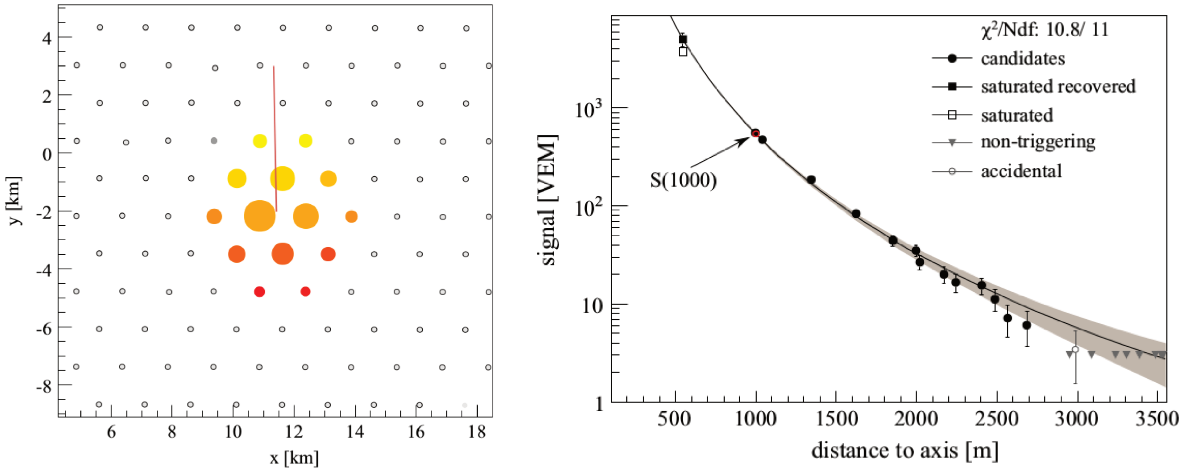

(a) (b)

Figure 4.1: (a) Footprint of an extensive air shower on the surface detector. Light yellow represents early trigger times and dark red later ones. The marker size is proportional to the logarithm of the signal. (b) Signal in the triggered stations as a function of distance to the shower axis. The two stations closest to the shower core presented saturation. Signals are larger for stations closer to the shower core due to higher particle density [10].

the signals. The line shows the projection of the arrival direction of the shower. Larger signals in the stations can be observed closer to the impact point of the shower core on the ground, as expected because the particle density at this region is higher.

The signals in the triggered stations are shown in Fig. 4.1b as a function of the perpendicular distance to the shower axis. Again higher signals for stations closer to the shower core are observed. The two stations closest to the shower core presented saturation in their signals, one of which was recovered by a software.

The saturation of a signal may stem from two sources: overflow of the digitising electronics or loss of linearity in the response of the photomultiplier. As described in Sec. 3.2.1, the signals produced in the photomultiplier tubes are digitised by a 10-bits flash analog-to-digital converter (ADC) at a sampling rate of 40 MHz. Given the limited number of bits available to digitise a pulse (1024 possible values), if the pulse height is larger than a limit, the ADC will achieve the end of its scale not being able to digitise the entire pulse. This effect is clearly visible in the signal trace (the count of ADC channels as a function of time) presented in Fig. 4.2a. There, the signal rapidly spikes up reaching the ADC digitisation limit. The result is a cut on top of the signal thus missing a part of

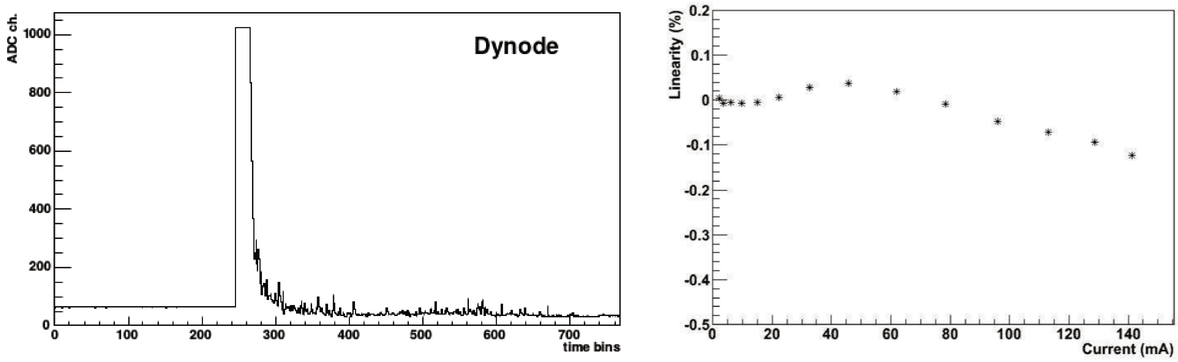

(a) (b)

Figure 4.2: (a) Saturated signal trace caused by overflow in the digitising analog-to-digital converter, the top part of the signal is cut off. (b) Deviation of linearity for different electric currents in the anode of a Photonis XP1805. Inputs causing an anode current higher than 100 mA have a response more than 6% off the linear behaviour.

it.

The other kind of saturation happens when the response of the photomultiplier to an input ranges outside its linear regime. If twice as much photons enter its photocathode, twice as large anode signals will be produced when it operates in its linear region. Unfortunately, there is a limit to this behaviour: for large enough inputs the PMT response reaches a plateau and its linearity is lost. The deviation from linearity for different electric currents measured in the anode of a Photonis XP1805, used in the water-Cherenkov detectors of the Pierre Auger Observatory, is seen in Fig. 4.2b. For an anode current of approximately 105 mA, the deviation from linearity is of about 6%. Higher anode current can therefore be considered outside the linear-response regime.

As explained in Sec. 3.3, the quantity $S(1000)$, the signal at 1000 m from the shower axis, is used to represent the size of an extensive air shower. The value of $S(1000)$ is obtained from a fit of the signals registered by stations triggered in the event to a lateral distribution function (LDF), describing the particle density as a function of the perpendicular distance to the shower axis (see Fig. 4.1b). The distance 1000 m, called the optimum distance, is chosen because it minimises the dependence on the particular LDF chosen for the fit. Several LDF fits for an event are presented in Fig. 4.3a. The signal at about 1000 m is clearly very weakly dependent on the choice of LDF.

When an event presents saturated stations, the optimum distance is no longer

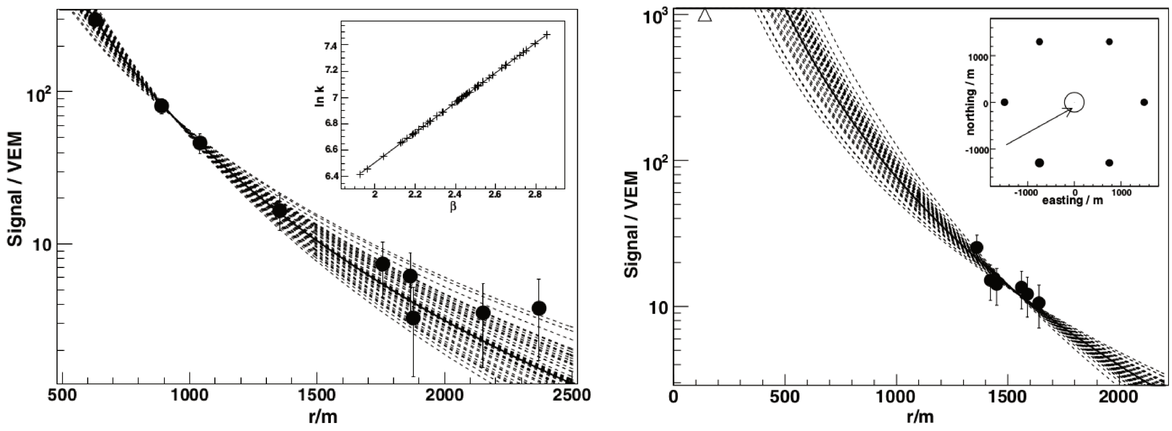

(a) (b)

Figure 4.3: (a) Fit of signals of triggered station to several lateral distribution functions. The distance which minimises the dependence on the choice of LDF is about 1000 m from the shower core. (b) Several LDF fits to signals in an event presenting one saturated station. The optimum distance becomes about 1500 m. In this case, the estimated signal at 1000 m has larger uncertainty due to the choice of LDF for the fit [17].

1000 m from the shower core. In Fig. 4.3b, several LDF fits were performed for an event with one saturated station (the one closest to shower core, as shown in the graph at the upper right). In this case, the distance which minimises the dependence on the choice of LDF is about 1500 m from the shower core. Therefore, in events with saturated stations, the estimated signal at 1000 m obtained from the LDF fit presents a much larger uncertainty.

In the standard procedure to reconstruct an event (see Sec. 3.3), saturated stations are included in the fit of the signals to an LDF (see Fig. 4.1b). This certainly affects an accurate determination of $S(1000)$ and consequently the estimation of properties of the primary cosmic ray, such as its energy. Besides, saturation is a big obstacle to a precise knowledge of the lateral distribution of particles in an extensive air shower, mainly close to its core. In the context of the Observatory upgrade, saturation might impact on the determination of the muonic and electromagnetic components and therefore on the primary mass estimation. Altogether, saturation affects measurements which are key to study models of origin, propagation and acceleration of ultra-high energy cosmic rays as well as to verify the theoretical descriptions of extensive air showers they produce.

Currently, an offline procedure using a software is employed to recover saturated signals. It works well for energies up to 10^{19} eV, above that its accuracy becomes increasingly worse, being smaller than 70% for signals higher than 10 kVEM [1].

One could think of several solutions to the saturation problem. In doing so, avoiding changes to the structure of the detectors is highly desirable as it proved to be robust and provided remarkable data so far. Along these lines, the most natural option would be to lower the gain of the photomultiplier tubes, thus obtaining smaller signals for high particle densities. The problem is that the photomultiplier tubes already operate at a low gain of 2×10^5, therefore lowering it even more would produce a small dynamic-range extension of about a factor two. An additional problem is that the calibration procedure would also change, breaking the data into two sets which could turn the analysis more laborious and complicated.

Another possible solution is to attenuate the anode signal to overcome the ADC saturation. Unfortunately, this option also offers a limited extension of dynamic range. Since most of the photomultiplier tubes in the field were measured to be linear up to anode currents of 80 mA, and that the ADCs have a range of 40 mA, the attenuation of the anode signals could also yield a maximum dynamic-range extension of a factor two, i.e., too small to solve the saturation issue. Besides, the inter-calibration between the dynode and anode signals using physical events would become longer and harder in this case.

In the light of the discussion above, the best-suited solution for the saturation problem is the installation of an extra photo-sensitive device to the stations so that it will provide linear responses in the range of events with high particle density. In principle, any kind of photodetector could be used. However, a photomultiplier tube with small photocathode area was chosen, as this is a well-established and robust technology. The use of newer technologies such as photodiodes, MPPCs or SiPMs were discarded because their implementation would require a longer period of laboratory and field tests (R&D) than desirable for the Observatory upgrade.

Each water-Cherenkov detector (WCD) of the surface array will be equipped with the new PMT, beside the standard PMTs already present. In a given event at which several charged particles cross a WCD and produce many Cherenkov photons, a PMT with smaller area will collect fewer photons yielding a smaller signal compared to the standard PMTs.

For sake of nomenclature, the photomultiplier tubes with small photocathode area will be referred to as small PMTs or sPMTs, the standard photomultiplier tubes will be called large PMTs or LPMTs.

Supposing a photomultiplier tube with quantum efficiency η, area A and gain G, the output charge produced when it is exposed to an area density of photons σ_γ is

$$Q = \sigma_\gamma \eta A G \; . \tag{4.1}$$

The photons are diffusely reflected on the inner surface of the liner of a station, resulting in a quite uniform distribution in the water volume. This translates into a constant σ_γ. Supposing two photomultiplier tubes with similar quantum efficiency, the ratio of their output charges is

$$\frac{Q_1}{Q_2} = \frac{A_1 G_1}{A_2 G_2} \; . \tag{4.2}$$

The collecting area of the large PMTs is 363 cm^2. Assuming a small PMT with 4.9 cm^2 of active area, and setting the gains in these PMTs so that $G_{sPMT} = 2G_{LPMTs}$, results in a charge ratio of $R \equiv Q_{LPMT}/Q_{sPMT} \approx 37$. Therefore, a simple scaling of the collecting area with a sPMT offers an extension of dynamic range of about 37 times (5 bits). The assumption on the PMTs gain ($G_{sPMT} = 2G_{LPMTs}$) is to provide an overlap region in their responses, thus allowing one to calibrate the sPMT using the LPMTs, as will be discussed further.

4.2 Expected performance with small PMT implementation

Researchers of the University of Lecce, in Italy, performed a study based on simulations to validate the proposal of using a small PMT and understand its performance in a more quantitative manner [1, 23]. The results obtained in this study will be presented in this section.

The surface detectors were simulated using the Geant4 toolkit [24] within Offline [25], the software developed by the Pierre Auger Collaboration for relevant analysis, such as event reconstruction from real data and simulation of the Observatory detectors. In the simulations, each water-Cherenkov detector presented a small PMT placed 60 cm

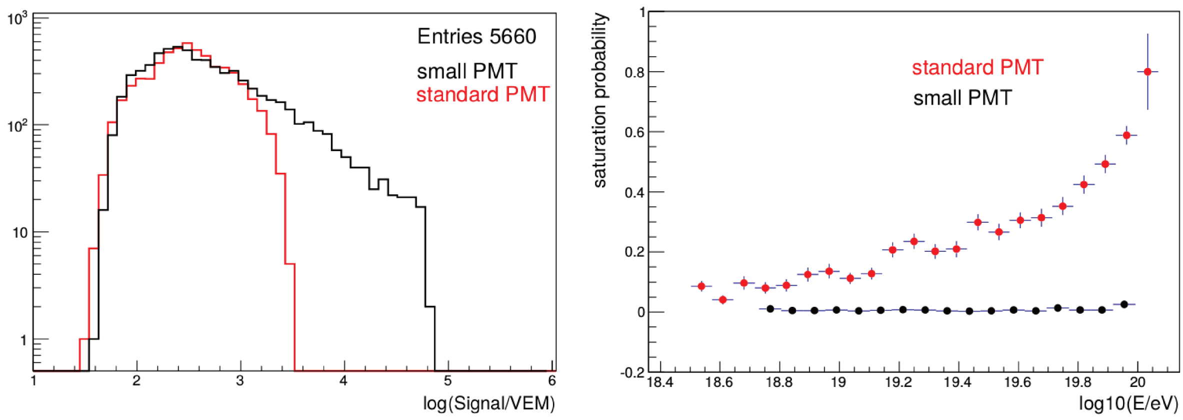

(a) (b)

Figure 4.4: (a) Signal spectrum of the stations. Red represents the signals recorded with the standard PMT, which ranges up to about 1 kVEM. The small PMT (black line) offers a great increase in the dynamic range with registered signals of more than 40 kVEM. (b) Saturation probability as a function of primary energy for large (red) and small (black) PMTs. The implementation of the small PMT almost completely removes saturation occurrences [23].

off the station centre as well as the three standard PMTs. Extensive air showers were simulated using the CORSIKA codes.

As discussed in the previous section, a scale of the PMT collecting area together with setting the proper gain can produce a proportional extension of the dynamic range. The result on the histogram of Fig. 4.4a, showing the signal spectrum of the stations, confirms this prediction. The WCDs with the standard PMTs are able to record signals up to about 1 kVEM, whereas with the implementation of the small PMT the dynamic range should increase to more than 40 kVEM.

Figure 4.4b shows the saturation probability as a function of the primary energy. The saturation probability for the large PMTs increases with energy, as expected since more particles are produced in more energetic showers. With the implementation of the small PMT, providing the increase of dynamic range, the saturation occurrence is almost completely removed even for the highest energy events.

In Fig. 4.5, the simulated signals of the stations are plotted as a function of their distance to the shower axis for different energies, represented by the coloured markers for the large PMT signals. Black markers represent the small PMT signals. For smaller

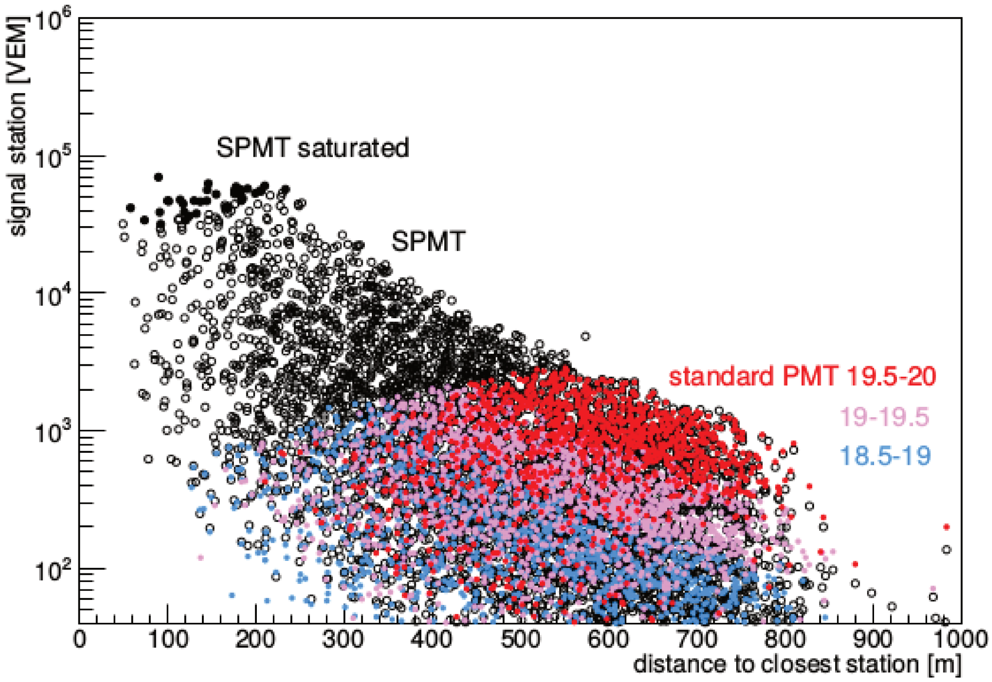

Figure 4.5: Simulated signals as a function of the distance to the shower axis for different primary energies. Coloured markers represent LPMTs and black ones the sPMT signals. Using the small PMT it will be possible to measure unsaturated signals as close as 250 m from the shower core [1].

energies, the LPMTs present unsaturated signals closer to the shower core. However, with increasing energy, and thus higher particle densities, the LPMTs can provide clean signals only farther from the shower core. On the other hand, the use of small PMTs allows one to have unsaturated signals as close as 250 m from the shower core, even for the highest primary energies. This offers an opportunity to study the details of the lateral distribution of particles at distances never explored before.

The simulation study also showed an improvement on the resolution of $S(1000)$ with the implementation of the small PMT. In Fig. 4.6, the $S(1000)$ resolution ($\sigma_{S(1000)}$) is plotted for different energies. Red points represent saturated events, whereas unsaturated ones, in black, are due to the use of the sPMT. An improvement from 10% to 5% for lower energies and from 7% to 3% for higher energies was obtained. The plot also shows in opened black circles the performance of the recovery software. It works well up to about 10^{19} eV and for higher energies it becomes less effective, therefore reinforcing the need for dynamic-range extension. The improvement on $\sigma_{S(1000)}$ was expected, since saturation affects an accurate determination of $S(1000)$ obtained from the LDF fit, as discussed in

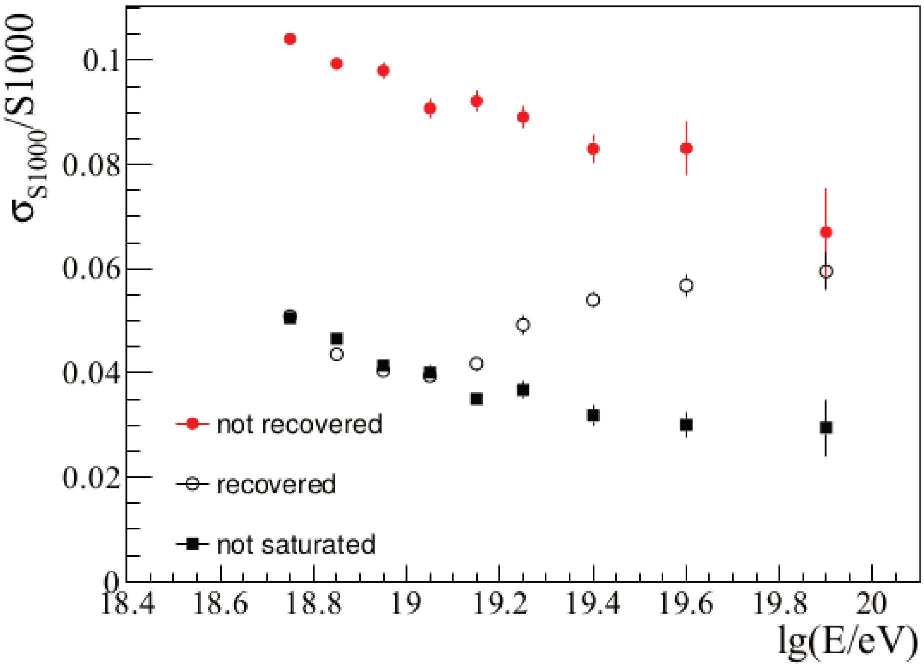

Figure 4.6: Resolution of $S(1000)$ for different energies. Red points represent saturated events, black squares unsaturated events and open circles the performance of the recovery software. The implementation of small PMTs improves the $S(1000)$ resolution [1].

the previous section.

Another interesting result obtained from the simulations is that saturation does not affect the determination of the expectation value of reconstructed observables such as $S(1000)$, energy and arrival direction, but it impacts on their resolution. With the improvement on the resolution of $S(1000)$, as seen in Fig. 4.6, a better resolution on shower properties derived from the estimation of $S(1000)$ is also expected. This is exactly what is observed in Fig. 4.7, for the resolution on depth of shower maximum X_{max} and relative number of muons R_μ, obtained from shower reconstruction using the universality principle [26]. The plots on the left show the reconstruction resolution with unsaturated events, whereas events with saturation are shown on the right. Improvements are seen in the X_{max} and R_μ resolutions for all the energy ranges shown, both for proton and iron primaries. In the case of R_μ, a great improvement is verified, for instance, at energy of 10^{19} eV, the resolution goes from about 20% when saturation is present to roughly 5% without saturation.

The energy determination for events detected only with the surface stations relies on their calibration using hybrid events seen by both surface and fluorescence de-

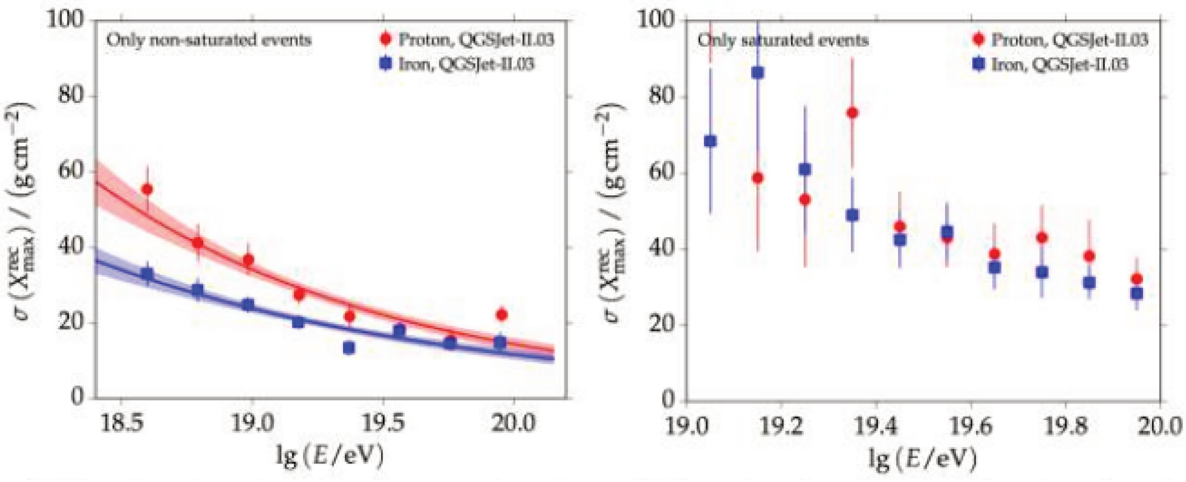

(a)

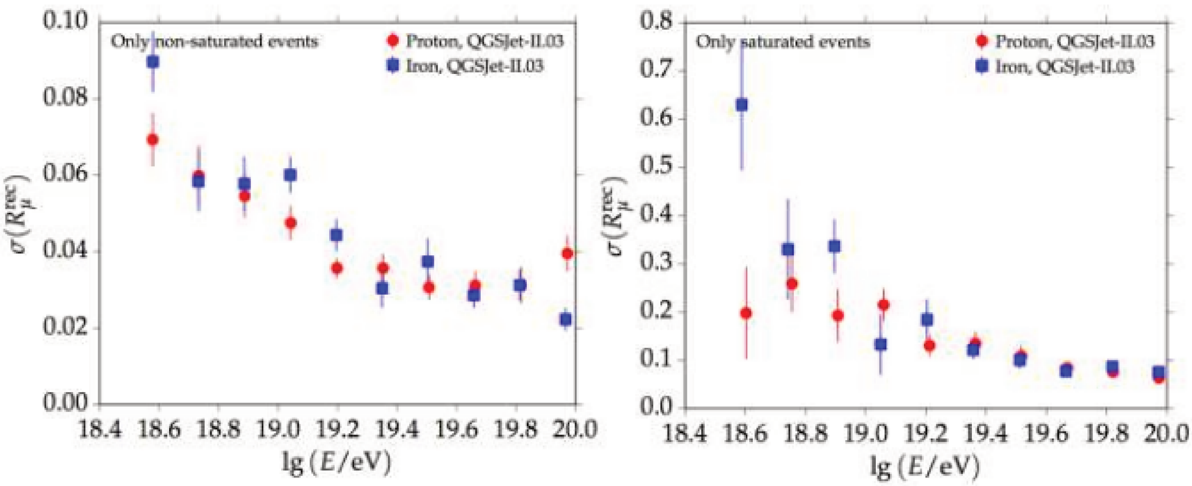

(b)

Figure 4.7: Resolution of reconstructed depth of shower maximum (a) and relative number of muons (b) as a function of energy, for both proton and iron primaries. The plots on the left show unsaturated events whereas the ones on the right are done using saturated events. In both cases (a) and (b), an improvement is observed when non-saturated events are present [23].

tectors (see Sec. 3.3). The uncertainty on this calibration depends on the resolution of the detectors. In the case of the surface stations, a better resolution on the determination of $S(1000)$, achieved with the implementation of the small PMT, translates into an improved calibration and therefore estimation of the primary energy with better resolution.

Since the impact point of the shower axis on the ground is obtained from the fit of the station signals to an LDF, the accuracy in its determination shall also benefit

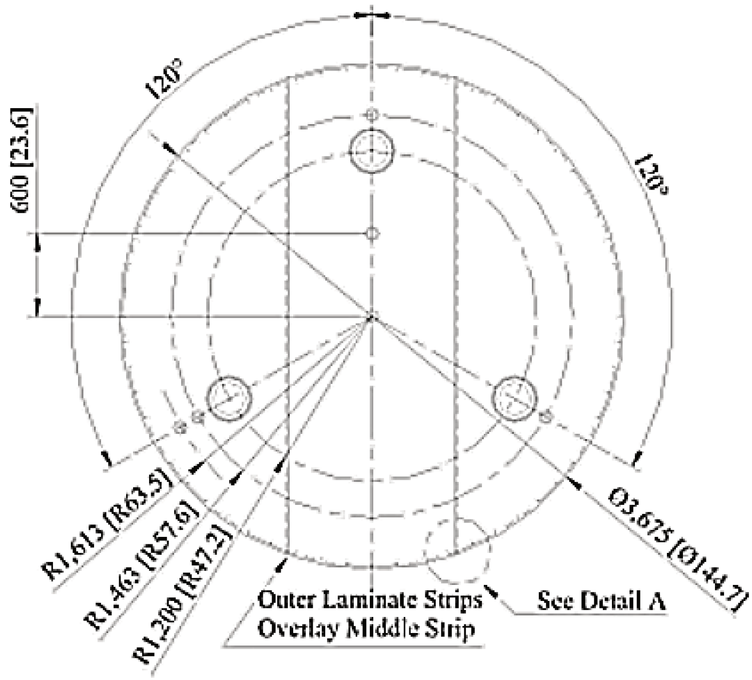

Figure 4.8: Schematic view of the liner top. The three standard photomultiplier windows are shown. Additional windows for hosting LED flashers are present and offer a good option of place for the installation of the small PMT.

from the implementation of the small PMT, especially near the shower core.

The simulation results presented in this section reinforce the proposal of using small PMTs and the physics potential which can be achieved with its installation in the water-Cherenkov detectors of the surface array.

4.3 Implementation of small PMT in the surface detector

Given that the use of small PMTs in the water-Cherenkov detectors is a solution to the saturation problem and extension of the dynamic range of the surface stations, the details of its physical implementation in the stations will be discussed in this section.

One of the main concerns is to minimize the impact on data taking during the upgrade phase. Therefore, the current physical characteristics of the WCDs must be conserved as much as possible. The station liners have extra windows with 30 mm of diameter, as shown in the schematics of Fig. 4.8 (also see Sec. 3.2.1). They were designed

Figure 4.9: Picture of Hamamatsu photomultiplier tubes R8619 (top) and R6094 (bottom), candidates for the small PMT proposal.

to host additional LED flashers, but currently are not being used thus it is the ideal place to install the small PMT.

The liner offers two options of window to install the small PMT: the central window or the one at 60 cm off centre. The one in the liner centre is ideal, as the sPMT will be placed in a symmetrical position, however access to it is difficult through the standard PMT hatches forcing an additional hole on the tank structure to be drilled. As modifying the tank structure is not desirable, it was chosen to install the sPMT on the off-centre window, which can be easily accessed by the closest LPMT hatch. The off-centre position should not be a problem as the sPMT signal will be used for events that produce a high photon density inside the liner which spreads uniformly in the water volume.

Since the upgrade also includes new electronics, specifically flash analog-to-digital converters with sampling rate of 120 MHz, the small PMT model chosen must have anode rise time smaller than 6 ns. In addition, the sPMT response is required to present a maximum deviation from linearity of 5% for anode currents up to 50 mA to avoid its saturation.

A search on the market for photomultiplier tubes meeting the requirements discussed resulted in three candidates. The models R8619 and R6094 produced by Hamamatsu and 9107FLB by ET Enterprise. Some characteristics of these models are shown in Tab. 4.1. Among the options, R8619 has been chosen as the best candidate due to production uniformity and the possibility of being produced with flying leads. The other two models can be regarded as backup options. A picture of Hamamatsu models R8619 and R6094 can be seen in Fig. 4.9.

The voltage divider used for the small PMT candidates has several resistors in series. The voltage on the last stages becomes increasingly larger, as shown in Fig. 4.10a for model R8619. This allows one to achieve high-current peaks and good linearity. A picture of the divider circuit-board made for model R8619 is shown in Fig. 4.10b, which is attached to the PMT base (see Fig. 4.9).

The high voltage powering the small PMTs will be provided by a dedicated module produced by CAEN. Given the small dimensions of the base divider and aiming at easy maintenance, the high-voltage module will be inside an isolated box (see Fig. 4.10c) placed close to the upgraded unified board.

As the liner LED window was not designed to host an additional PMT, some adjustments are necessary to guarantee its steady placement. A PVC flange will be placed around the window to increase the pressure on the water and flatten the liner. The PMT is put inside a PVC tube which works as a holder and provides access for cables.

An additional flash analog-to-digital converter, similar to the one for the large PMTs with 12 bits and 120 MHz, will be used to read the small PMT signals. The signals will then have to be converted to VEM unit. Due to the small collecting area of the small PMT, it is not capable of registering the signal produced by single vertical muons. Therefore, a VEM calibration process similar to the one performed for the large PMTs is not possible (see Sec. 3.2.2). Fortunately, it is possible to calibrate the sPMT

Table 4.1: Characteristics of the small PMT candidate models which meet the physical and performance requirements. Gain and non-linearity anode current were measured in the INFN Torino laboratory.

Model	Glass diameter (mm)	I_{max} non-linearity $< 5\%$ (mA)	Quantum efficiency (@ $\sim$ 400 nm)	Gain @ 1.5 kV
R8619	25	58	28%	1.2×10^7
R6094	28	62	27%	1.7×10^7
9107FLB	29	65	28%	1.6×10^7

Elettrodi	K	Dy1	Dy2	Dy3	Dy4	Dy5	Dy6	Dy7	Dy8	Dy9	Dy10	P
TAPER A	3	1	1,5	1	1	1	1,2	1,5	2,2	3,6	3	
TAPER B	4	1	1,5	1	0,5	1	1,2	1,5	2,2	3,6	3	

K= catodo
Dy= dinodo
P= anodo

TAPER A = P1 chiuso P2 aperto
TAPER B = P1 aperto P2 chiuso

(a)

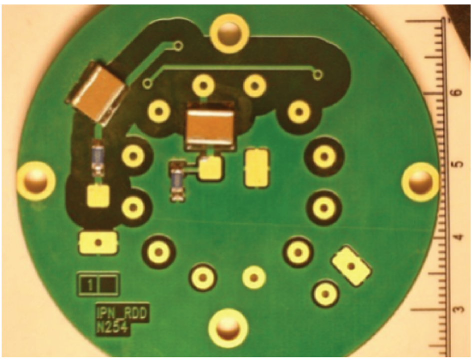

(b) (c)

Figure 4.10: (a) Schematic drawing showing the ratio of voltages applied in the different stages of Hamamatsu PMT model R8619. (b) Divider circuit-board for same PMT model which is attached to its base. (c) High-voltage power supply box produced by CAEN.

using the LPMTs. By setting the sPMT gain so that there is an overlap region of linear signal responses for both small and large PMTs, one can use small shower events seen by both PMTs and the LPMT VEM calibration to obtain the small PMT signals also in VEM units. More on the VEM calibration of the sPMTs will be discussed in the next chapter.

4.4 Engineering array test setup

During a campaign on the 20th and 21st of April 2016, ten water-Cherenkov detectors of the surface array had a small PMT installed on them to assess its performance in real surface detector stations as well as study their calibration and the dynamic-range extension they provide.

These ten stations are referred to as the Engineering Array (EA). Their geometric disposition as well as identification are shown in Fig 4.11. The three small PMT

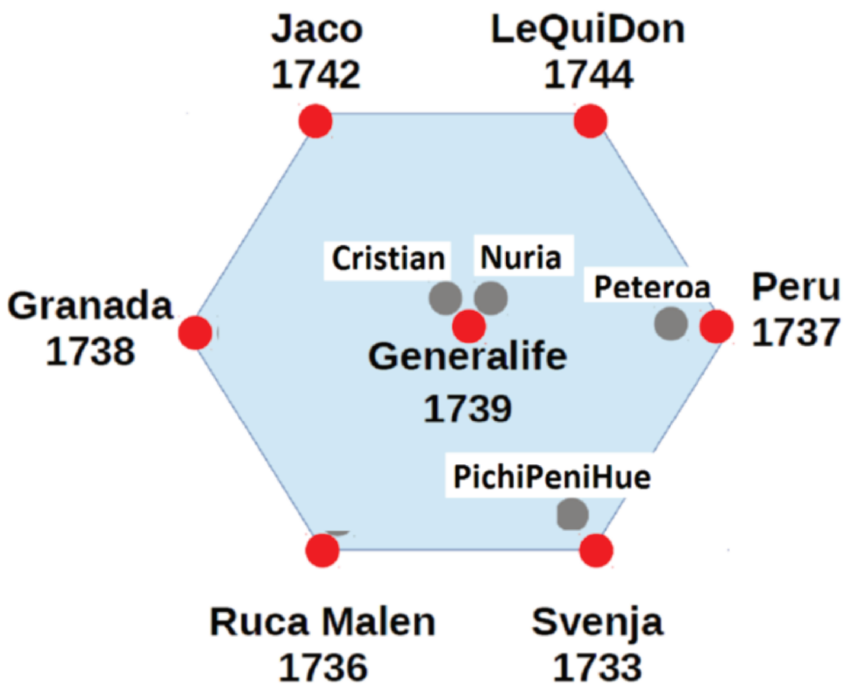

Figure 4.11: Geometrical disposition of the water-Cherenkov detectors forming the Engineering Array. Each station received a small PMT model.

candidate models, R8619, R6094 and 9107FLB were put to test, although, as explained before, R8619 is the preferred one. Six stations received the R8619 model, two the R6094 and two the 9107FLB.

The high voltage is supplied by the CAEN module and the base dividers are the ones shown in Fig. 4.10b for the R8619 model. Equivalent ones for the other sPMT models were used. LED flashers were installed in the liner central window for stations lacking it.

The steps for the installation of the small PMT in a station are illustrated in Fig. 4.12. The liner window at 60 cm off centre, which will receive the sPMT, is shown in panel A. The PVC flange is placed around the window to flatten the liner surface and provide more stability (panel B). Then a stainless steel hose clamp is placed around the window to later fix the sPMT (panel C). Using a syringe, 3 cm^3 of optical silicon, the same used for the LPMTs, is inserted to improve the coupling of the sPMT to the window (panel D). The small PMT, inside the PVC mechanical holder, is placed on the window and the hose clamp is closed to fix it (panel E). Lastly, the cables are fixed to the PVC flange to avoid unintentional accidents (panel F). The whole process takes less than thirty minutes.

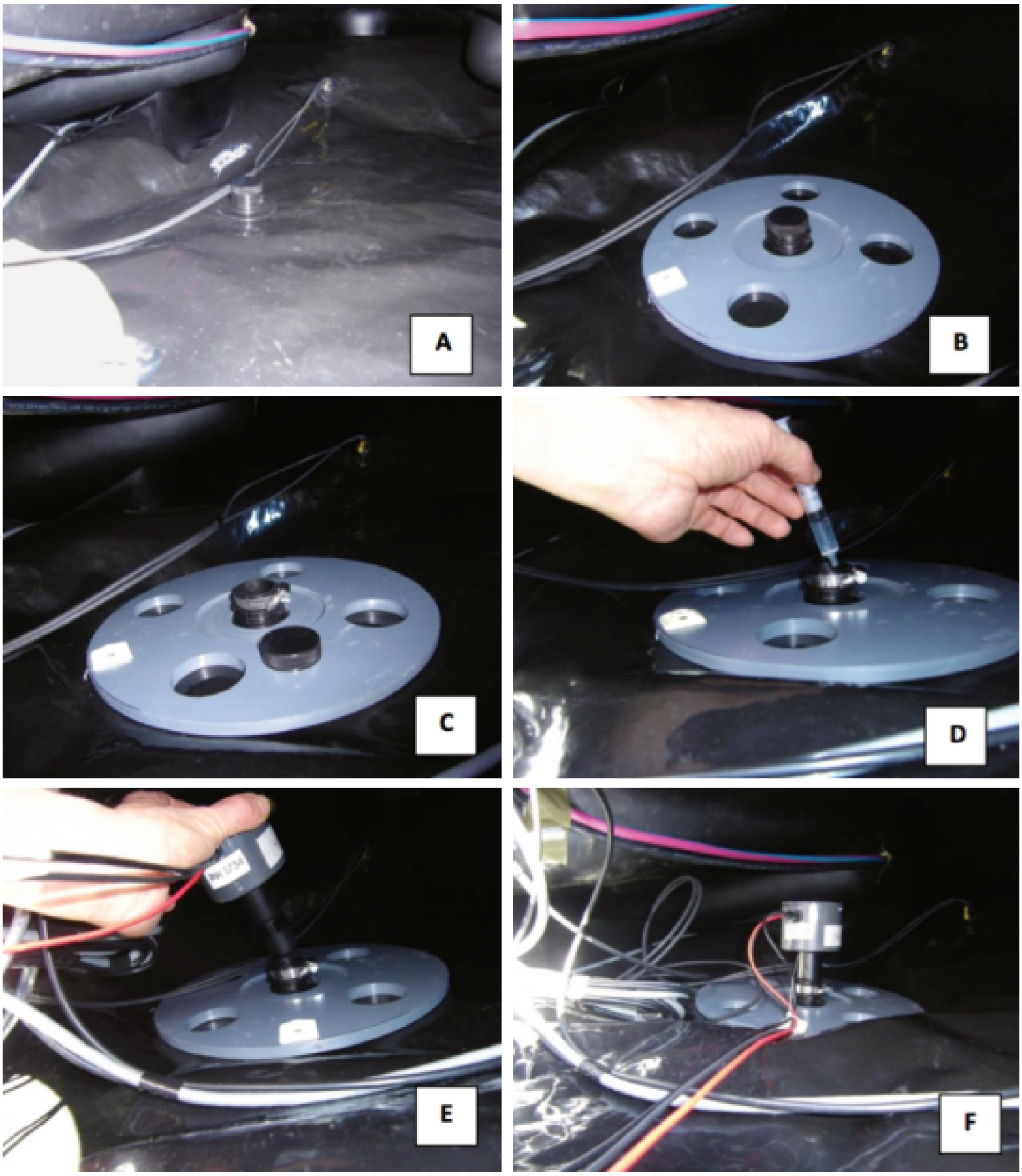

Figure 4.12: Installation procedure of the small PMT (see text for description). The whole process takes less than 30 minutes.

Since no upgraded unified board was available at the time, a dedicated ADC channel for collection of the sPMT signal could not be used. To solve this issue, the ADC for digitisation of the anode signal of one of the large PMTs (LPMT 1) was used for the small PMT. Therefore, the EA stations had one small and two standard PMTs operational.

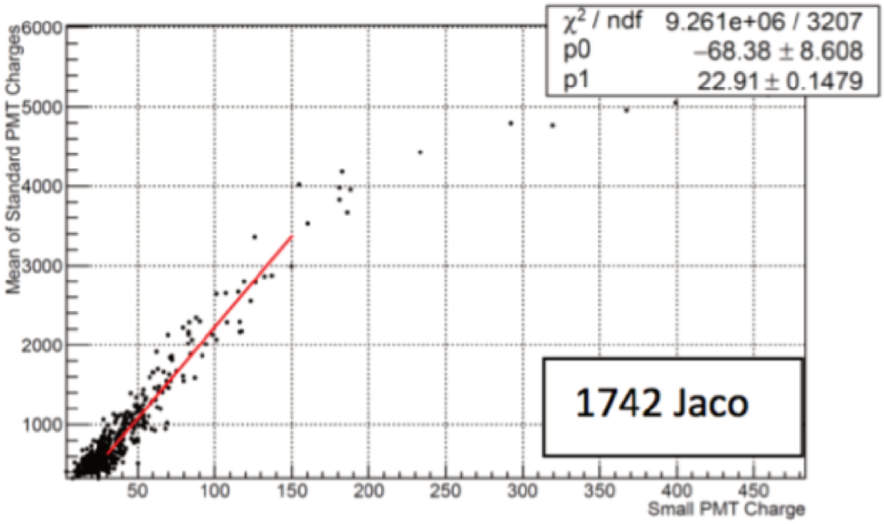

(a)

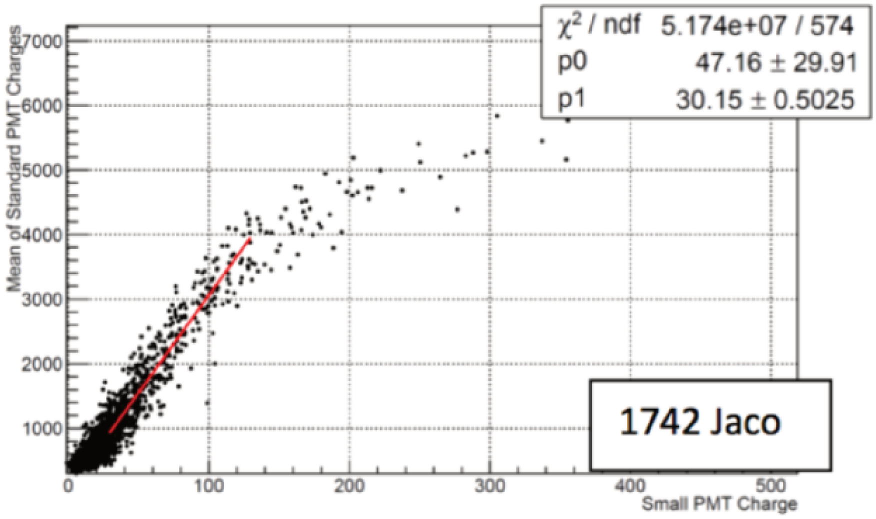

(b)

Figure 4.13: Average large PMT charge versus small PMT charge for station 1742, using real shower events. (a) After procedure to set sPMT high voltage with the LED flasher. (b) After manual adjustment of the sPMT high voltage to obtain $R \sim 32$ with real shower events. A significant difference is observed in coefficient p_1 representing the ratio between the large and small PMTs.

After a successful installation of the small PMTs, their gains were adjusted, using light pulses produced by the LED flashers, so that the ratio R between the average signal charge of the two LPMTs and the sPMT be close to 32. A program called "GoSmall" will be installed to automatise this procedure. It will produce light pulses with increasing intensity, then R is calculated, and if it is not close to 32 the sPMT high voltage is modified and the process is repeated until R converges to about 32.

With the sPMT gain set by the LED flasher method, real shower data started to be acquired. A threshold trigger requiring that the signal pulse-height in both LPMTs be larger than 120 ADC channels was set. The data collected for each event includes

- event time, using UNIX timestamp,
- signal charge in the small and large PMTs, in integrated ADC channels (ADC $\times$ bins),
- signal peaks of small and large PMTs, in ADC channels.

At every 500 events a file was sent to CDAS containing these events. The typical file size is about 8 kB.

Due to geometrical effects, the LED light diffuses differently in the water volume compared to Cherenkov photons produced in shower events. Therefore, for these a different ratio R may be presented. This is precisely what was observed for some stations. For example, station 1742 had R set to 30 using the LED flasher procedure. After some shower data was collected, the value $R = 22.9$ was obtained, as shown in Fig. 4.13a where the average signal charge of the LPMTs (y-axis) is plotted against sPMT charge (x-axis). A linear fit was applied and p_1 represents R.

The high voltage on the small PMT was modified remotely from CDAS so that the obtained R from shower events be close to 32. The same plot as in Fig. 4.13a is presented in Fig. 4.13b after the gain adjustment. The value $R = 30$ was obtained. The development of a software to automatically perform this adjustment in “real time” is under way.

In the next chapter, the results of our analysis using the data collected by the engineering array during more than five months will be presented.

Chapter 5

Engineering array data analysis

In this chapter, we present the results obtained in our analysis of the data collected by the engineering array between the 21st of April and the 17th of October of 2016. First, we synchronized two relevant sets of data, then the validity of the data collected by the small PMTs was verified. We studied two calibration methods as well as their performances. Finally, we observed the extension of the dynamic range of the engineering array stations with the use of the small PMTs.

5.1 Data sets used for analysis

The data used for the analysis described in this chapter came from two sources. The first, as described in Section 4.4, contains the event time, integrated charges and signal peaks registered by each PMT of the engineering array (EA) stations. The other set contains monitoring data which gives information about the performance and status of the components of each station. These data is collected every six minutes and a more detailed description will be given in the next section.

We created a program written in C++ to synchronize each event detected with the closest monitoring data available. It also excluded events for which monitoring data at the time was absent. The program delivered as output one file containing all synchronized data for each station. This design made the data analysis much more efficient and easier to carry.

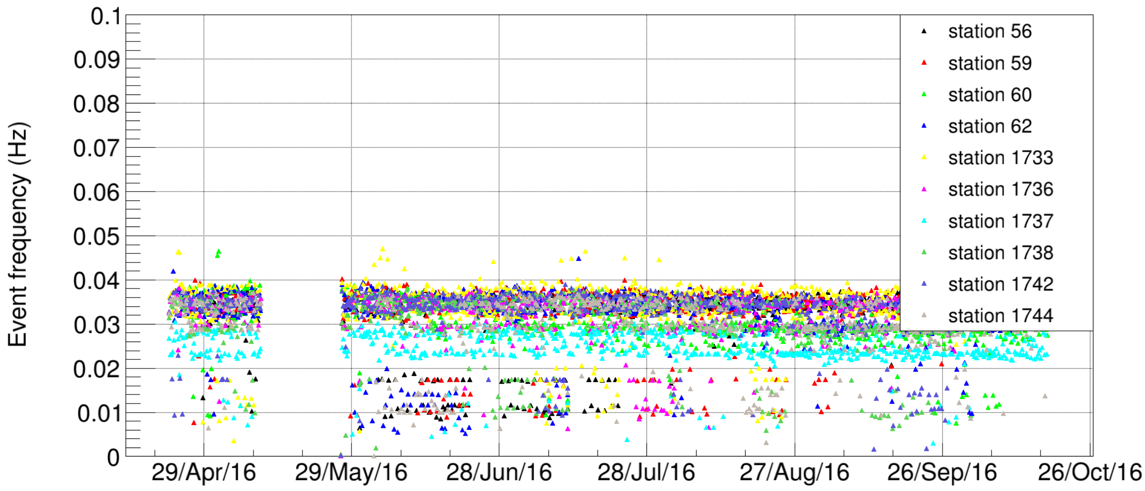

Figure 5.1: Frequency of events calculated every six hours for all engineering-array stations. The frequency is constant in time with some variations due to noise.

5.2 Validation of data collected by the small PMTs

Verifying whether the data collected by the small PMTs is valid, e.i., if it was collected under stable working conditions of the stations, is necessary before using it for deeper analysis. Using data collected when some component of a station was operating improperly is not desirable. We used two approaches to achieve such quality control of the small PMT data. First, the event rate was analysed, then a more thorough study was carried out using monitoring data. Each of these approaches will be described in the following subsections.

5.2.1 Event frequency

The frequency of events detected by a station provides an indirect means to assess its working condition. If a station presents some malfunction, the rate of detected events can be directly affected, and therefore it can be used as a preliminary check of its working condition.

The frequency of events for each station during the whole period of data collection in the engineering array is presented in Fig. 5.1. We calculated the frequency every six hours. No events were registered during the 10^{th} up to the 23^{rd} of May of 2016. That happened because all stations of the surface detector array were powered down during that period, due to cloudy weather conditions which made the batteries reach a low level.

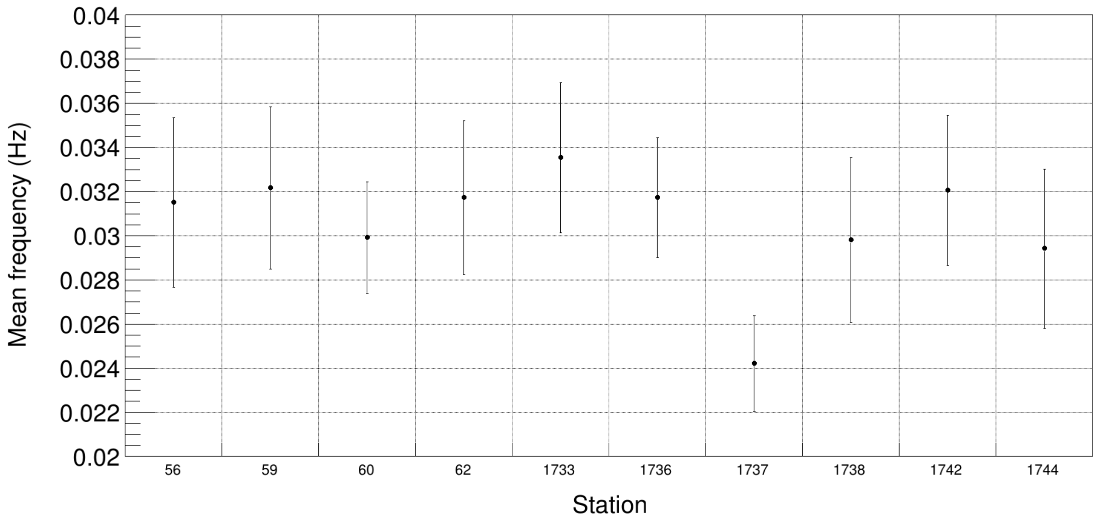

Figure 5.2: Mean frequency of events for each engineering array station during the whole period of data collection. About 100 events are registered every hour, therefore the rate of events is high enough for remote and independent calibration of the small PMTs.

The frequency of events observed in Fig. 5.1 is quite constant during time for all stations, with some variations due to noise. This is a good indicator that the engineering-array stations are operating soundly.

We present in Fig. 5.2 the mean frequency of events registered by each station during the whole period of data collection. For most stations, the mean frequency is about 0.03 Hz. Station 1734 presented a slightly lower frequency of 0.024 Hz. This translates into roughly 100 events every hour. Therefore, besides being a first good indicator that the stations are operating stably, the rate of events is large enough to allow the calibration of the small PMTs to be performed remotely and independently. More on calibration will be treated in Section 5.3.

5.2.2 Monitoring data

We performed a more thorough verification of the working conditions of the engineering-array stations using monitoring data. Monitoring data concerns information about several components which are part of a station, therefore this set of data can provide direct information on the performance of individual stations.

We plotted in Fig. 5.3 the electric current of one of the large PMTs (PMT 3) along the period of data collection for all stations. Most of the time, the electric current

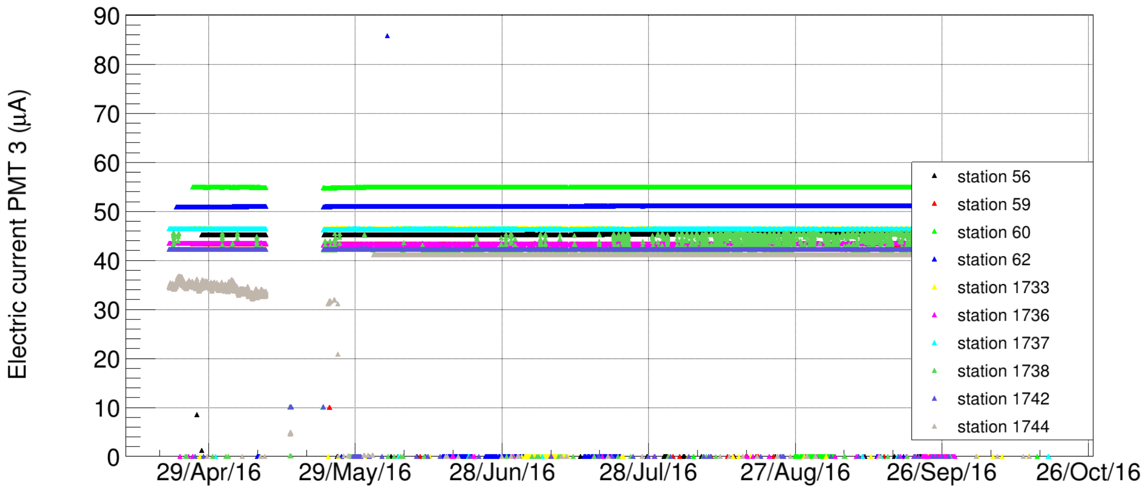

Figure 5.3: Electric current on PMT 3 (a large PMT) as a function of time for all engineering-array stations. Most of the time, it presents a constant value, between 40 and 56 μA, which is assumed to represent the stable behaviour of this parameter. Some periods of instability are observed. Data collected during such periods were excluded from further analysis.

is constant. For these periods we assumed that the current is in its regular regime of

Table 5.1: Range of regular working conditions for monitoring parameters.

Monitoring parameter	Lower limit	Upper limit
3.3 V power supply	3.31 V	3.36 V
-3.3 V power supply	-3.41 V	-3.33 V
5 V power supply	5.08 V	5.17 V
12 V power supply	11.85 V	12.1 V
SPMT current	13.5 μA	17.0 μA
LPMT 2 current	37.0 μA	45.0 μA
LPMT 3 current	40.0 μA	56.0 μA
LPMT 2 temperature	-7.0 $°C$	35.0 $°C$
LPMT 3 temperature	-10.0 $°C$	40.0 $°C$
LPMT 2 VEM calibration	90 ADC ch.	170 ADC ch.
LPMT 3 VEM calibration	100 ADC ch.	162 ADC ch.

operation. In the case of Fig. 5.3, the identified stable working condition for the electric current, concerning all stations, is between 40 and 56 μA. Sometimes the current is outside the limits of stable operation. Using data collected during such periods of time is not desirable because such data might have been registered when the station was not working properly.

Plots such as the one in Fig. 5.3 were done for the following monitoring parameters: temperature of the photomultipliers, their electric current, power supplies and VEM calibration (large PMTs only). The region of stable condition for these parameters was identified and is shown in Tab. 5.1. Only the data collected when the monitoring parameters were within their regular operation conditions were used for further analysis.

5.3 Calibration of the small PMTs

The main goal of the small PMT calibration is to provide a means to convert their signals from hardware unit (integrated ADC channels) into a station-independent physical unit (VEM), which represents the particle density that crossed the detector in an event. Expressing the signals in VEM provides a reference level for all stations and facilitates further analysis of this data and comparison to simulation.

As the signal produced by single muons is too low for the small PMT to detect, the calibration procedure performed for the large PMTs, as described in Sec. 3.2.2, can not be applied to the sPMTs. However, they can be calibrated exploiting the VEM calibration of the large PMTs of the station and the overlap region of their linear responses. In this case, linearity means that the produced signals have a linear dependency on the number of photons entering the cathode, i.e., a signal twice as big is observed when twice as much photons enter the PMT.

Due to the different cathode collecting area of the small and large PMTs, the latter will present higher signal than the first for the same particle density crossing the water volume of the detector. Events with low particle density can not be detected by the sPMT. On the other hand, high particle-density events cause saturated signals in the LPMTs, mainly because of overflow in the digitizing electronics. However, there are events which will generate non-saturated signals in both small and large PMTs. These overlapping events are the ones interesting to use in the sPMT calibration, because the

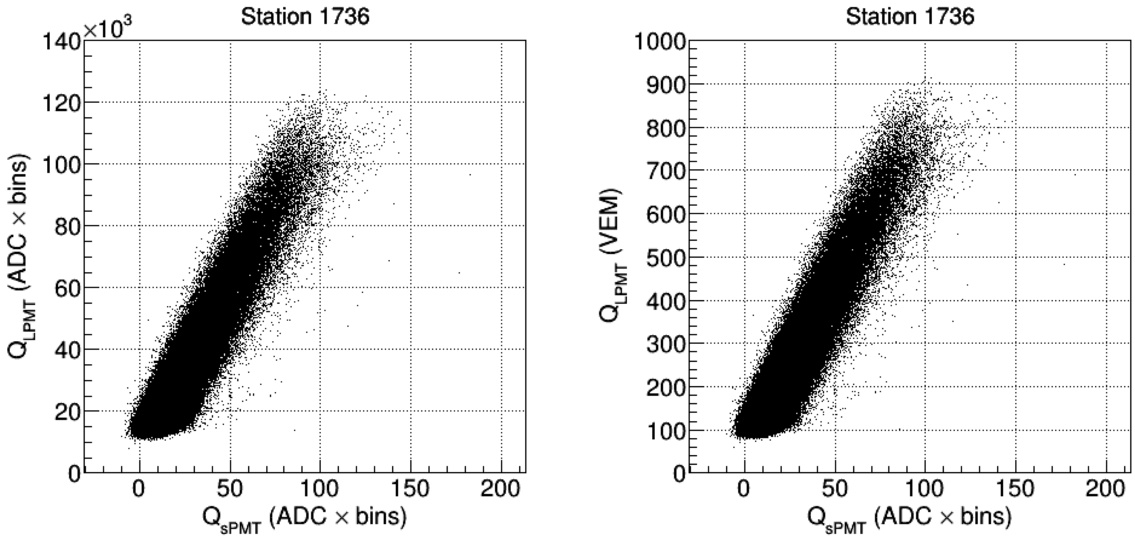

Figure 5.4: Left: average charge on the large PMTs as a function of the charge on the small PMT of the engineering-array station 1736, both in hardware units. The charges in the sPMT are much smaller than the ones in the LPMTs. Right: same plot as the one in the left, but with the charges on the LPMTs in VEM units. The sPMT charge, in hardware unit, can be related to the VEM charge obtained by the LPMTs. Both plots have only non-saturated events.

signal in VEM unit is known from the large PMTs, and, as both PMTs are in the linear response regime, a relation of the form

$$Q_{LPMT}\ (\mathrm{VEM}) = p_0 Q_{sPMT}\ (\mathrm{ADC\ ch.}) + p_1 \tag{5.1}$$

can be established, where Q is the charge (signal) in a given PMT. The term p_1 is necessary to compensate for the low signals in the large PMTs which the small PMT can not detect. Equation 5.1 says that, for an event, the signal of the small PMT in hardware unit corresponds to a signal in VEM unit obtained from the large PMT calibration.

Figure 5.4 underlines the ideas above. On the left, we plotted the average charge on the large PMTs of a station as a function of the charge on the small PMT, both in hardware units. In both plots, only non-saturated events are shown. For the same event, the charge on the LPMT is much larger than on the sPMT, because the first has a larger cathode area than the latter. Therefore, the extension of dynamic range can already be observed.

On the right of Fig. 5.4, we plotted the average charge on the LPMTs, now in VEM unit, as a function of the charge in the sPMT, in integrated ADC channels. For each

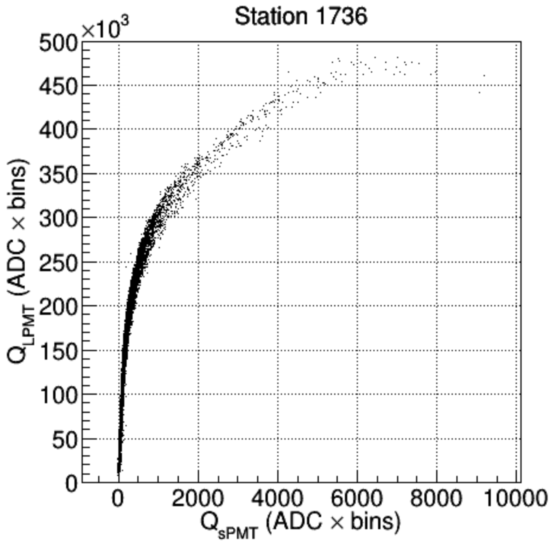

(a)

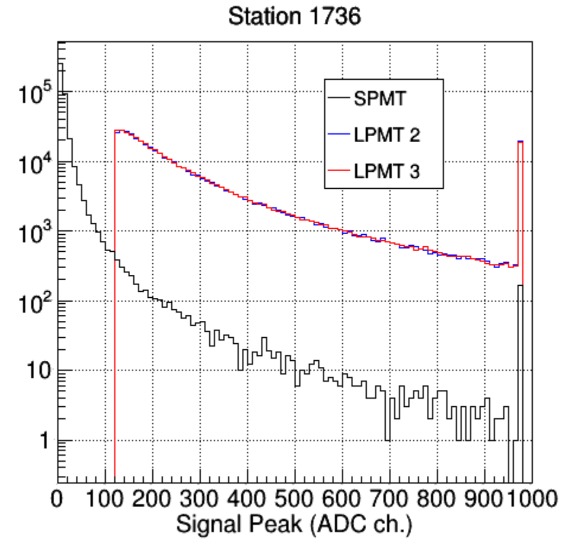

(b)

Figure 5.5: (a) Average charge of the LPMTs as a function of the charge of the sPMT. Saturated events are also shown. The charges of the small and large PMTs have a linear relationship until the LPMT signals start to saturate. (b) Histogram of the signal peak of the PMTs of station 1736. The peak at the right end of the distribution corresponds to saturated events that caused overflow of the analog-to-digital converter.

of these events, the sPMT signal, in hardware unit, can be related to the corresponding signal detected in the LPMTs in VEM unit, therefore it provides a means to calibrate the sPMT.

In Fig. 5.5a, we plotted the average charge of the LPMTs as a function of the charge of the sPMT, only this time saturated and non-saturated events are present. The charges of the small and large PMTs follow a linear relationship until the latter starts to present saturation, causing their linearity to be lost. Since using only unsaturated events is critical to perform the calibration of the sPMT, identifying saturated events is extremely important, so that they are excluded from the procedure to calibrate the small PMTs.

As explained in Section 4.1, saturation arises when a signal is too large to be digitised by the station electronics. We plotted in Fig. 5.5b a histogram of the signal peak for each PMT of station 1736. A peak in the histogram can be seen at the end of the distribution. It represents events for which the signal peak was larger than the analog-to-digital converter (ADC) could digitise, i.e., hitting the ADC “end of

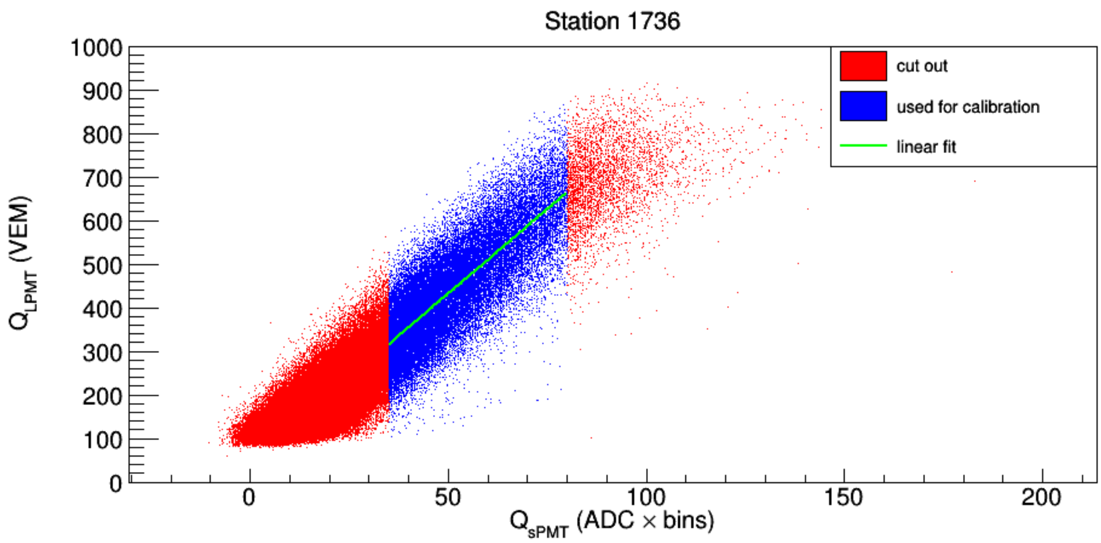

Figure 5.6: Linear fit performed to obtain relation between Q_{LPMT}, in VEM, and Q_{sPMT}, in integrated ADC channels. There are biases for low and high-charge regions. The low-charge bias is caused by the threshold trigger for data acquisition, whereas the high-charge bias is due to saturation of the LPMTs. Cuts on Q_{SPMT} were set to remove biases. The red points are events excluded by the cuts. Blue points represent events used in the linear fit represented by the green line.

scale". Therefore, events with signal peak larger than this value are saturated events. We analysed histograms like the one in Fig. 5.5b for all stations and saturation was defined to occur for events with signal peak above 960 ADC channels.

5.3.1 Calibration methods

We studied two methods to perform the calibration of the small PMTs, i.e., find a way to convert their signals from hardware units to VEM. We now describe these methods and compare their accuracy.

Linear fit with vertical cuts

In this approach, the basic procedure is to calibrate the sPMT by performing a linear fit with the form of Eq. 5.1 in the plot of the average charge on the LPMTs, in VEM unit, as a function of the charge on the small PMT, in ADC channels, for each engineering-array station. We show such plot for station 1736 in Fig. 5.6.

In the plot of Fig. 5.6, there are two regions with biases: one at low charges and other for high charges. The low-charge bias is due to the threshold trigger condition for data acquisition (see Section 4.4). It causes a somewhat horizontal cut at the bottom of the plot. The high-charge bias happens because of saturation of the large PMTs.

We set simple cuts on the charge of the sPMT to remove the biases: a lower cut to remove threshold bias and a higher cut to remove saturation bias. The cut values were chosen so that the calibration uncertainty obtained with the linear fit were as close as possible to zero. The calibration uncertainty will be defined and discussed in Section 5.3.2. The cut values are presented in Tab. 5.2 for all stations, in hardware units.

Once the biased events were removed, we applied a linear fit, represented by the green line in Fig. 5.6. The events used for the calibration are shown in blue, whereas the ones excluded by the cuts are in red. The cuts produce vertical lines in the plot.

The calibration parameters p_0 and p_1 of Eq. 5.1 were retrieved from the linear fit. They can be used, in a given event, to convert the small PMT signal into VEM unit with the relation

$$Q \text{ (VEM)} = p_0 Q_{sPMT} \text{ (ADC chs.)} + p_1 \ . \tag{5.2}$$

The linear fit parameters are shown in Tab. 5.3 for all stations along with their corresponding sPMT models.

Table 5.2: Lower and upper cuts on the charge of the sPMT for all stations, in integrated ADC channels.

Station	Lower cut	Upper cut
56	45	100
59	20	55
60	40	80
62	30	65
1733	40	85
1736	35	80
1737	30	60
1738	40	75
1742	35	70
1744	45	80

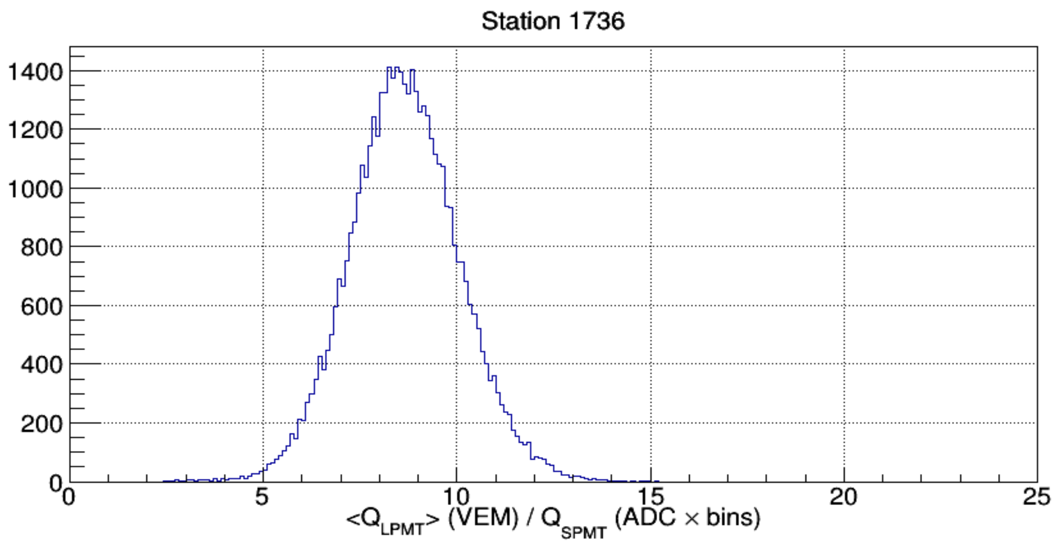

Figure 5.7: Histogram of the ratio between the average charge of the LPMTs (VEM) and the charge on the sPMT (integrated ADC channels). The distribution varies around a mean value, with a shape reminding that of a Gaussian distribution. The mean value of the histogram was used to calibrate the sPMT.

Charge ratio

We studied another approach to calibrate the sPMT by computing the ratio (R) between the signals on the large PMTs, in VEM, and on the small PMT, in ADC channels. This method is valid when the term p_1 in Eq. 5.1 is negligible compared to $p_0 Q_{sPMT}$, so that

$$R = \frac{Q_{LPMTs}\ \text{(VEM)}}{Q_{sPMT}\ \text{(ADC chs.)}} = p_0\ . \tag{5.3}$$

We plotted in Fig. 5.7 a histogram of the charge ratio R, for non-saturated events. Cuts on the charge of the sPMT were also applied to remove the biases discussed above. We used the same values shown in Tab. 5.2 for the linear fit. The histogram has a shape resembling that of a Gaussian distribution, varying around a mean value.

For each engineering-array station, we obtained the mean value of the charge-ratio distribution ($\langle R \rangle$) which can be used to calibrate the small PMT, since the relation

$$Q\ \text{(VEM)}\ = \langle R \rangle \times Q_{sPMT}\ \text{(ADC chs.)} \tag{5.4}$$

can be found from Eq. 5.3. It converts the charge of the sPMT from hardware units to VEM. The values of the mean ratio for all stations are presented in Tab. 5.3. Indeed, the mean ratio is closer to the values of p_0 obtained with the linear-fit method when p_1 is small. This agrees with the assumption of validity of the method leading to Eq. 5.3.

Table 5.3: Linear fit coefficients and mean charge ratio for each station and corresponding sPMT models.

Station	sPMT Model	p_0	p_1	$\langle R \rangle$
56	R8619Sel-2	5.69 ± 0.02	17 ± 1	5.981 ± 0.005
59	R8619Sel	7.68 ± 0.05	152 ± 2	12.79 ± 0.02
60	R6094	6.94 ± 0.03	20 ± 2	7.314 ± 0.007
62	ET9107B	8.40 ± 0.04	29 ± 2	9.125 ± 0.009
1733	R8619Sel-2	6.22 ± 0.02	24 ± 1	6.661 ± 0.005
1736	R8619Sel-2	7.74 ± 0.03	43 ± 1	8.652 ± 0.006
1737	ET9107B	9.07 ± 0.05	42 ± 2	10.15 ± 0.01
1738	R6094	7.77 ± 0.04	21 ± 2	8.173 ± 0.008
1742	R8619Sel-10	7.54 ± 0.04	23 ± 2	8.043 ± 0.008
1744	R8619Sel-2	7.39 ± 0.06	15 ± 3	7.66 ± 0.01

5.3.2 Precision of calibration methods

Assessing the accuracy of a calibration method is extremely important. If the calibration is inaccurate it might compromise further analysis of the data, such as event reconstruction.

For each event, the calibration of the small PMT yields a signal in VEM. However, the equivalent signal of the sPMT in VEM is known from the large PMTs[1]. Therefore, for a given event, we define the uncertainty on the sPMT charge obtained from the calibration ($Q_{unc.}$) as

$$Q_{unc.} = \frac{Q_{LPMT}\ (\mathrm{VEM}) - Q_{sPMT}\ (\mathrm{VEM})}{Q_{LPMT}\ (\mathrm{VEM})}\ , \tag{5.5}$$

where Q_{sPMT} (VEM) is the charge on the small PMT in VEM units obtained from the calibration method, i.e., from Eqs. 5.2 and 5.4. The term Q_{LPMT} (VEM) is the corresponding signal detected by the LPMTs in VEM.

We present in Fig. 5.8 the histogram of the uncertainty on the charge of the sPMT obtained from calibration for one of the engineering-array stations. The result for the method of the linear fit is shown in blue whilst in red for the charge ratio.

The linear-fit method has a distribution with mean closer to zero than the

[1]For non-saturated events detected by both the large and small PMTs, i.e., all the events shown in Fig. 5.6.

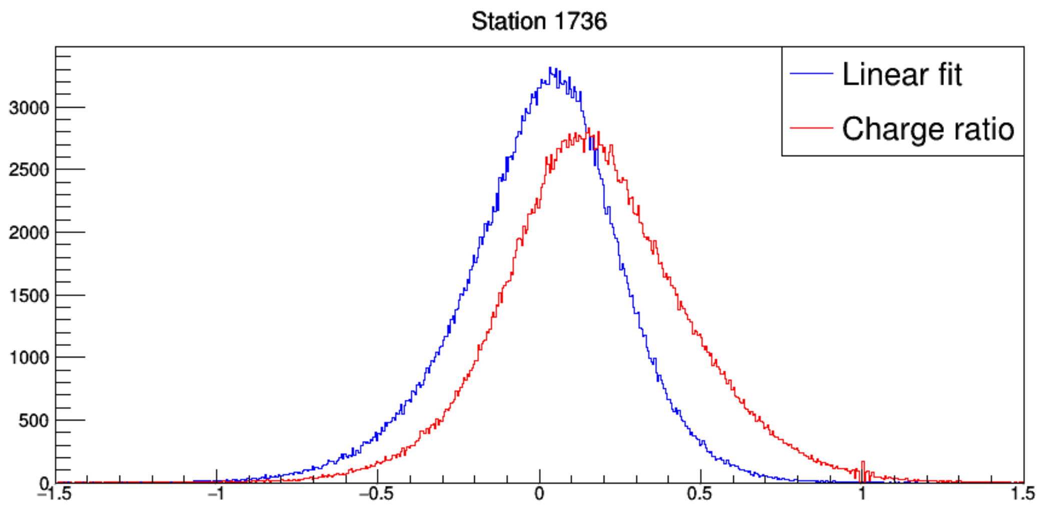

Figure 5.8: Histogram of the uncertainty on the sPMT charge obtained from calibration. The results for the linear-fit (blue) and charge-ratio (red) methods are shown. The linear-fit method presents a narrower distribution with mean closer to zero.

charge-ratio method. The width of the distribution of the first is also narrower. We were already expecting this result, as the charge-ratio method uses the approximation that coefficient p_1 in Eq. 5.2 is negligible, when actually, there are events for which it is not,

Table 5.4: Mean value and standard deviation of the uncertainty distribution on the sPMT calibration for all engineering-array stations.

	Linear fit		Charge ratio	
Station	Mean (%)	Std dev (%)	Mean (%)	Std dev (%)
56	0.374	24.1	6.87	25.2
59	-1.40	38.3	59.1	52.3
60	0.646	27.3	7.43	28.5
62	-0.553	30.6	9.90	32.6
1733	0.104	24.3	9.99	26.0
1736	0.253	25.2	17.0	29.0
1737	0.216	28.2	13.3	31.4
1738	-0.771	25.9	6.84	27.0
1742	0.493	27.5	9.30	29.1
1744	-0.243	29.3	5.32	30.1

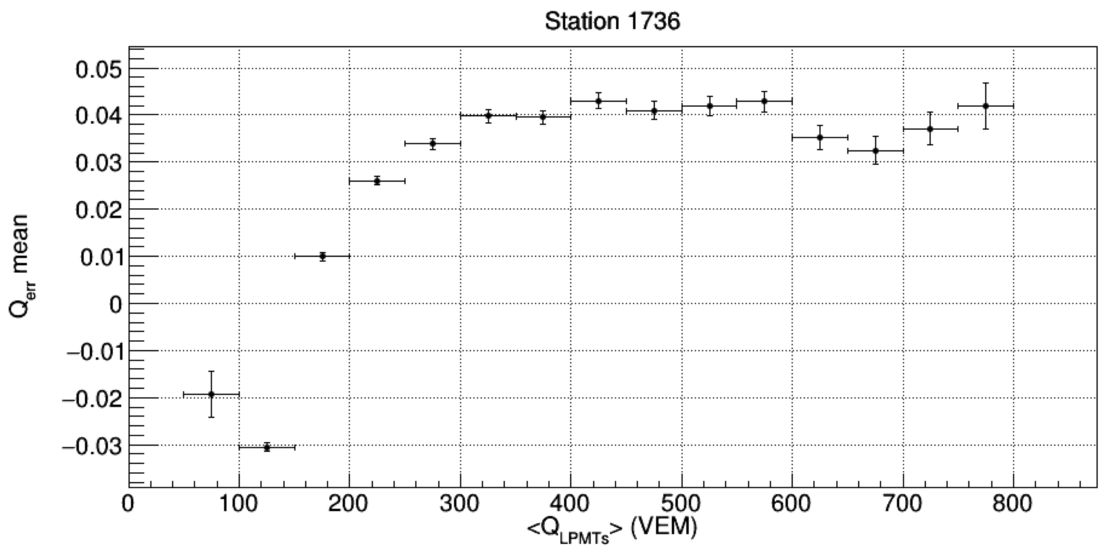

Figure 5.9: Profile of the uncertainty on the sPMT calibration for different intervals of 50 VEM on the charge of the LPMTs. The mean uncertainty on the sPMT calibration is within 5% across the whole range of LPMT charges.

for instance, events for which the sPMT charge is small.

Although the distribution peak is close to zero, there are events that have the uncertainty on the sPMT calibration larger than 10%. This might affect event reconstruction and should be investigated further. The mean value of the distributions and their standard deviation for the two calibration methods are presented in Tab. 5.4. We verified that the method using the linear fit always has the mean closer to zero and a smaller standard deviation than the charge-ratio method.

After establishing the linear-fit method as the one with better results, we plotted, as shown in Fig. 5.9, the profile of the uncertainty on the sPMT calibration for different intervals of the LPMT charge, each with width of 50 VEM. For each interval, we did a histogram of the uncertainty, such as the one in Fig. 5.8, from where the mean value and its uncertainty were retrieved. The mean uncertainty on the sPMT calibration was within 5% across all the range of signals in the LPMTs of station 1736. Apart from station 59, all the other stations presented similar results with the mean uncertainty within 10% for the whole range of charges on the LPMTs.

5.3.3 Investigation of calibration uncertainty sources

The distribution width of the uncertainty on sPMT calibration in Fig. 5.8 calls for a deeper investigation of its source.

From the definition of calibration uncertainty in Eq. 5.5, events with larger uncertainty correspond to those for which the sPMT charge in VEM, from calibration, differs more from the corresponding VEM charge on the LPMTs. Analyzing the plot of sPMT calibration with linear fit (see Fig. 5.6), one verifies that, indeed, there are events far from the fit line. Besides, it also shows that for a given value of sPMT charge, in hardware unit, there is a spectrum of corresponding values for the LPMT charge which translates into the width of the distribution of the calibration uncertainty.

The output charge in a PMT is the product of the number of photoelectrons, emitted from the photocathode, by the PMT gain (see Appendix A). However, the number of photoelectrons is given by the number of photons arriving at the PMT multiplied by its quantum efficiency (η). Therefore, the PMT charge can be written

$$Q = n_\gamma \eta G \ , \tag{5.6}$$

where G is the gain. Since the number of photons arriving at the PMT is the number of photons per unit of area (μ_γ) times the collecting area of the photocathode (A), then Eq. 5.6 becomes

$$Q = \mu_\gamma A \eta G \ . \tag{5.7}$$

Following Eq. 5.7, the ratio between the charge of the large and small PMT is

$$\frac{Q_L}{Q_s} = \frac{\mu_\gamma A_L \eta_L G_L}{\mu_\gamma A_s \eta_s G_s} = \frac{A_L \eta_L G_L}{A_s \eta_s G_s} \ , \tag{5.8}$$

where the terms μ_γ were cancelled out because it is assumed that the photons are scattered homogeneously inside the tank volume. Because the collecting area and quantum efficiency of the PMTs are fixed, keeping a constant gain ratio should yield a constant charge ratio.

In Fig. 5.10, we plotted the charge ratio between the large and small PMTs as a function of time along with a corresponding histogram. The charge of both PMTs were in hardware units for the ratio calculation. It presents a constant behaviour in time, as expected from the discussion above. However, there are fluctuations around the mean value which cause the charge width in the calibration curve (see Fig. 5.6) and consequently the width on the distribution of the calibration uncertainty (see Fig. 5.8).

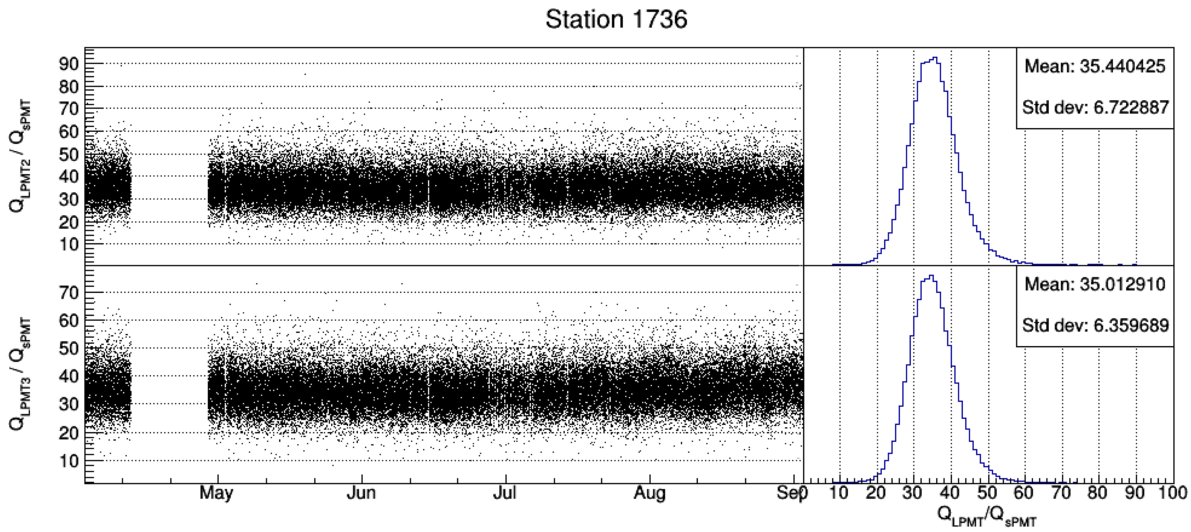

Figure 5.10: Charge ratio between large and small PMT as a function of time. The corresponding histograms are also shown. The ratio is quite constant in time. However, there are fluctuations around the mean value which produce the width on the distribution of the calibration uncertainty.

As seen from Eq. 5.8, some factors may affect the charge ratio. For instance, if the gain of the photomultiplier tubes varies, so will the charge ratio. In this context, the effects of temperature on the performance and response of the PMTs were studied.

Firstly, we observed that there is no correlation between temperature variations and the fluctuations of charge ratio on a daily time scale. Regardless of this result, a dependence on long-term variations of temperature was found for some stations, as displayed in Fig. 5.11 for station 62. There, the charge ratio tends to increase with temperature. This effect can be seen more clearly after August, when a raise on the charge ratio is more distinctive.

We performed the small PMT calibration, using the linear-fit method, for intervals of 24 hours. In Fig. 5.12, the coefficient p_0 obtained (see Eq. 5.2) as well as the temperature were plotted as a function of time. Again, we verified a long-term variation of p_0 with temperature, although a daily correlation can not be observed.

Even though we found a relation between the small PMT calibration (and charge ratio) and long-term variations of temperature, the source of the short-time fluctuations on the charge ratio remains to be discovered. Variations of the charge ratio for an one-hour interval are displayed on the plot of Fig. 5.13. Such variations happen in a

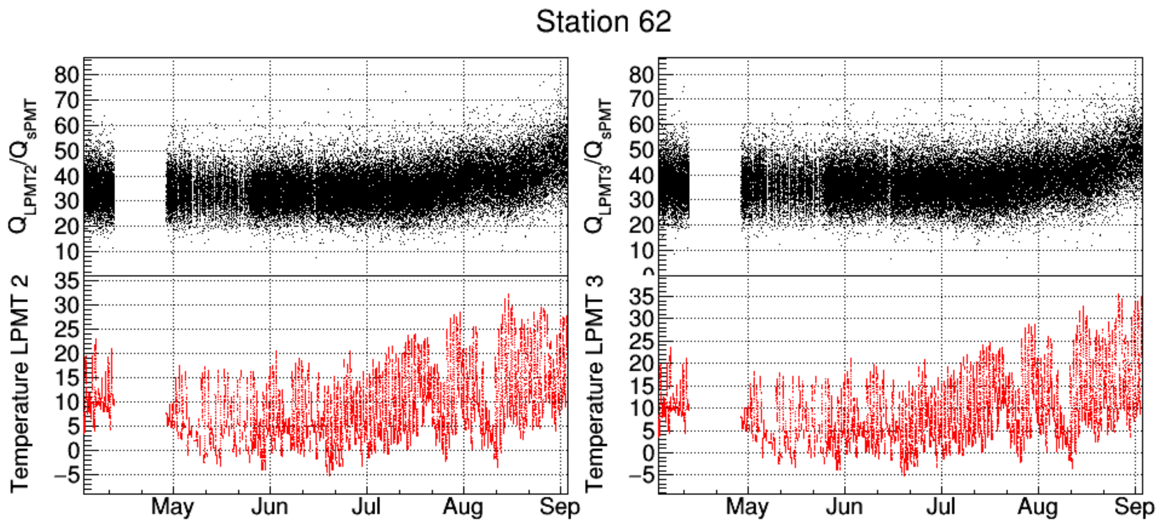

Figure 5.11: Ratio between charge of the large and small PMTs and temperature as a function of time for station 62. A dependency of the charge ratio on long-term variations of temperature is observed.

rapid and random fashion. Therefore, parameters which vary slowly, such as temperature, can not afford for these fluctuations.

The gain of a photomultiplier tube depends on its high-voltage supply (HV). Thus, instabilities in the HV could induce fluctuations consistent with the ones observed in Fig. 5.13. To verify this possibility, we plotted the charge ratio along with the HV in

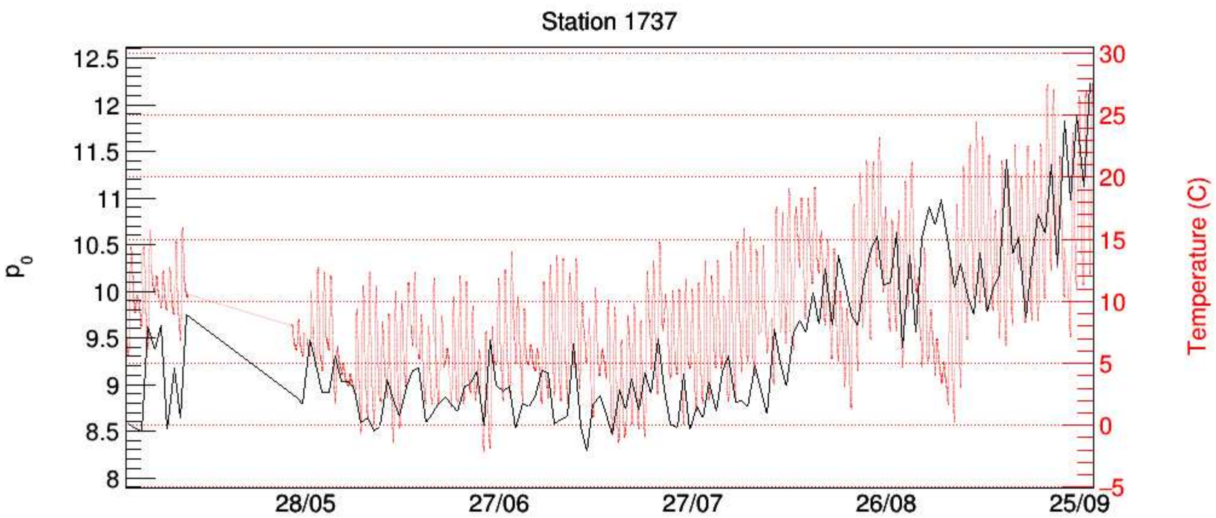

Figure 5.12: Parameter p_0 obtained from the small PMT calibration using the linear-fit method and temperature as a function of time. There is a correlation between p_0 and long-term variations of temperature.

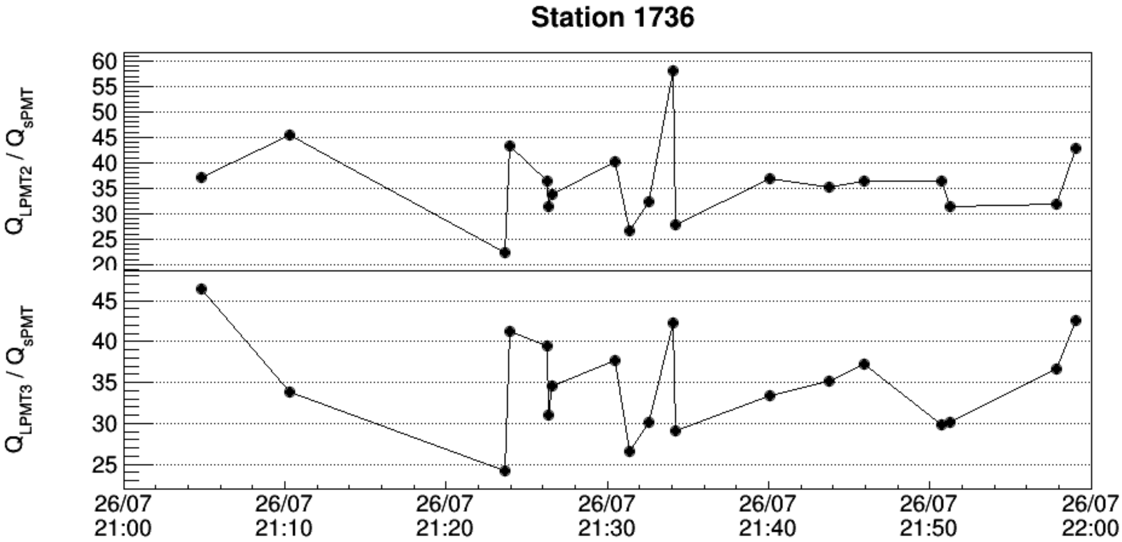

Figure 5.13: Fluctuations of the charge ratio during an one-hour interval. Such variations are rapid and random. Parameters which vary slowly can not afford for the fluctuations observed.

each PMT for an one-hour interval. We verified from Fig. 5.14 that variations in the HV are not the direct cause of fluctuations in the charge ratio.

Using the monitoring data, we investigated whether other parameters of the stations, such as the voltages feeding the control board of the PMTs, could account for the fluctuations in charge ratio. We used a procedure analogous to the plot in Fig. 5.14 for the high-voltage supply. Again, no direct correlation was found. The statistical nature

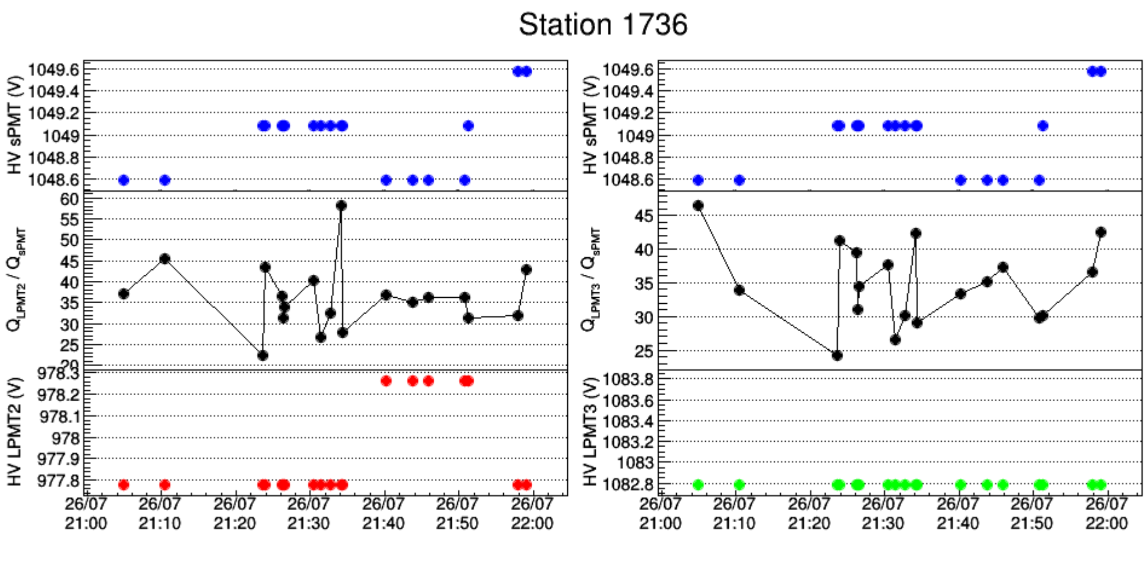

Figure 5.14: Behaviour of charge ratio and high-voltage supply during an one-hour interval. The fluctuations of charge ratio are not correlated to variations in the high voltage.

of electron emission by the photoelectric effect, in the photocathode, could also produce fluctuations, however they should have a smaller effect than observed in Fig. 5.13.

The above results seem to indicate that the fluctuations in charge ratio, which are the cause of the uncertainty in the sPMT calibration, are due to something intrinsic to the electronics applied for data acquisition.

5.3.4 Calibration interval

All the analysis presented so far was performed using the data set for the whole test period. When the small PMTs become part of the whole surface detector, they should be calibrated every certain time interval. The question that naturally arises is: how often should the sPMTs be calibrated?

The long-term variation of charge ratio and calibration parameters with temperature, as displayed in Figs. 5.11 and 5.12, suggests that the calibration should be performed for smaller time intervals, so that the long-term temperature effects do not influence on the calibration.

On the other hand, the calibration interval should be long enough to gather enough events so that it is statistically possible to perform an acceptable linear fit (see Fig. 5.6) to achieve the small PMT calibration. From the plots in Figs. 5.1 and 5.2, the stations register about 100 events per hour which can be used for the sPMT calibration.

We applied the following method to find a reasonable calibration interval. Along the whole test period, the sPMT calibration was performed every certain time interval. For each calibration, a histogram of the calibration uncertainty was done, from which the distribution mean and standard deviation were retrieved. Each of these quantities were filled into a corresponding histogram to verify whether the values for each calibration are consistent with each other. The mean value of these last histograms were plotted for the corresponding calibration interval, with error bars representing the corresponding standard deviation of the distributions. Such plots for three stations of the engineering array are shown in Fig. 5.15.

From the plots on the left in Fig. 5.15, the mean uncertainty on the calibration seems to be independent of the calibration interval chosen, as it is quite constant and close to zero. Considering the error bars, the calibration mean uncertainty is within 10%. Another distinctive feature is that the error bars decrease for longer calibration intervals.

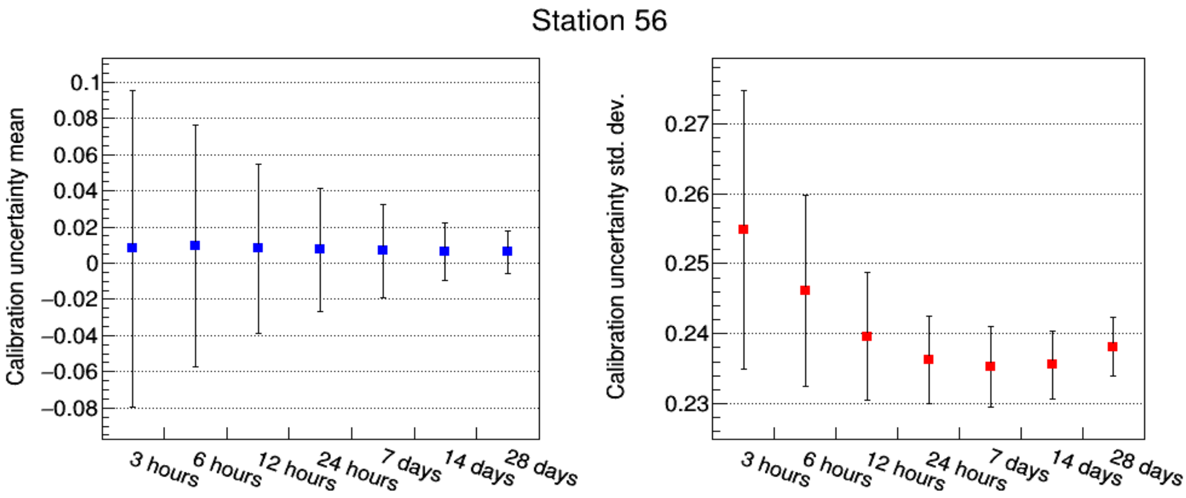

(a)

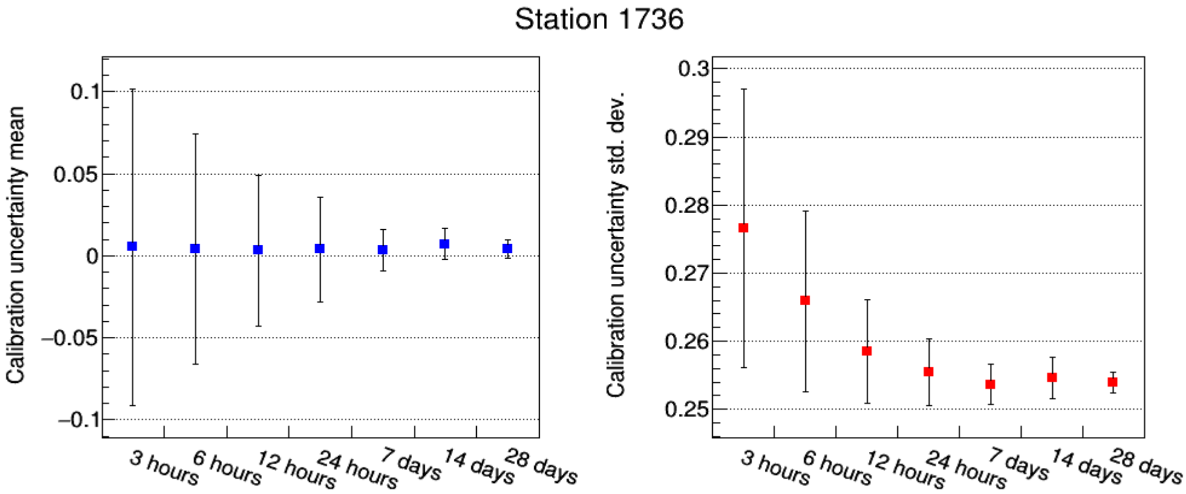

(b)

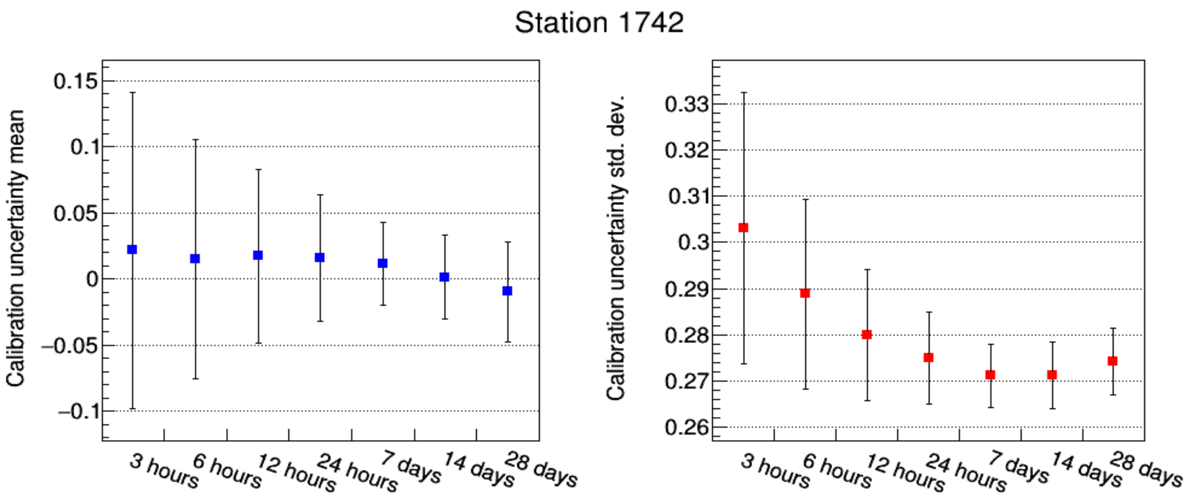

(c)

Figure 5.15: Small PMT calibration error mean and standard deviation for different calibration intervals. Results are shown for stations (a) 56, (b) 1736 and (c) 1742.

Since the error bars represent the standard deviation of the distribution of the mean uncertainty on the calibration for a given interval, we can conclude that as the calibration interval becomes larger the values for the calibration uncertainty becomes more consistent among each calibration performed. This result is expected, since for a larger calibration interval, the number of events is also larger, improving the statistics and the quality of the linear fit performed for the calibration.

Regarding the standard deviation of the calibration uncertainty on the right in Fig. 5.15, we verified that it is between 22 and 30% for all stations. Similar results were obtained in the analysis with the whole data set, shown in Fig. 5.8 and Tab. 5.4. There, the values of the standard deviation were ascribed to the fluctuations in charge ratio, as observed in Fig. 5.10.

The standard deviation presents the following behaviour: it decreases with calibration interval, passing through a minimum at about seven days and then it increases. The initial decrease is probably due to improvement of statistics, because of a larger number of events for larger calibration intervals, as mentioned before. The increase for larger intervals can be associated with long-term temperature variation. As shown previously, it affects the charge ratio and the calibration, causing a wider distribution of the calibration uncertainty. The error bars become smaller for larger intervals up to about seven days when their size does not vary much. This effect can also be related to statistical improvement for larger calibration intervals up to the point when the effects of long-term variations of temperature become important. The difference of standard deviation for each calibration interval is small, within 5% considering all stations.

A preferred time interval to perform the small PMT calibration should fulfill some requirements:

1. Calibration mean uncertainty close to zero,
2. across all calibrations performed, small variations on the calibration mean uncertainty,
3. width of the distribution of calibration uncertainty as small as possible, for each calibration performed,
4. calibration time interval as small as possible, so to minimise impact on data collection if some malfunction affects a station.

Since the mean uncertainty on the calibration does not depend on the calibration interval, requirement 1 is automatically met for all calibration intervals. Item 4 discards intervals larger than a day, because waiting that amount of time to have a sPMT calibration after a station malfunction is not feasible.

Condition 2 translates into intervals with small error bars in the plot of the mean uncertainty on the calibration (Fig. 5.15 left). As discussed, this is associated with larger calibration intervals. Regarding condition 3, the preferred intervals would be those closer to seven days, as it presented the smallest standard deviation on the calibration uncertainty (Fig. 5.15 right).

Among the calibration intervals not excluded by condition 4, the one that presents smaller variation on the mean uncertainty and standard deviation of the calibration is the 24-hours interval, which could be used when the small PMT is implemented in the surface-detector array.

5.4 Dynamic range extension

As we discussed in Chapter 4, the goal of implementing the small area PMTs is to overcome the saturation of the surface detectors by extending their dynamic range and thus enabling them to detect a broader signal spectrum.

Using the small PMT calibration with the linear-fit method (performed using data for the whole test period), we plotted the charge spectrum in VEM units displayed in Fig. 5.16 for one of the engineering-array stations. The charge spectrum for the large and small PMTs are shown. Non-saturated events are distinguished from the saturated ones.

On the overlap region of unsaturated signals on the small and large PMTs, we verify a good agreement of their charges. When the LPMTs saturate, such agreement is not observed, instead a bump in relation to the sPMT spectrum is present.

The large PMTs register non-saturated signals up to about 1000 VEM. On the other hand, the small PMT can detect unsaturated signals up to about 25000 VEM, therefore a dynamic range extension of factor 25 was achieved with the implementation of a small area PMT. Similar results were also obtained for the other stations of the engineering array.

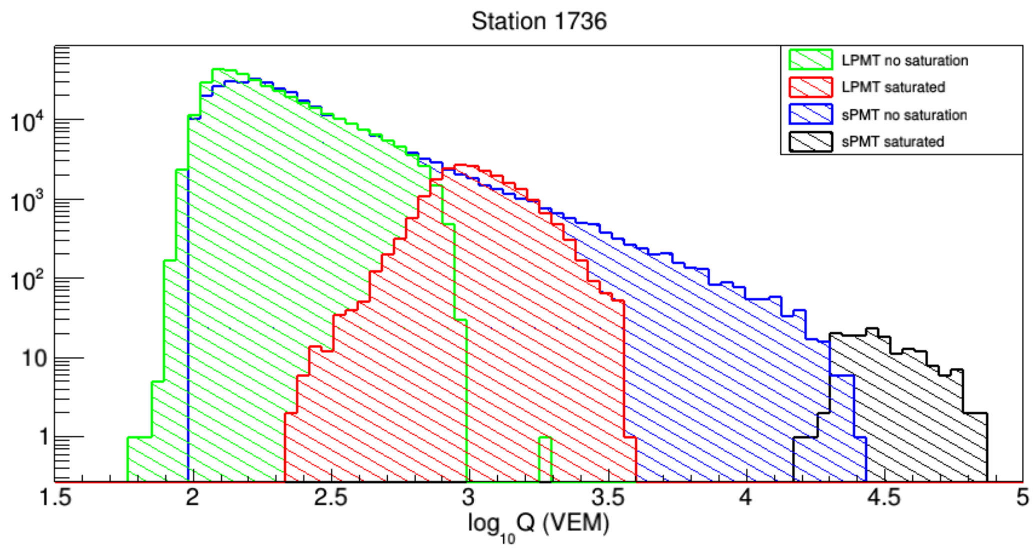

Figure 5.16: Charge spectrum for engineering-array station 1736. Large and small PMTs spectra are shown separately. Saturated and non-saturated events are also distinguished for each kind of PMT. The dynamic range of the station was extended from around 1000 VEM with the large PMTs to around 25000 VEM with the implementation of the small PMT.

Despite the extension of dynamic range seen in the charge spectrum, we observe events where even the small PMT saturated. We display in Tab. 5.5 the number of saturated events for the small and large PMTs. Although there are still saturated events

Table 5.5: Number of saturated events for the small and large PMTs.

Station	LPMT saturated events (%)	sPMT saturated events (%)
56	6	0.06
59	6	0.03
60	7	0.06
62	6	0.03
1733	6	0.05
1736	6	0.05
1737	7	0.04
1738	6	0.05
1742	6	0.05
1744	6	0.05

with the small PMT, the occurrence of saturation was greatly reduced from roughly 6% to less than 0.1%.

Chapter 6

Conclusions

As part of the upgrade plan of the Pierre Auger Observatory, each water-Cherenkov detector will receive an additional photomultiplier tube with small photocathode area to overcome the occurrence of saturation in the stations. In our work, we have analysed the data collected by ten experimental detectors equipped with small photomultiplier tubes (sPMT). Our analysis aimed at assessing their performance in the field and validating its proposal as solution to the saturation problem by extending the dynamic range of the detectors.

Using monitoring data, we have verified that the small PMTs presented a stable behaviour under the configuration of the detectors in the field during most of the test period. The analysis of the frequency of events registered by the stations also reinforces the sPMT robustness. In addition, we verified that roughly 100 events are observed every hour. This allows the calibration of the sPMTs using physical events to be performed in the course of some hours.

The signals produced in the small PMTs are digitised by an analog-to-digital converter. It outputs the signals in hardware units. Therefore, a procedure is needed to convert the signals into a unit which reflects the particle density that crossed the water volume of the detector. We call such procedure the calibration of the sPMTs. The physical unit used is the vertical equivalent muon (VEM), defined as the signal produced by a vertical muon crossing the centre of a station. We have studied two methods of calibration.

In the first method, events which produce non-saturated signals in both standard and small PMTs of a station are used. The standard PMTs are also called large PMTs

(LPMTs). We performed a linear fit in the plot of the average charge registered by the large PMTs, in VEM units, as a function of the sPMT charge. The value of the charge in VEM unit for the LPMTs are known from their independent calibration method which can not be applied for the sPMTs. Using the linear-fit parameters we can find the charge of the small PMT in VEM units.

Before performing the linear fit, we have defined cuts on the sPMT charge to remove biases caused by the triggering condition and by the saturation of the LPMTs. Such cuts were manually set. We believe that implementing an algorithm to automatically define the cuts by minimising the uncertainty on the calibration obtained with the resulting linear fit could be desirable.

For the second calibration method, we computed the ratio between the charge of the LPMTs, in VEM units, and the sPMT charge for non-saturated events. The mean value of the charge ratio was obtained from a corresponding histogram and it was used to convert the signals of the sPMTs into VEM units. This approach is not valid when the sPMT registers small signals, since it does not take into account the fact that a certain minimum particle density crossing the water volume is needed for a signal to be produced in the sPMTs.

We have defined the uncertainty on the calibration to assess the accuracy of the calibration methods studied. The linear-fit method presented mean uncertainty smaller than 1%. In contrast, the mean uncertainty using the charge-ratio method was around 10%. This result was already expected since the charge-ratio method is an approximation valid for large signals on the sPMTs. Despite the mean uncertainty being close to zero for the linear-fit method, there is a considerable amount of individual events for which the calibration uncertainty reached more than 20%. We believe that studying the impact of such uncertainties on the procedures of event reconstruction is important to be conducted in future works.

Given the large calibration uncertainty for some events, we investigated what could be its sources. We verified that the uncertainty was related to the width of the distribution of points in the calibration curve, and that the charge ratio between the small and large PMTs presented fluctuations around a mean value (in an ideal situation, the charge ratio should be constant). We found that long-term variations of temperature impact on the calibration. However, short-time fluctuations on the charge ratio were also observed. We could not find any correlation between these fluctuations and small variations in the station parameters such as the high-voltage supply of the PMTs. These results let us to conclude that the cause of the short-time variations of charge ratio, responsible for the calibration uncertainty, is due to some cause intrinsic of the station electronics. These uncertainties could be reduced with the upgraded electronics planned for the stations.

When the small PMT is implemented in the surface detectors, it will need to be calibrated every certain interval. We have analysed the engineering-array data to find a reasonable calibration frequency for the stations. We verified that with larger calibration intervals the calibrations are more consistent among each other. That is due to a larger statistics for larger time intervals. On the other hand, for intervals larger than seven days the standard deviation on the calibration uncertainty becomes larger, probably due to the long-term dependence of the calibration with temperature. In face of the results obtained, we suggest a calibration interval of 24 hours, since it would also minimise the impact on data collection if a station presents some malfunction.

The main goal of the small PMT proposal is to overcome saturation of the surface detectors by extending their dynamic range. Using the linear-fit method of calibration, which presented better performance, we plotted the charge spectrum of the engineering-array stations. We show that the implementation of the small PMT extended the dynamic range from around 1000 VEM to about 25000 VEM, an extension of roughly 25 times. Although a great dynamic-range extension was achieved, we still observe a few events with saturation. However, the occurrence of saturation observed in the engineering-array stations was reduced from about 6% to less than 0.1% with the implementation of the small PMT.

With the drastic reduction of saturation occurrence using the small PMT, we expect to have more precise measurements of extensive air showers produced by cosmic rays with the highest energies. This will provide a means to study the primaries with more accuracy and shed light on the questions of origin and propagation of ultra-high energy cosmic rays.

Bibliography

1. The Pierre Auger Collaboration. The Pierre Auger Observatory Upgrade - Preliminary Design Report. *arXiv:1604.03637* (2016).
2. Ginzburg, V. L. Cosmic ray astrophysics (history and general review). *Physics-Uspekhi* **39,** 155–168 (1996).
3. Heitler, W. *The Quantum Theory of Radiation* third ed. p. 386 (Section 38) (Oxford University Press, 1954).
4. Mollerach, S. & Roulet, E. Progress in high-energy cosmic ray physics. *Progress in Particle and Nuclear Physics* **98,** 85–118. ISSN: 0146-6410 (2018).
5. Matthews, J. A Heitler model of extensive air showers. *Astroparticle Physics* **22,** 387–397. ISSN: 0927-6505 (2005).
6. Glasmacher, M. *et al.* The cosmic ray composition between 10^{14} and 10^{16} eV. *Astroparticle Physics* **12,** 1–17. ISSN: 0927-6505 (1999).
7. http://www.ams02.org. Accessed 27-08-2018.
8. Gaisser, T. Cosmic-Ray Showers Reveal Muon Mystery. *Physics* **9** (2016).
9. Tanabashi, M. *et al.* Review of Particle Physics. *Phys. Rev. D* **98,** 030001 (3 2018).
10. Aab, A. *et al.* The Pierre Auger Cosmic Ray Observatory. *Nuclear Instruments and Methods in Physics Research Section A: Accelerators, Spectrometers, Detectors and Associated Equipment* **798,** 172–213. ISSN: 0168-9002 (2015).
11. Abraham, J. *et al.* The fluorescence detector of the Pierre Auger Observatory. *Nuclear Instruments and Methods in Physics Research Section A: Accelerators, Spectrometers, Detectors and Associated Equipment* **620,** 227–251. ISSN: 0168-9002 (2010).

12. Allekotte, I. *et al.* The surface detector system of the Pierre Auger Observatory. *Nuclear Instruments and Methods in Physics Research Section A: Accelerators, Spectrometers, Detectors and Associated Equipment* **586,** 409–420. ISSN: 0168-9002 (2008).

13. *Photomultiplier XP1805* http://hzcphotonics.com. Accessed May-2018.

14. Aglietta, M. *et al. Response of the Pierre Auger Observatory Water Cherenkov Detectors to Muons* in *Proceedings of 29th International Cosmic Ray Conference, Pune* **7** (2005), 83–86.

15. Etchegoyen, A. *et al.* Muon-track studies in a water Cherenkov detector. *Nuclear Instruments and Methods in Physics Research Section A: Accelerators, Spectrometers, Detectors and Associated Equipment* **545,** 602–612. ISSN: 0168-9002 (2005).

16. Bertou, X. *et al.* Calibration of the surface array of the Pierre Auger Observatory. *Nuclear Instruments and Methods in Physics Research Section A: Accelerators, Spectrometers, Detectors and Associated Equipment* **568,** 839–846. ISSN: 0168-9002 (2006).

17. Newton, D., Knapp, J. & Watson, A. The optimum distance at which to determine the size of a giant air shower. *Astroparticle Physics* **26,** 414–419. ISSN: 0927-6505 (2007).

18. Hersil, J., Escobar, I., Scott, D., Clark, G. & Olbert, S. Observations of Extensive Air Showers near the Maximum of Their Longitudinal Development. *Physical Review Letters* **6,** 22–23 (1961).

19. Abraham, J. *et al.* Trigger and aperture of the surface detector array of the Pierre Auger Observatory. *Nuclear Instruments and Methods in Physics Research Section A: Accelerators, Spectrometers, Detectors and Associated Equipment* **613,** 29–39. ISSN: 0168-9002 (2010).

20. Schulz, A. *The measurement of the energy spectrum of cosmic rays above* 3×10^{17} *eV with the Pierre Auger Observatory* in *Proceedings of 33rd International Cosmic Ray Conference, Rio de Janeiro* (2013).

21. Fenu, F. *The cosmic ray energy spectrum measured using the Pierre Auger Observatory* in *Proceedings of 35th International Cosmic Ray Conference, Busan* (2017).

22. Martello, D. *The Pierre Auger Observatory Upgrade* in *Proceedings of 35th International Cosmic Ray Conference, Busan* (2017).

23. Castellina, A. *The dynamic range of the AugerPrime Surface Detector: technical solution and physics reach* in *Proceedings of 35th International Cosmic Ray Conference, Busan* (2017).

24. Agostinelli, S. *et al.* Geant4—a simulation toolkit. *Nuclear Instruments and Methods in Physics Research Section A: Accelerators, Spectrometers, Detectors and Associated Equipment* **506,** 250–303. ISSN: 0168-9002 (2003).

25. Argirò, S. *et al.* The offline software framework of the Pierre Auger Observatory. *Nuclear Instruments and Methods in Physics Research Section A: Accelerators, Spectrometers, Detectors and Associated Equipment* **580,** 1485–1496. ISSN: 0168-9002 (2007).

26. Ave, M., Roth, M. & Schulz, A. *A universal description of temporal and lateral distributions of ground particles in extensive air showers* in *Proceedings of 34th International Cosmic Ray Conference, The Netherlands* (2015).

27. Leo, W. R. *Techniques for Nuclear and Particle Physics Experiments A How-to Approach* Second Revised Edition (Springer-Verlag, 1994).

28. *Photomultiplier Tubes Basics and Applications* Third Edition. Hamamatsu Photonics (2007).

29. Lung, K. *et al.* Characterization of the Hamamatsu R11410-10 3-in. photomultiplier tube for liquid xenon dark matter direct detection experiments. *Nuclear Instruments and Methods in Physics Research Section A: Accelerators, Spectrometers, Detectors and Associated Equipment* **696,** 32–39. ISSN: 0168-9002 (2012).

Appendix A

Photomultiplier tubes

A basic discussion of photomultiplier tubes is given in this appendix. Here its working principles, main components, behaviour and main operation parameters will be presented. An in-depth description of photomultiplier tubes is not intended. Instead the basic ideas relevant for the project are described. For more information on the subject the reader is referred to Refs. [27, 28].

A.1 Overview

Photomultiplier tubes are devices that convert light into electrical signals. The schematic representation of the workings of a photomultiplier tube along with its main parts are presented in Fig. A.1. When a photon hits the photocathode material an electron is released by photoelectric effect. By means of an appropriate electric field, the electron reaches the first dynode causing secondary electrons to be emitted. These are accelerated by an electric field and hit the second dynode releasing even more electrons. This process repeats along all dynode stages producing a cascade of electrons which is collected by the anode and can be read as an electric current. The set of dynodes forms the electron-multiplier system. The acronym PMT will be used as shorthand for photomultiplier tube.

A.2 Photocathode and dynodes

Electrons are emitted from the photocathode material by photoelectric effect. In this process the energy of a photon is transferred to an electron of an atom. If the photon is

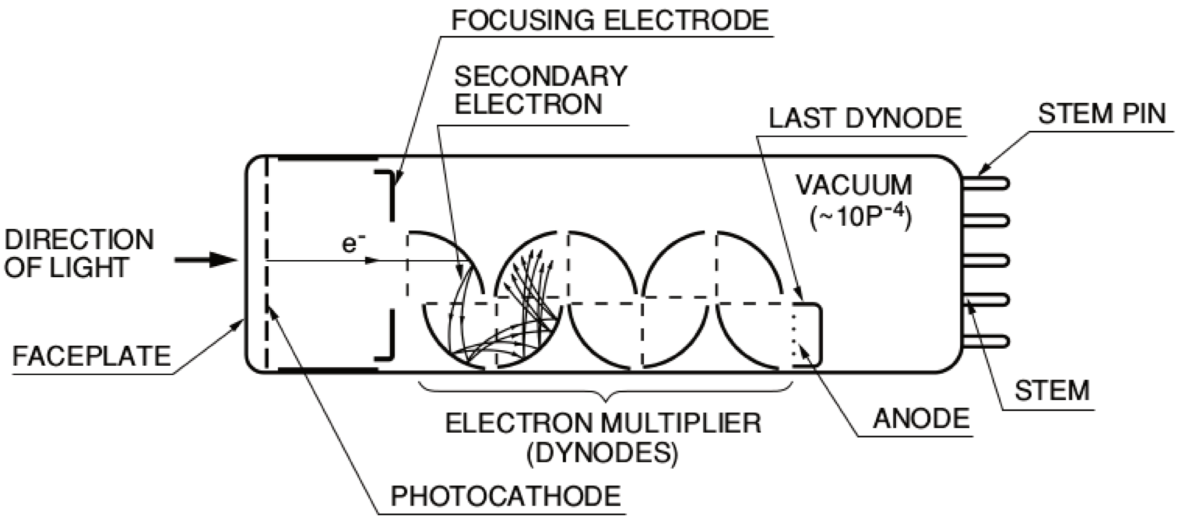

Figure A.1: Schematic view of a photomultiplier tube. A photon hits the photocathode releasing an electron by photoelectric effect. The electron is focused onto the first dynode where it releases even more electrons. These are accelerated by an electric field to the second dynode where further electrons are emitted. The process repeats along all dynodes of the electron multiplier system producing an electron cascade which is collected at the anode [28].

energetic enough the transferred energy will be enough to overcome the binding energy of the electron to the material. Such binding energy is represented by the work function ϕ. The released electron will have energy

$$E = h\nu - \phi \ , \tag{A.1}$$

where h is Planck constant and ν is the incident photon frequency.

The probability of an electron being emitted when a photon reaches the photocathode material is not unity and it depends on the photon wavelength. This effect can be expressed by the photocathode *quantum efficiency* (η), defined as

$$\eta(\lambda) = \frac{\text{number of electrons released}}{\text{number of incident photons } (\lambda)} \ , \tag{A.2}$$

with λ the photon wavelength. Such dependency of the quantum efficiency with the wavelength of the incident photon is plotted in Fig. A.2 for PMT model R11410-10 manufactured by Hamamatsu Photonics.

Photocathodes are usually made of semiconductor materials, since these have quantum efficiency of the order 10 to 30%, much larger than metals which present typical

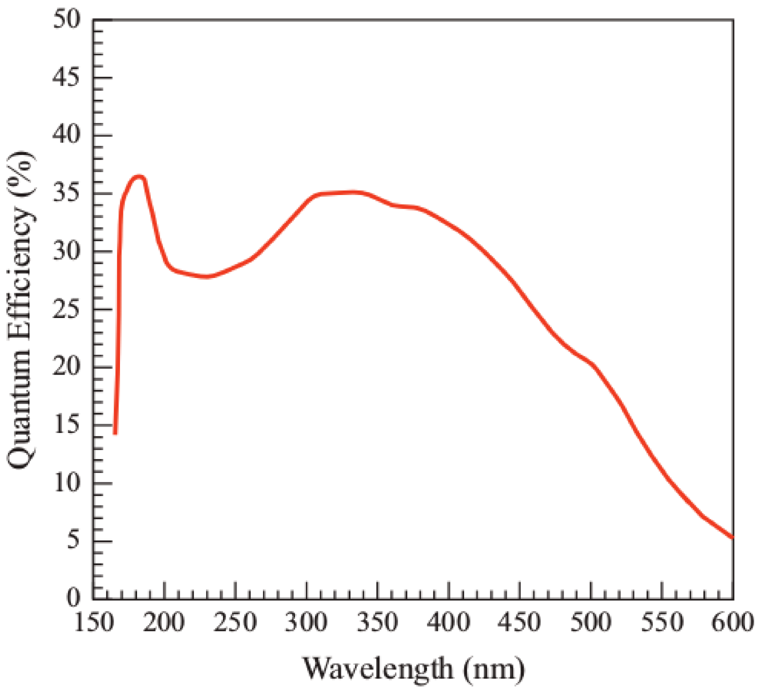

Figure A.2: Dependency of the quantum efficiency with the incident photon wavelength for PMT model R11410-10 by Hamamatsu [29].

quantum efficiency not greater than 0.1%. In a metal the electrons are essentially free, therefore when a photon transfers energy to an electron, the later will encounter many other electrons on its way out of the material, and the outgoing electron loses its energy to the free electrons making it hard to escape. On the other hand, a semiconductor material has most of the electrons tightly bound to the atoms, only the ones on the conduction and valence bands being approximately free. Thus, it is much more likely that an electron knocked out by a photon escapes a semiconductor material resulting in a larger quantum efficiency.

When an incoming electron hits a dynode it transfers energy to electrons of the material causing them to escape. The physical process behind electron emission at the dynodes is then very similar to the photoelectric effect, with the incident photon replaced by an electron. The *secondary emission factor* (δ) of a dynode is defined as the average number of electrons knocked out by an incident electron. Naturally, the secondary emission factor depends on the energy of the incoming electron, the more energetic, the more electrons are emitted. As the energy of the incident electron is proportional to the electric potential difference used to accelerate it, the secondary emission factor can be

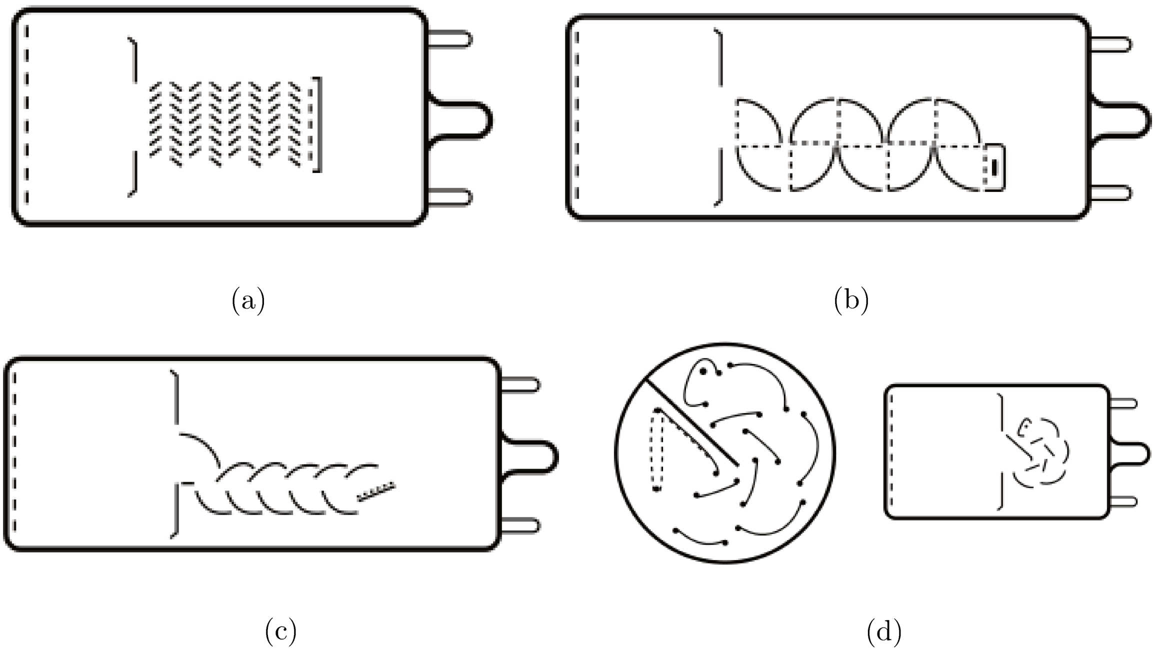

Figure A.3: Different dynode configurations [28]. (a) Venetian blind. (b) Box and grid. (c) Linear focused. (d) Circular focused.

expressed as

$$\delta = KV_d \;, \tag{A.3}$$

where V_d is the potential difference between the dynodes and K is a proportionality factor. Given the theory of secondary emission, the use of semiconductor materials as dynodes comes as no surprise.

Dynodes can be arranged in different geometrical configurations as seen in Fig. A.3. The configuration of a PMT can affect its performance, therefore different dynode arrangements can be used for different applications. For example, linear focused PMTs (Fig. A.3c) have better response linearity than venetian blind ones (Fig. A.3a).

A.3 Gain and single-electron spectrum

The *gain* (G) of a photomultiplier tube is the average number of electrons obtained at the anode for one electron emitted from the photocathode. Since the amplification at each dynode depends on the potential difference (see Eq. A.3), the gain also does. For a PMT with n dynodes and with the same potential difference applied between dynodes Eq. A.3

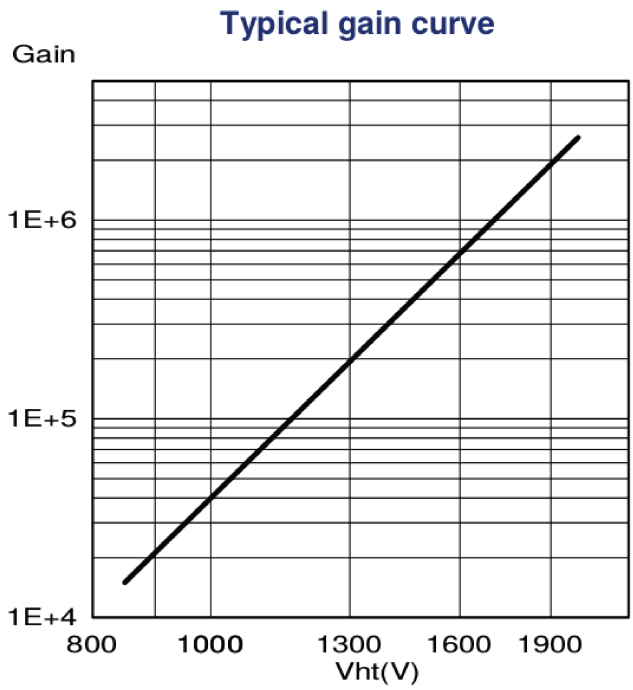

Figure A.4: Gain as a function of the supply voltage for PMT model XP1805 by HZC Photonics [13].

yields

$$G = \delta^n = (KV_d)^n \ . \tag{A.4}$$

The behaviour of the gain as a function of voltage supply for the PMT model XP1805 by HZC Photonics is observed in Fig. A.4. This is the PMT model used as the standard PMTs of the water-Cherenkov detectors of the Pierre Auger Observatory.

From Eq. A.4 one obtains the variation of gain when a variation of the voltage supply happens as

$$\frac{dG}{G} = n\frac{dV_d}{V_d} \ , \tag{A.5}$$

which implies that for a PMT with ten dynodes a variation of 1% on the voltage supply leads to a 10% variation on the gain. This result reinforces the importance of having a stable power supply feeding a PMT.

Given the statistical nature of the secondary emissions that take place at each dynode, single electrons of the same energy emitted by the photocathode may produce different currents at the anode resulting in fluctuations in the PMT gain. A histogram of the number of electrons collected at the anode when a single electron is emitted from the photocathode is presented in Fig. A.5, for PMT model R11410-10 by Hamamatsu

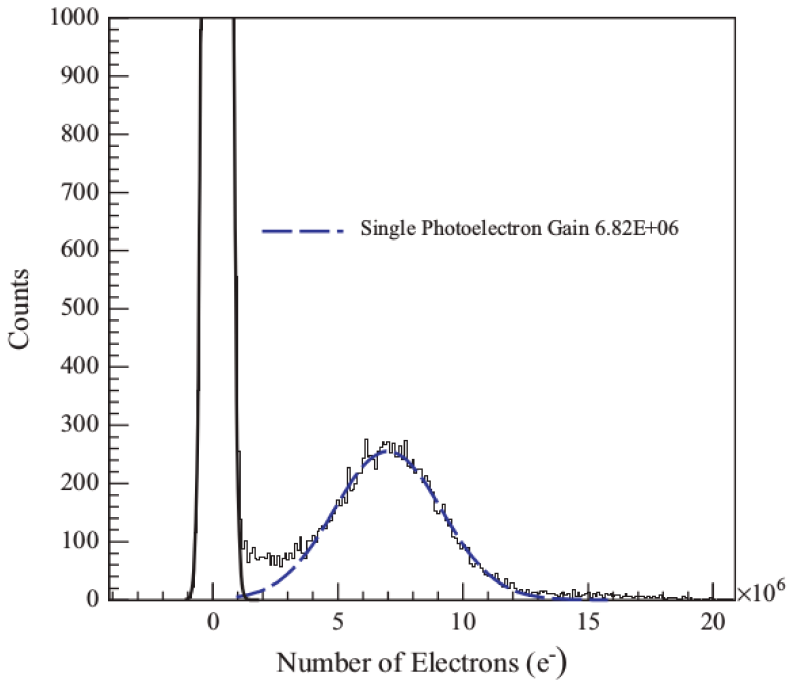

Figure A.5: Single-electron spectrum of PMT model R11410-10 by Hamamatsu Photonics. Fluctuations on the number of electrons at the anode are observed due to the statistical nature of secondary emissions at the electron-multiplier system of the PMT. The gain was obtained by fitting the distribution [29].

Photonics. This kind of plot is called a *single-electron spectrum* obtained using a very dim source of light such that the probability of more than one electron being emitted from the photocathode is rather small. The fluctuations around a mean value on the number of electrons at the anode are markedly distinct in the plot. The single-electron spectrum offers a means to measure the PMT gain, as observed in Fig. A.5 where a fit was used, and, therefore, the spectrum is an important step in the characterization of a PMT.

A.4 Voltage dividers

Ideally, the electric fields between the photocathode and the first dynode, the dynodes of the electron-multiplier system and the anode could be provided by batteries, however this approach is impractical.

Usually a high voltage is applied between the photocathode and the anode and a resistive circuit is used to properly set the potential difference between the dynodes. This kind of circuit is called a *voltage divider* and is represented in the schematic drawing

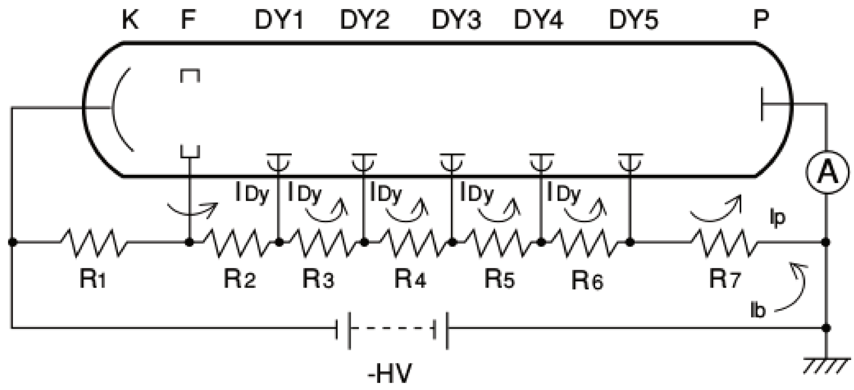

(a)

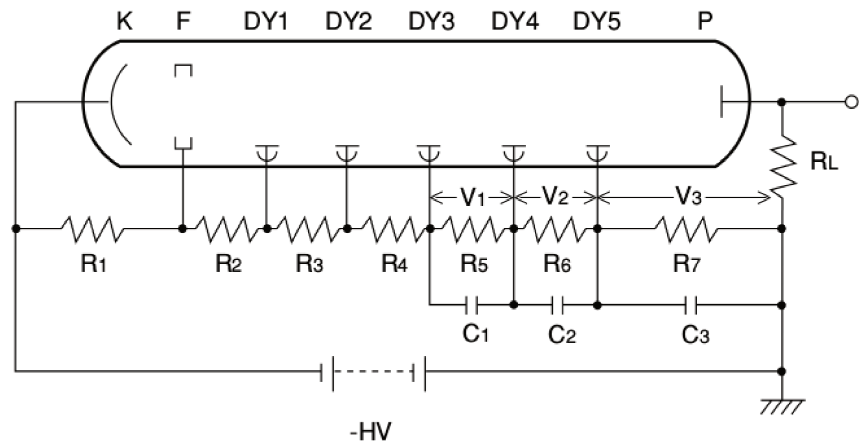

(b)

Figure A.6: Voltage dividers used to set the proper potential difference between the PMT components [28]. (a) Simple resistive divider. (b) Capacitors are employed in the last stages to keep their potential difference constant.

of Fig. A.6a.

The electric current on the voltage-divider circuit is known as the *bleeder current*. It is important that the bleeder current be larger than the electric current inside the PMT so that the potential difference between the dynodes be constant as well as the gain. Sometimes the PMT current on the last dynode stages can be quite high and cause fluctuation on the gain. Decoupling capacitors can be employed on the voltage-divider circuit of these stages to maintain their potential difference and, therefore, the PMT gain constant. Such circuit can be seen in Fig. A.6b.

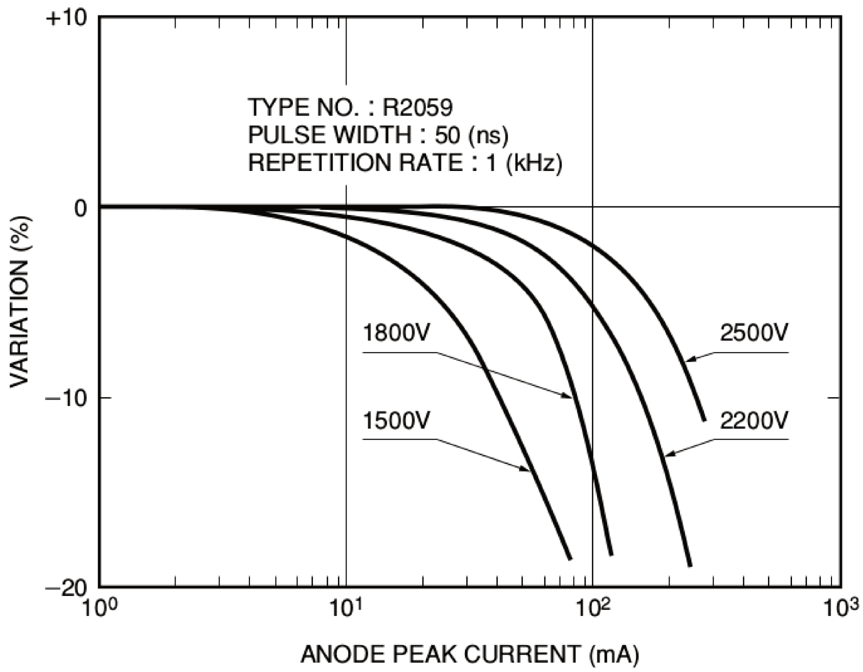

Figure A.7: Deviation from linearity as a function of peak current at the anode of a PMT [28]. Linear range is improved for increasingly higher voltage supplies which produce stronger electric fields between dynodes of the electron-multiplier system. PMTs are said to saturate when their responses deviate significantly from linearity.

A.5 Linearity

Linearity in a PMT means that the output signal at the anode increases linearly with the illuminating intensity at the photocathode. For example, if twice as many photons strike the photocathode an output signal twice as large should be observed at the anode.

The linearity of a PMT depends strongly on all electrons emitted in a dynode being collected in the next stage. When electrons are emitted from a dynode they create a space charge which tends to nullify the electric field towards the next dynode. Therefore, setting and keeping a high enough potential difference between dynodes is extremely important.

As mentioned in the previous section, the electric current between the last stages of a PMT can be quite high, therefore an intense electric field must be set to sweep the electrons emitted by these dynodes. This is accomplished by using a special kind of circuit known as a *tapered voltage-divider* in which the resistors between the last stages are set so that the potential difference is increasingly higher. Sometimes the current of the last stages is so large that additional high-voltage supplies are used to keep the gain constant and thus the linear behaviour of the PMT.

The deviation from linearity of a PMT as a function of the peak current measured at its anode is shown in Fig. A.7. The linearity improves for increasingly larger high-voltage supplies. This behaviour is expected, since higher voltages produce stronger electric fields between dynodes, thus the collection efficiency of emitted electrons is improved impacting directly on the linearity of the PMT.

When the response of a PMT deviates significantly from linearity it *saturates*. Therefore, when designing an experiment it is extremely important to characterise a PMT and know its range of linearity.